Award Title: Fusion-Enabled Pluto Orbiter and Lander

Report Type: NIAC Phase II Final Report

Principal Investigator: Ms. Stephanie Thomas, PSS
sjthomas@psatellite.com

Co-Investigators: Mr. Michael Paluszek, PSS
map@psatellite.com

Dr. Samuel Cohen, PPPL
scohen@pppl.gov

Institutions: Princeton Satellite Systems, Inc.
6 Market St. Suite 926
Plainsboro, NJ 08536
(609) 275-9606
www.psatellite.com

Princeton Plasma Physics Lab
P.O. Box 451
Princeton, NJ 08543-0451
(609) 243-2000

Period of Performance: May 9, 2017 through May 9, 2019

Report Date: May 15, 2019

NASA Award Number: 80NSSC18K0040

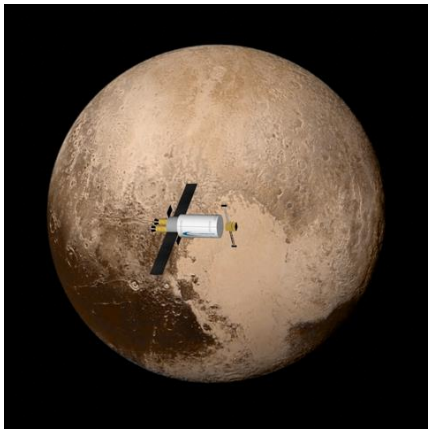

Executive Summary

Direct Fusion Drive (DFD) is a unique fusion engine concept based on the Princeton Field-Reversed Configuration (PFRC) fusion reactor conceived by Dr. Sam Cohen of the Princeton Plasma Physics Laboratory. DFD would enable the Pluto orbiter and lander context mission and more broadly enable true "rapid transit" to outer-planet and near interstellar space. The truly game-changing levels of thrust and power in a modestly sized package could integrate with our current launch infrastructure while radically expanding the science capability of these missions.

Our Phase I was our first funded work on the DFD, with previous work at PSS occurring only under internal R&D. We established the feasibility of our Pluto mission trajectories using straight-line and planar models, including a departure spiral from Earth and insertion at Pluto. We developed our first thrust and specific impulse model using the results of the UEDGE multi-fluid code. Our specific power model was improved.

During this Phase II effort, we continued our efforts to increase the fidelity of the designs for the RF, magnet, and shielding subsystems. Dedicated thrust augmentation experiments were run on the PFRC experiment, using a supersonic gas puffing valve. For the first time, we analyzed the design of a closed-loop operation mode and estimated the hardware that would be required for a dual-mode engine. In an exciting new development, we have invented a new thermophotovoltaic thermal conversion method that has the potential to have efficiencies of a Brayton or Stirling system. Our report presents details of these analyses.

Our roadmap to bringing DFD to flight predicts that with sufficient support, a first flight unit could be built by 2040. We anticipate that three machine generations are required before this point: a ~1 T PFRC-3 machine hitting new plasma temperature and density levels, a ~5 T PFRC-4 machine with first demonstration of D-3He fusion, and a flight. (The current experiment, PFRC-2, is limited to about 0.1 T). In order to achieve a flight in 2035-2040, the TRL of the supporting systems must be increased in parallel, including low mass radiators, cryogenic propellant storage, and large (>100 kW) thermal conversion systems. Fortunately, many of these systems are dual-use and are required for other technologies including fission systems, so DFD would contribute to and benefit from those programs.

This NIAC support and the results of our work have led to multiple follow-on contracts. We won two NASA STTRs focused on DFD subsystems, one on the RF system and one on the superconducting magnets, and our magnet STTR is now midway through a Phase II. We will be receiving a superconducting test magnet for experiments at PPPL this summer. In addition, we won an ARPA-E OPEN grant; this is the first time that OPEN has included fusion technologies, and we are part of a cohort of three alternative fusion companies now supported directly by DOE. We are very optimistic that if we are able to meet our experimental milestones in the next 12-18 months, we will be competitive for additional DOE grants to build PFRC-3.

Table of contents

List of Figures

List of Tables

1 Introduction

Figure 1 shows an artistic rendition of the space reactor, with key components labeled.

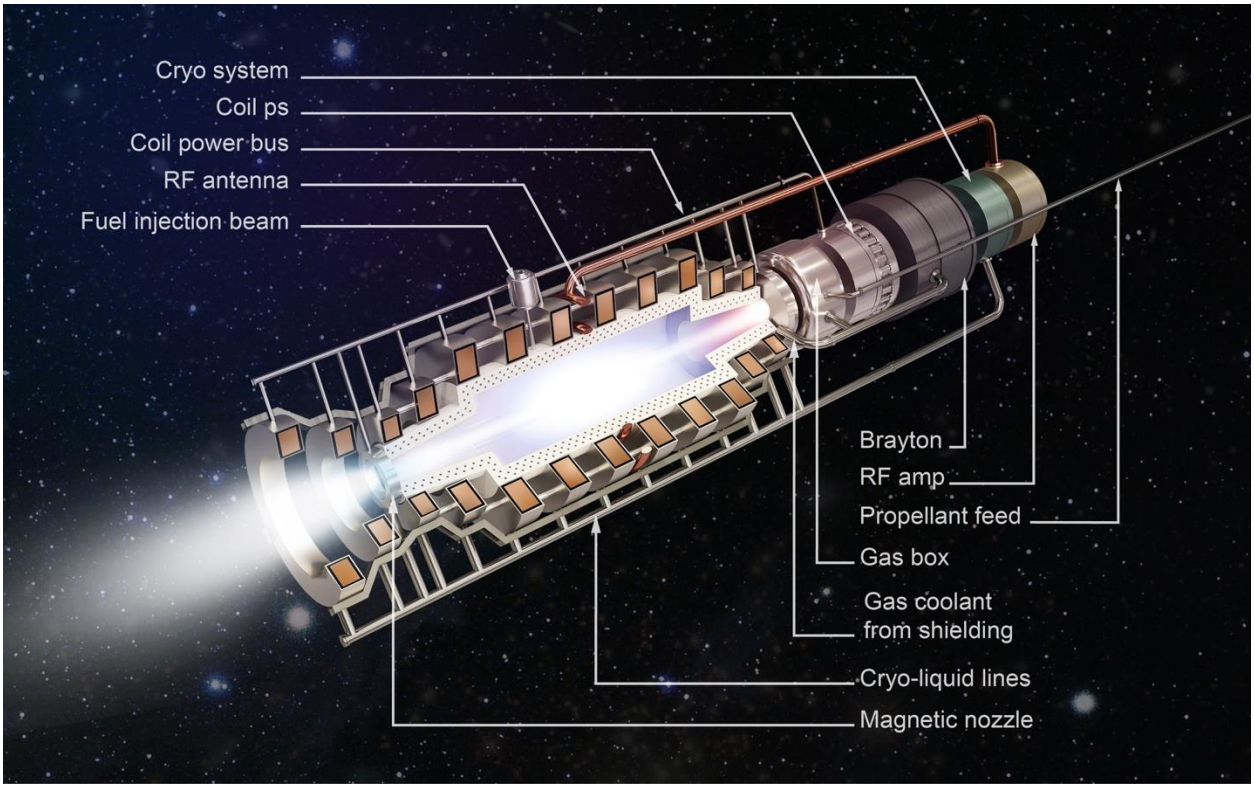

Figure 1. Artistic rendering of the DFD engine with an interior cutout to show detail of the coils.

Our NIAC mission context is delivery of a Pluto orbiter with a lander, with the lander being powered from orbit. Direct Fusion Drive (DFD) provides high thrust to allow for reasonable transit times to Pluto while delivering substantial mass to orbit: 1000 kg delivered in under four years using 5-10 N thrust. As much as 500 kW might be available to the payload, for communications and power beaming. In contrast, the recent New Horizons mission required a 10 year transit time for a flyby mission with the spacecraft having only about 200 W of power.

Our Phase I NIAC was our first funded work on the DFD, with previous work at PSS occurring only under internal R&D. PFRC was previously supported at PPPL at a low level under DOE funding. This supported the construction and operation of the PFRC-1, followed by the PFRC-2. These machines used repurposed water-cooled magnets with a specially designed vacuum vessel and RF subsystem. PFRC-2 has held the world record for pulse length in an FRC, and for a long time was the only fusion experiment in the US using high-temperature superconductors, which are utilized in the passive flux-conservers.

PFRC-1 and PFRC-2 established that the "odd-parity" RF heating method heats electrons efficiently. Appendix A of this report provides background information on the PFRC experiments. Dr. Cohen, the inventor of the PFRC, saw the potential for PFRC to be used as a space propulsion device. PSS collaborated with Dr. Cohen on a number of conference papers about Direct Fusion Drive [1] [2] [3] leading up to our NIAC Phase I award.

During Phase I, we established the feasibility of our Pluto mission trajectories using straight-line and planar models, including a departure spiral from Earth and insertion at Pluto. We developed our first thrust and specific impulse model using the results of the UEDGE multi-fluid code. Our specific power model was improved.

During this Phase II effort, we continued our efforts to increase the fidelity of the designs for the RF, magnet, and shielding subsystems. Dedicated thrust augmentation experiments were run on the PFRC experiment, using a supersonic gas puffing valve. For the first time, we analyzed the design of a closed-loop operation mode and estimated the hardware that would be required for a dual-mode engine. In an exciting new development, we have invented a new thermophotovoltaic thermal conversion method that has the potential to have efficiencies expected from a dynamic system in a static device.

In this report, we begin by reviewing the Phase II work plan. We give a brief overview of the PFRC and list the applicable software tools. We then discuss the results in order of tasks. We conclude with updated reference designs for a 1 MW and 10 MW engine. In our conclusion, we present roadmaps for continued developed of DFD with the goal of a flight article by 2040.

We would like to acknowledge the contributions of Dr. Sam Cohen, Co-I at PPPL; Mr. Michael Paluszek and Charles Swanson of PSS; Mary Dahl, Alice Gao, Eric Ham, Eric Hinterman, Yukino Nagai, Lisa Peng, Tingxiao Sun, and Audrey Walsh, PSS interns; Alexander Glasser, Eugene Evans, and Peter Jandovitz, PPPL graduate students; and Gabriel Gaitan, Fred Zheng, Johannes van de Wetering, Alan Kaptanoglu, Ben Taylor, Matt Penza, Tony Qian, PPPL interns. The artist who did the rendering above was S. Shalumov.

2 Methods and Assumptions

2.1 Work Plan

Our Phase I findings indicated that our baseline mission trajectories to Pluto were feasible. Lower cost launch vehicles could be used if the DFD vehicle were launched first into LEO. It would then depart from LEO using a spiral trajectory. Our mass studies indicated that we need to more carefully account for the mass of the magnets, as the both superconductor and its support structure are important mass drivers. The RF subsystem is not a mass driver but does drive the total engine efficiency. The Phase II research objectives are focused on those subsystems that have the most unknowns after Phase I in terms of their design specifications and contributions to the engine mass.

The shielding and coil design remain key drivers that merit further analysis, due to the wide range of superconducting wire and cables currently available or under development, and the impact of the superconductor neutron tolerance on the shielding design.

In evaluating our engine modeling process, we also determined that we need a better model of the synchrotron radiation. Global loss models developed for tokamaks cannot be directly applied to FRCs due to the variation in the field and plasma properties. A simple model using a 10% volume adjustment may be greatly overestimating the synchrotron losses at 30%, while other absorptions models in the literature may be underestimating it at only 5%.

Finally, our Phase I analysis of the thrust augmentation system using multi-fluid codes was very promising, indicating that sufficient thrust and specific impulse can in fact be generated. We proposed to build on these results with experiments on the PFRC-2 testbed, using an existing gas puff valve that has to date gone un-utilized. This will allow us to further explore and validation the dynamics of the interaction of the scrape-off-layer (SOL) flow with the FRC.

Our Phase II study therefore had the following objectives:

- continue research on the superconducting magnets
- refine the shielding analyses
- investigate a highly efficient RF subsystem design concept using switching (class E) amplifiers
- create a synchrotron model that is specific to our magnetic configuration
- analyze the nozzle magnet geometry and its effect on thrust
- evaluate experiments relating to the thrust augmentation system.

Figure 6 shows a block diagram of the system components with the targeted subsystems indicated using task numbers.

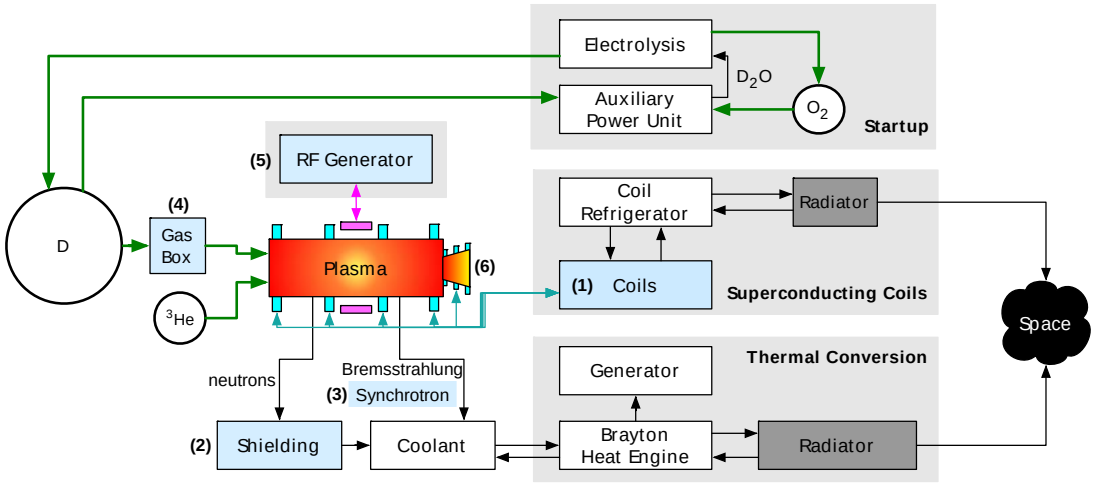

Figure 2 DFD System Components. *This diagram identifies key components and subsystems of the engine. Those marked (1)-(6) will be studied in Phase II.*

The Phase II tasks were:

1. **Magnets**. Continue to investigate the current state of the art in both low and high temperature superconductors and develop design tools that can trade conductor mass, structural mass, cooling mass, and shielding mass to find an optimum material and operating temperature;
2. **Shielding**. Refine the shielding analyses by including different elements and compositions and updated evaluations based on neutron irradiation experiments; and
3. **Synchrotron**. Develop a new synchrotron model specific to our FRC configuration;
4. **Thrust Augmentation Experiments**. Analyze thrust augmentation experiments on the PFRC-2 at PPPL using a pulsed gas valve to inject gas into its gas box, increasing the density there 10-fold or more, and investigate how the gas flows around the FRC;
5. **RF Subsystem**. Explore the use of a switching RF heating system and quantify the expected efficiency;
6. **Closed Loop Mode**. Evaluate the requirements of a propellant-capture mode
7. **Design Update**. Update the engine, nozzle, and spacecraft design for the Pluto mission and other selected deep space missions

Approximately 1100 hours were allocated annually to PSS staff for the modeling and system analysis and 320 hours for PPPL's Dr. Cohen and for other staff. A $20,000 subcontract was allocated to Dr. Minervini in year 1 as a consultant on the superconducting coils task. $15,000 was reserved for creating a project video and $2,000 was allocated for the PI to travel to the two NIAC symposiums.

2.2 Princeton Field-Reversed Configuration (PFRC) Reactor

The Direct Fusion Drive concept is an extension of ongoing fusion research at Princeton Plasma Physics Laboratory dating to 2002. Princeton Field-Reversed Configuration machines (PFRC)

employ a unique radio frequency (RF) heating method invented by Dr. Samuel Cohen. Studies of electron heating with this method have surpassed theoretical predictions and experiments to measure ion heating in the second-generation machine are ongoing.

A full-sized PFRC is perfectly suited to use as a rocket engine for two reasons: one, the configuration results in a radical reduction of neutron production compared to other D-^{3}He approaches; two, the reactor features an axial flow of cool plasma to absorb the energy of the fusion products. Adding propellant to this flow results in a variable thrust, variable specific impulse exhaust through a magnetic nozzle. We call this process *thrust augmentation* of the reactor. Approximately 35% of the fusion power goes to thrust, 30% to electric power, 25% lost to heat, and 10% is recirculated for the RF heating.

The current one-quarter-scale machine, the PFRC-2 with a plasma radius to 7 cm (see Figure 3), is designed to demonstrate electron and ion heating. At an applied RF heating power of about 20 kW, electron heating to temperatures $T_e > 300$ eV has been demonstrated, see Figure 4. Ion heating studies will follow, once $T_e > 1$ keV has been achieved. Pulse lengths of 300 ms have been reached. The main axial-field water-cooled magnets, in conjunction with eight high-temperature superconducting internal flux conservers can produce a central internal field of 1.2 kG. (An operational PFRC would have a field of 70 kG). The RF heating system has been upgraded to 200 kW. Additional diagnostics have been added, a notable one being a soft X-ray pulse-height spectrometer with a spectral range of 0.25-10 keV, an energy resolution of 9% at 525 eV and 1% at 5.9 keV, and a count rate capability to in excess of 10^6/s. Probes are used to measure SOL properties.

Figure 3. PFRC-2 in operation. This photo captures a pulse; the plasma is white inside a Lexan vacuum vessel. An external RF antenna can be seen as Kapton-tape wrapped horizontal square figure-8's.

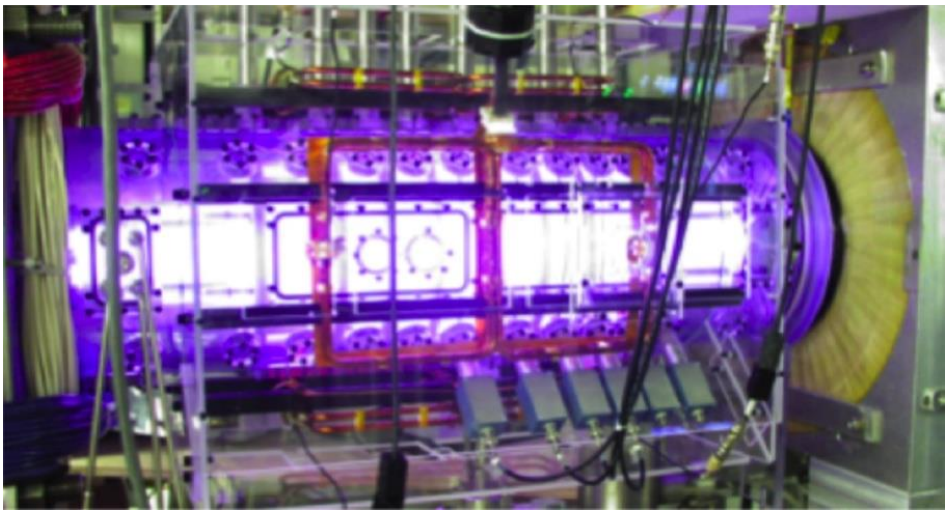

Figure 4. X-ray spectrum from a recent PFRC-2 RMF run. The tail electron temperature reached over 500 eV and the bulk temperature over 300 eV. [Courtesy C. Swanson and P. Jandovitz]

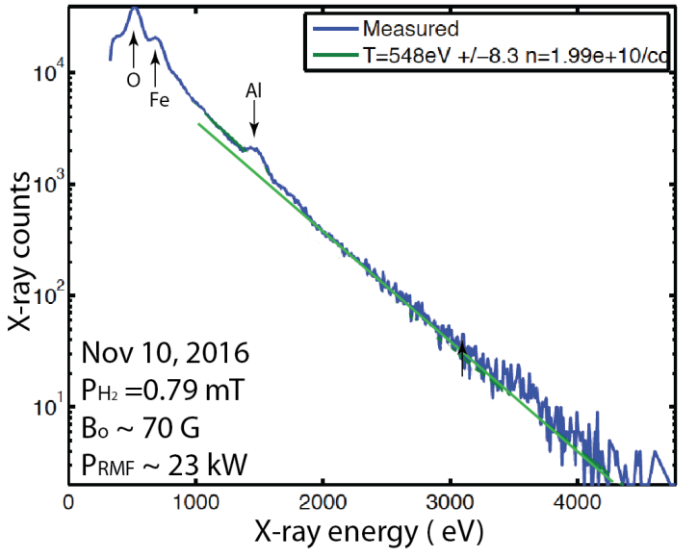

2.3 Modeling Tools

2.3.1 Software Packages

The following software are used to analyze the PFRC configuration and operation:

1. **LSP** - This is a 3-D electromagnetic particle-in-cell code for Large Scale Plasma simulations. This is commercial software owned by Orbital/ATK and run under a PPPL license. This code has been used to study FRC formation by RMF, RMF penetration, plasma heating, and fast-ion slowing down in cool magnetized plasmas. It requires significant supercomputer time, typically 10^5 cpu-hrs per run.
2. **UEDGE** - This 2D multi-species fluid code predicts electron and ion temperatures based on a specified magnetic configuration and plasma, neutral gas, and power input. Lawrence Livermore National Lab staff wrote and maintain this code.[1]
3. **RMF** - This Hamiltonian code, authored by Alan Glasser, models single-particle heating in 3-D with specified magnetic fields, *e.g.*, FRCs and RMF.
4. **ATTILA** – a comprehensive radiation transport environment. This code is used to model radiation effects in ITER, including neutron transport, activation, and defect generation.

[1] (T.D. Rognlien, 2000)

5. **FieldCoils** – Determines the magnetic field magnitudes and lines given a set of driven electromagnets, assumed FRC plasma currents, and reactive flux conservers.
6. **GS Solver** - Self-consistently determines the plasma current assuming ideal MHD equilibrium by assuming a relationship between plasma pressure and enclosed flux.
7. **ANSYS** – Used for structural calculations of the magnets.

ATTILA was used in prior work to generate shielding thicknesses based on certain neutron power and acceptable neutron fluences. UEDGE was used during this study to generate new simulation results for thrust and specific impulse as a function of input power and gas flow rate. RMF and LSP have been used in prior work to build the theoretical foundation of PFRC operation including detachment in the terminating magnetic nozzle.

The GS Solver is more accurate than FieldCoils for modeling fields in the PFRC because the plasma current and electromagnets can feed back on each other to create a self-consistent magnetic field. FieldCoils can also determine forces between magnets and flux measurements of diamagnetic loops.

For more details see Appendix A which has a detailed technical description of the PFRC.

2.3.2 Spacecraft Control Toolbox: Fusion Propulsion Module

This software packaged was initially developed using internal research and development funds. It includes the following tools:

- plasma physics utilities
- fusion reactions including the power released by each species and cross-sections
- Bremsstrahlung and synchrotron radiation models
- magnet sizing using Virial and shell methods
- power conversion system sizing [4]
- tools for sizing shielding and cryogenic cooling systems
- point reactor designs [5]
- rectilinear mission planning

During phase II we added a new electromagnetic field code for studying the plasma heating. It includes a single-particle trajectory integrator and runs in the MATLAB environment. It allows for any coil configuration and any current waveforms. We have new models for a conduction-limited regime divertor for the closed-loop PFRC. There are also extensive tools for sizing both HTS and LTS magnets.

3 Results

The results are presented in order of the Phase II tasks.

3.1 Superconducting Magnets

From the Phase II Proposal:

> Our Phase I analysis has made it clear that there is rapid development ongoing in superconductor technology and a single best design path is not yet clear. There are multiple low and high temperature superconductors available and under development, with properties that vary dramatically with temperature. Particularly important are the cross section of the conductor wire (tape or round) and the fraction of the structural load (typically 50 MPa/coil) the conductor and its substrate can bear. We must consider the mass of the conductor, structural components, cooling subsystem, and shielding mass, where the response of the superconductor to the radiation depends on operating temperature. Second-generation HTS in tape form are becoming available that are half the thickness of the original, providing important savings in mass. Documentation available from the manufacturers indicates that they are pushing the size of the required substrate down.
>
> More detailed information is needed on the various materials in play. We propose spending additional time gathering information and leveraging a small consultant contract with a superconductor expert. This will enable us to create a design tool that can assess the effect of operating temperature on total mass including the shielding and cooling components.

3.1.1 Superconducting Materials Properties

There are several new publications presenting results in irradiation of various superconductors [6] [7] [8] [9]. In the end, the conclusion is that low-temperature superconductors and high-temperature superconductors operated at low temperatures will have similar total neutron fluence limits on the order of 1e23. High-temperature superconductors see a performance *increase* at moderate fluence of about 2e22 but at higher fluences they degrade like any other material.

Table 1. Example Superconductor Parameters

Materials	Temperature	Field	Critical Current	Density
NbTi 1.3:1, 1.04 mm bare wire	4.2 K	5 T	880 A	5.9 g/m
	4.2 K	7 T	550 A	
SuperPower 12 mm 2nd gen HTS	20 K	5 T	1220 A	4.8 g/m
	20 K	7 T	955 A	
	45 K	5 T	519 A	
	45 K	7 T	390 A	
	4.2 K	20 T	650 A	
	10 K	20 T	831 A	
Bruker NbSn 1.1 mm	1.8 K	20.5 T	356 A	6.7 g/m

Figure 5 shows experimental data from Fischer for a single tape from SuperPower, indicating that critical current increases at low fluence, then decreases. For these experiments, "fast" neutrons are defined as E > 0.1 MeV. The transition temperature decreases about 3% per 10^{22} m^{-2}.

Figure 5. Impact of Fast Neutron Irradiation on HTS Tape Critical Current at Different Operating Temperatures, D. X. Fischer, 2018 [10]

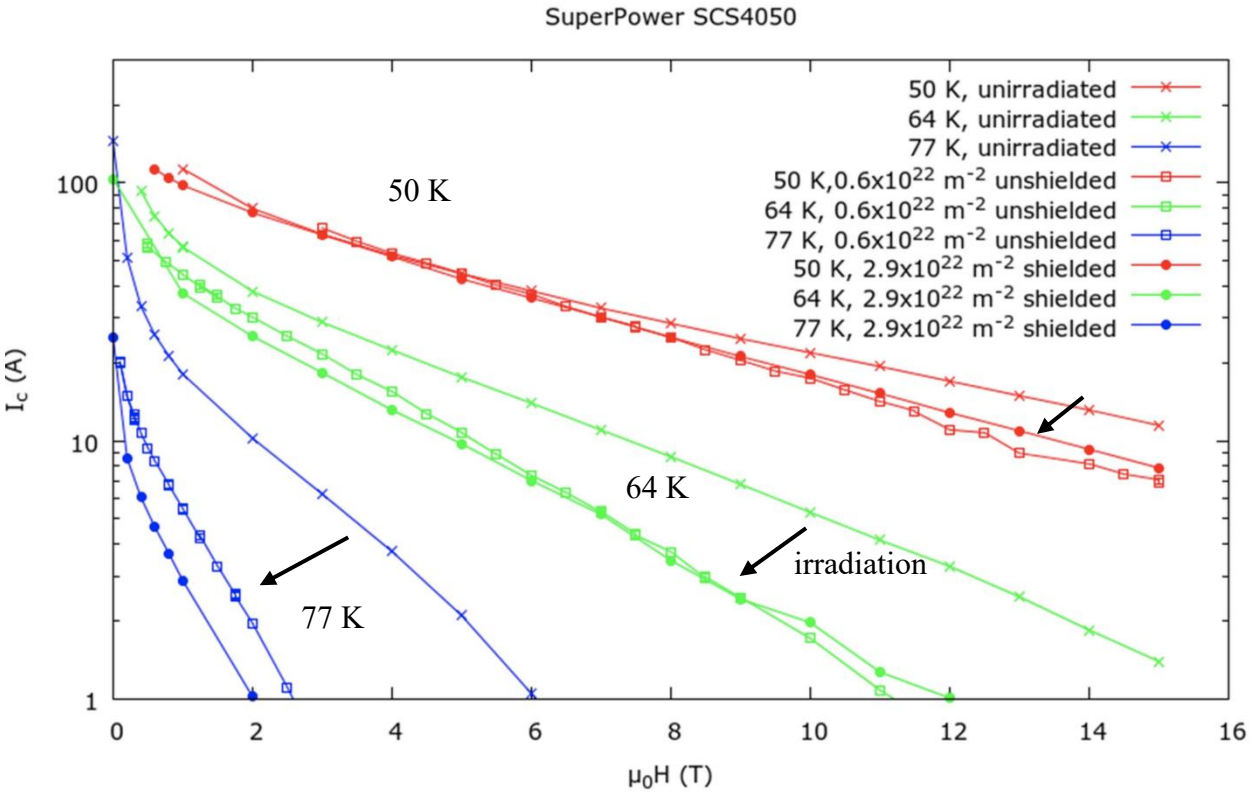

Figure 6 from Fischer shows a comparison among tapes from three manufacturers. The SCS tapes are samples from SuperPower, with the "AP" tapes having artificial pinning centers. The 344C tapes is from American Superconductor. SuNAM is a Korean manufacturer.

3.1.2 Consultant Contract – Dr. Minervini

Dr. Minervini developed a pancake magnet sizing model suitable for high-temperature superconducting tape. He also provided the latest experimental data from his lab on critical current in a high-temperature superconducting tape. Table 2 and Table 3 show the input and out tables from the Excel pancake magnet model.

Figure 6. HTS Critical Currents Increase than Decrease as a Function of Fast Neutron Fluence, D. X. Fischer, 2018 [10, 11]

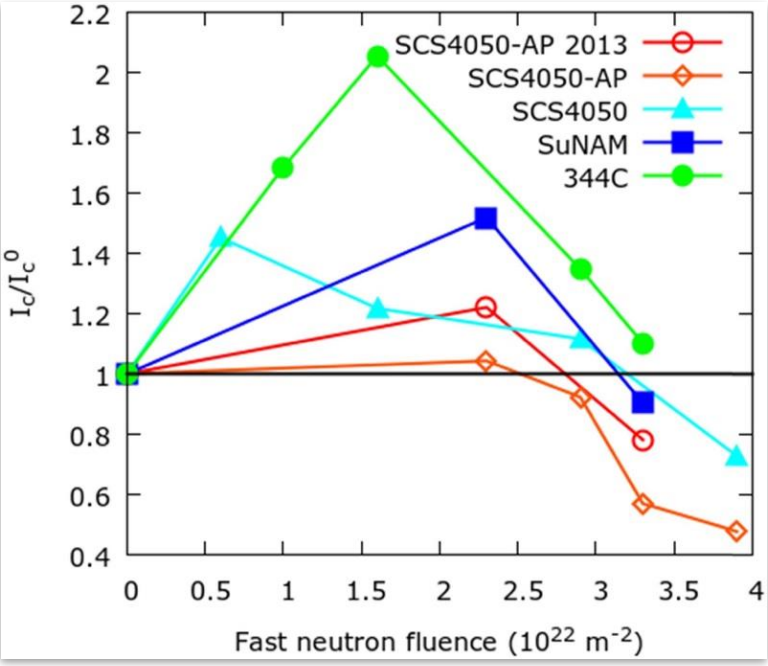

Table 2. Pancake Magnet Model Inputs

Inputs	Units	Symbol	Value
Coil Geometry			
Coil Inner Radius	m	Ri	0.4
Coil Outer Radius	m	Ro	0.48
Type of Winding			Double Pancake
Number of Double Pancakes		Ndp	4
Insulation Thickness on Tape	mm	Ti_tape	0
Insulation Thickness Between Pancakes	mm	Tp	0.5
Insulation Thickness Between Double Pancakes	mm	Tdp	1
Conductor Density	kg/m^3	Rho-cond	8000
Tape Geometry			
Tape Width	mm	Wtape	12
Copper Plating Thickness	m	Tcopper	5.00E-06
Substrate Thickness	m	Thastalloy	4.00E-05
Tape Thickness	m	Ttape	5.00E-05
Insulated Tape Thickness	m	Ttape_total	5.00E-05
Insulated Tape Width	mm	Wtape_total	12.00
Operating Conditions			
Tape Operating Current	A	Iop	**190**
Operating Temperature	K	Top	50

Table 3. Pancake Magnet Model Outputs

Outputs	Units		Value
Conductor and Coil Parameters			
Coil Radial Thickness	m	Wcoil	0.08
Total Coil Height	m	Hcoil	0.098
Number of Turns/Pancake		Ntp	1,600
Total Number of Turns in a DP		Ntdp	3,200
Tape Length/Double Pancake	m	Ldp	8,846
Total Length of Tape	m	Ltape	**35,384**
Coil Radius Ratio		Alpha	1.20
Coil Length Ratio		Beta	0.12
Coil Current and Current Density			
Coil Ampere-Turns	A-T	NIop	**2.43E+06**
Overall Coil Current Density	A/m^2	Jcoil	3.10E+08
Magnetic Fields			
Central Field on Axis	T	Bo	**3.46**
B Peak Ratio (Bmax/Bo)		Bp-Ratio*	*1.15*
Maximum Field at Coil Inner Radius	T	Bmax	3.98
Critical Current			
Critical Current	A	Ic*	*900*
Fraction of Critical		Iop/Ic	0.211
Volume and Mass			
Coil Volume	m^3	Vcoil	2.17E-02
Coil Mass	kg	Mcoil	**173.40**

Figure 7 shows the pancake model output for example nozzle magnet designs. *N* is the number of double-pancakes in the model. Each pancake is the width of the tape plus a small margin for insulation. The magnet field target is either 8 to 9 T for a PFRC-3 machine or 16-20 T for a reactor-scale PFRC-4 machine. This table assumes an operating current of 400 A.

Figure 7. Pancake Model Outputs for Nozzle Magnet

Nozzle Coils - assume 400 A

Radius (cm)	Outer (cm)	Height (cm)	N	Width (cm)	Field (T)	Mass	Length (m)	Current	Model
6.5	15	8.5	1	2.45	8.3355	11.25	2296	1.36E+06	PFRC-3
6.5	10	3.5	2	4.9	8.2777	7.11	1450	1.12E+06	PFRC-3
6.5	9	2.5	3	7.35	8.8358	7.16	1458	1.20E+06	PFRC-3
15	26	11	3	7.35	16.3	83.31	17001	5.28E+06	PFRC-4
15	23	8	4	9.8	16.6	74.88	15280	5.12E+06	PFRC-4
15	25	10	4	9.8	19.89	98.52	20104	6.40E+06	PFRC-4
15	23	8	5	12.25	20.37	93.59	19100	6.40E+06	PFRC-4

Note that the dimensions of magnets (i.e. the conductor windings) are about 5 cm x 3.5 cm for 8.6 T and 10 cm x 10 cm for 20 T. The 20 T magnet requires 20 km of tape! Figure 8 shows the critical currents measured for actual HTS tape at MIT. The lowest line is for a nozzle-level field of 20 T. In order for the critical current to be near 400 A, the temperature must be less than 20 K.

Since the magnets should operate at about 60% of the critical current, the actual nozzle operating temperature must be lower still.

Figure 8. HTS Tape Critical Currents for Fields from 2 to 20 T (Data: J. Minervini)

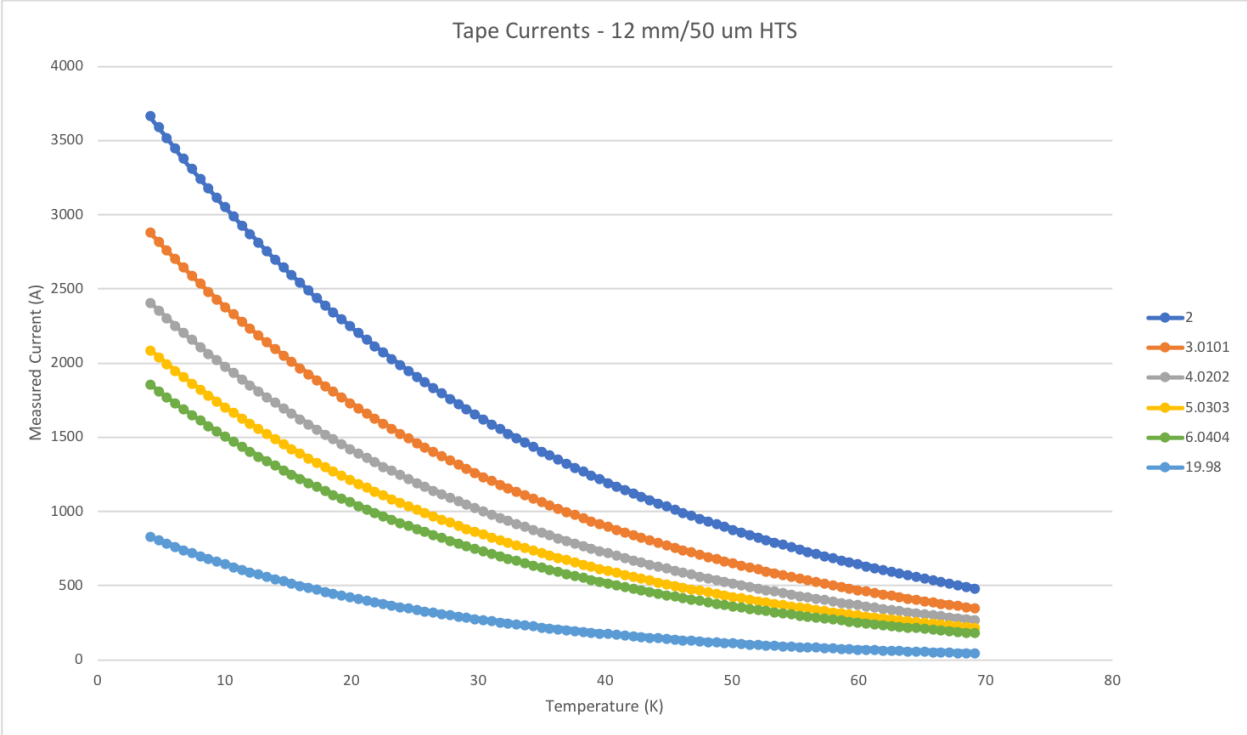

3.1.3 Magnet Design Tools

We have developed several tools in MATLAB that can be used to size the magnets for a PFRC machine given the desired axial field strength and mirror ratio.

Grad-Shafranov Solver

A Grad-Shafranov solver is a method for calculating a plasma equilibrium iteratively. In this case, we define the physical locations of the magnets and assign an initial active current. The solver computes the plasma currents necessary to reverse the field assuming a rigid rotor model for the resulting FRC. The user specifies either the radius or the length of the FRC and the solver computes the other. Through this tool we compute the induced currents in the magnets, resulting in the total current load each magnet must carry. We can then use the pancake sizing tool for HTS or a similar method for LTS wire to calculate the amount of superconductor needed and the mass of the windings.

Figure 9. Grad-Shafranov Equilibrium for an Elongated PFRC

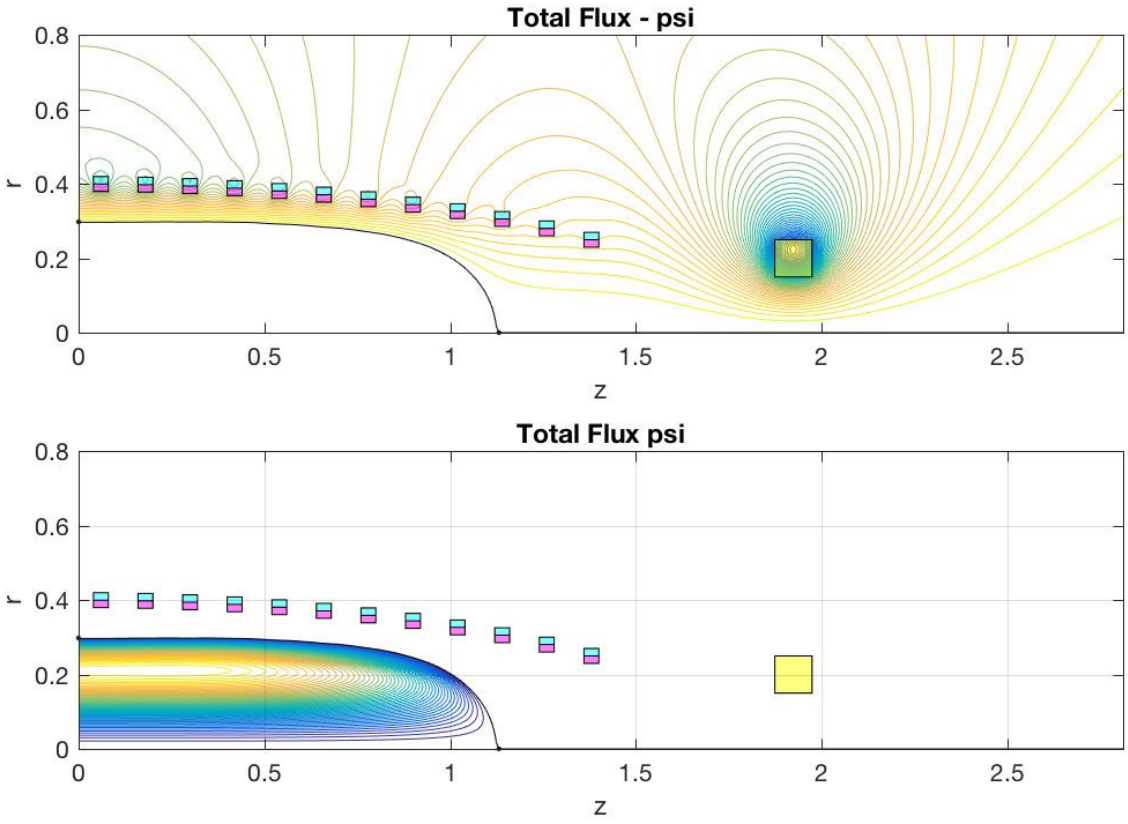

In applying this tool to the PFRC, we learned that the initial currents in the magnets must taper from the midplane to the ends, and that the induced currents will similarly taper along the FRC's length. The distance between the nozzle magnet and the last axial magnet impacts the elongation that can be achieved. If the magnetic field does not taper sufficiently, the FRC collapses into a spherical configuration. Figure 10 shows an example of the vacuum field of a "long" PFRC, showing the taper of the field along the machine axis approaching the nozzle magnet, which in this case is 16 T.

The equilibrium solver starts with the initial magnet currents and iterates on the FRC current until an equilibrium is found, from which the induced currents can be computed. This is depicted in Figure 11, where the vacuum, induced, and total currents for an equilibrium are plotted. The initial or vacuum currents (before there is plasma) taper linearly. The induced currents are, in the center, even greater than the initial currents. The magnet currents fall off sharply along the FRC's length.

Figure 10. PFRC-4 Grad-Shafranov Vacuum Scan

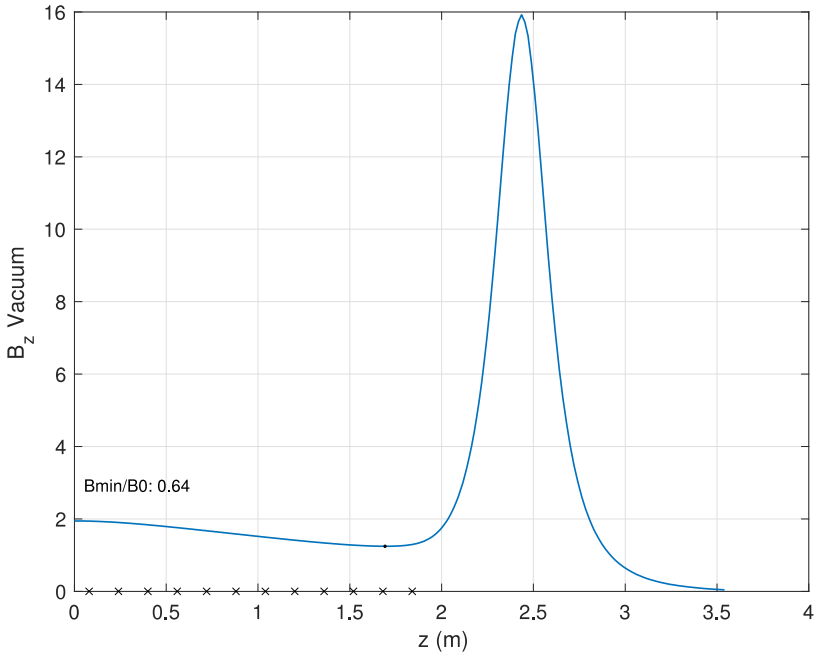

Figure 11. Vacuum and Induced Currents in the Magnets

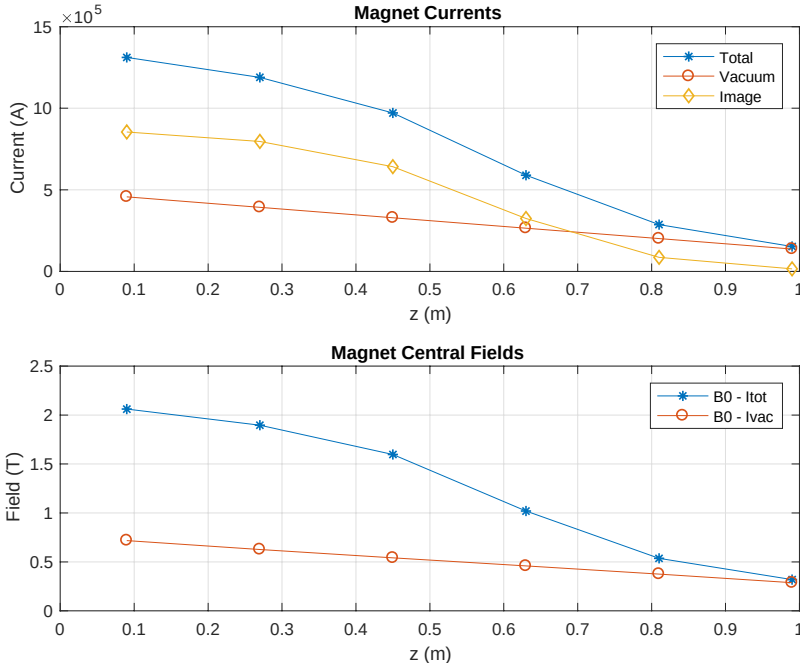

Figure 12 shows how reducing the "taper" in the magnet initial currents shrinks the elongation of the resulting FRC. In this figure, I_{min} is I/I_0, the fraction of the central magnet's current I_0 that is initialized in the last magnet.

Figure 12. Grad-Shafranov Magnet Current Taper Study

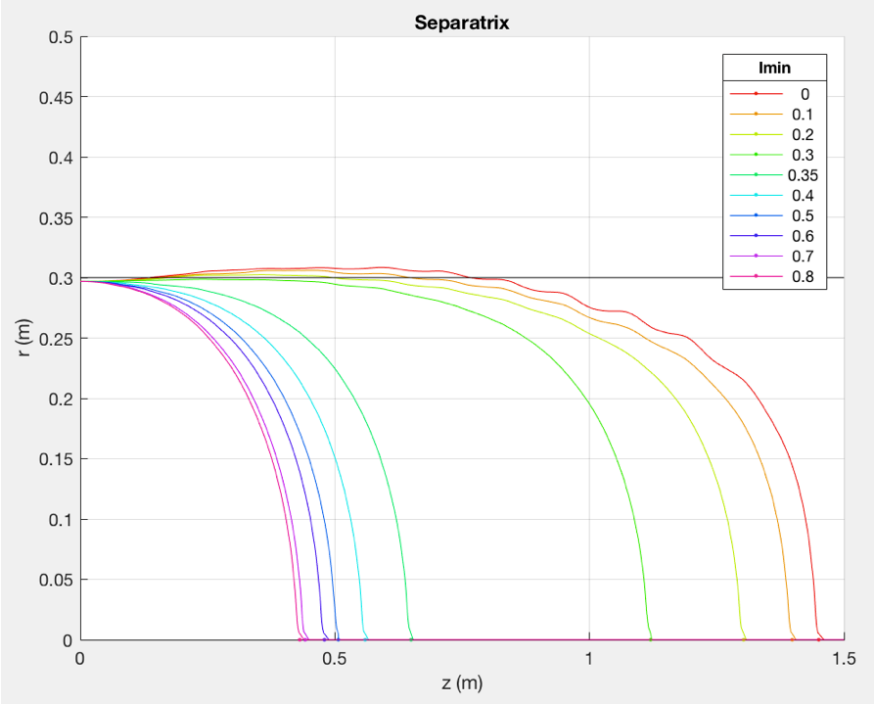

The spacing between the axial magnets also has an impact on the elongation that can be achieved. We found generally that the spacing needs to be less than one-half the magnet radius. Table 4 shows example output from the Grad-Shafranov solver for an 18 cm spacing between magnets that have a 40 cm mean radius. Table 6 gives the corresponding parameters of the FRC. Note that while total central field in the FRC is 5.4 T, the maximum field of the inner magnet (#1) by itself, it's central field, is less than 2 T. Note that a complete PFRC has two of each magnet, plus the nozzle magnets. The nozzle magnet parameters are given in Table 5, where the Z location is important.

Table 4. Grad-Shafranov Computed Magnet Currents

Magnet	Radius (cm)	Field (T)	Current (kA)
1	40.0	1.784	1,136
2	39.4	1.681	1,054
3	38.2	1.437	874
4	36.3	0.969	560
5	33.7	0.527	283
6	30	0.320	153

Table 5 Grad-Shafranov Input Nozzle Parameters

Nozzle Magnet	Value
Radius	13 cm
Field	16 T
Current	5.6 MA
Z location	1.57 m

Table 6. Grad-Shafranov Computed FRC Parameters

FRC Parameters	
Plasma current	10 MA
Radius	28.3 cm
X-point	75 cm
B vacuum	2.2 T
B_0 (w/plasma)	5.4 T

Figure 13 shows the magnet locations and fieldlines for this example.

Figure 13. Six Magnet Grad-Shafranov Solution

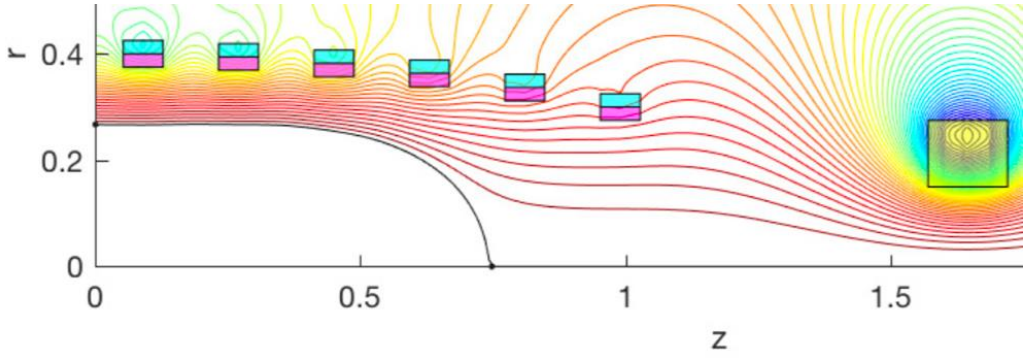

Magnet Thermal Analysis

The overall layout of the fusion reactor is shown in Figure 14. Reactor layout. The reactor is thermally isolated from the coils. As will be shown, radiative heat transfer will be very small.

Figure 14. Reactor layout

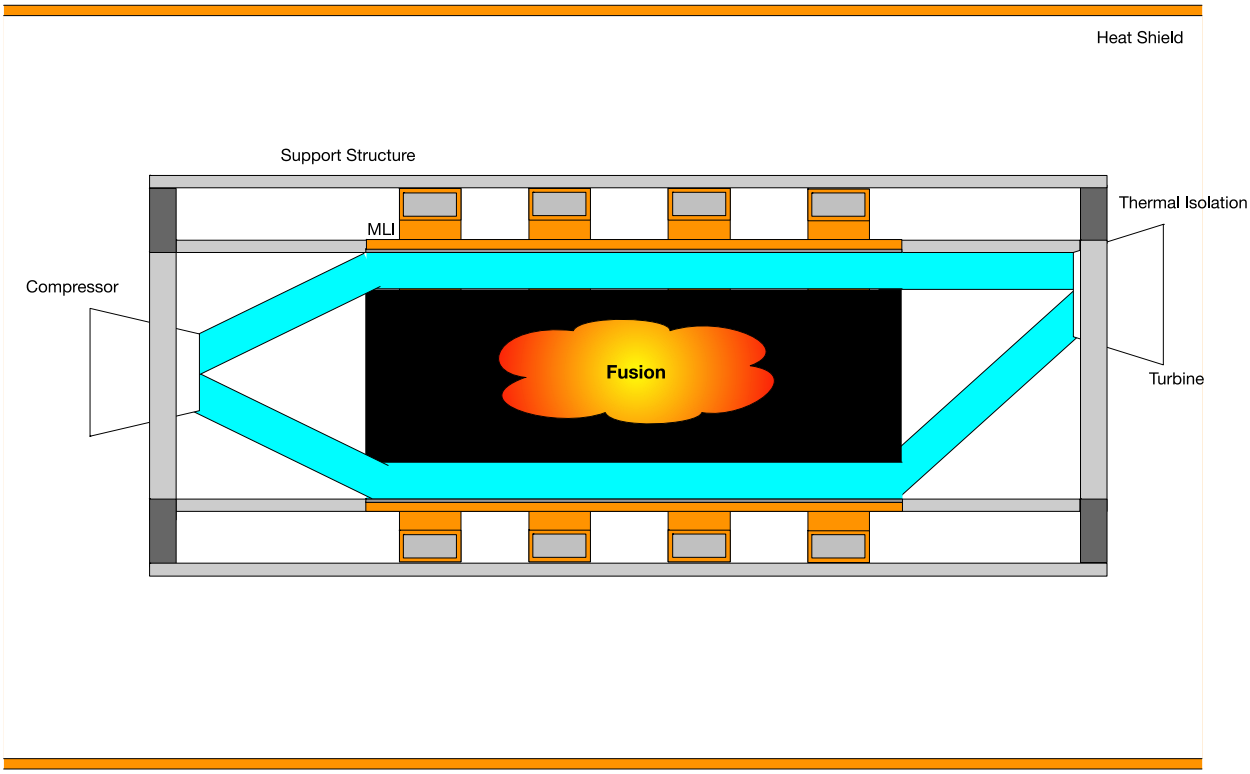

MLI insulation is used between the heat exchanger and the superconducting coils. We did not account for the thermal conductivity of the shielding which will also reduce the heat flux. The particular shell temperatures are for demonstration purposes only. They do not reflect a complete system design that would include the cooling requirements for the superconducting coils, the mass of the coil cryocoolers and the power requirements of the cryocoolers. There will be optimal value that will minimize the contribution of cooling to the specific power of the rocket engine.

The analysis was solely based on radiation heat transfer. There will be some leakage through the structure but that will be minimized by including thermal breaks.

The heat exchanger is shown in Figure 15. This is similar to a rocket engine nozzle cooling jacket. The heat transfer model includes optimal multi-layer Insulation (MLI) thicknesses. It also included a model of the convection heat transfer.

Figure 15 Heat Exchanger Schematic with Ducts

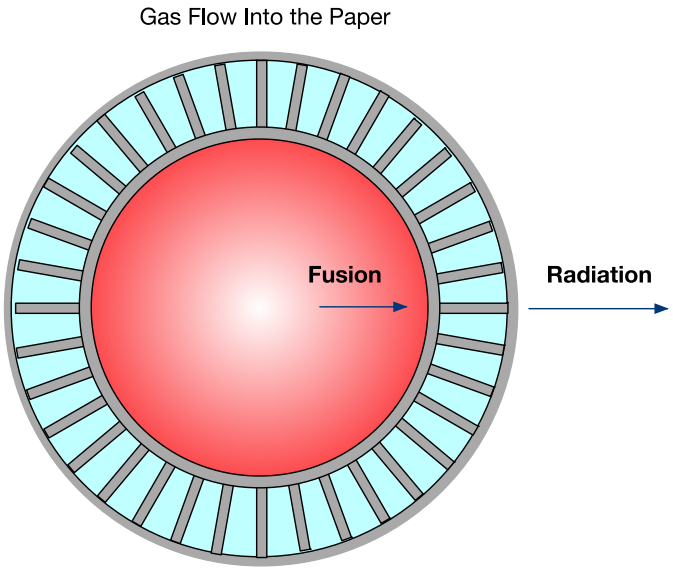

The heat exchanger is made of ceramic. The actual types of material will depend on the outlet temperature. If the outlet is directly to the turbine material limits for solid uncooled ceramic blades limits it to under 1600 deg-K. If we use a direct conversion system at the outlet, we can go over 2000 deg-K. This would increase the Carnot efficiency of the system.

The total heat transfer is the sum of the heat emitted by the outer shell and that emitted by the fusion reactor. The outer shell produces 0.07 W/m^2. The peak radiation flux from the fusion chamber is 170 W/m^2 at the hot end of the reactor. Using the same 200-layer blanket we get the results in Table 7. Adjust the number of layers of MLI in the fusion blanket can reduce the temperatures.

Table 7. Coil heat transfer results.

Parameter	Value	Units
Outer shell temperature	177.80	deg-K
Inner shell temperature	27.24	deg-K
Inner shell flux	6.24×10^{-3}	W/m^2
MLI conductance	4.14×10^{-5}	W/m^2

Magnet Sizing Methods

We use Dr. Minervini's pancake model for sizing the nozzle magnets. This computes the number of turns needed to produce a field given the number of layers in the pancake, and hence the mass. For LTS magnets, we simply pack the turns of round wire into a square cross-section using a packing fraction of 0.9069.

For all magnets, we assume that they operate at approximately 60% of the critical current for the given peak magnetic field and operating temperature. Table 8 gives the superconductor properties used

Table 8. Selected Superconducting Wire Properties

	Model	Wire Size	Density	Temperature	Peak Field	Critical Current	Operating Current
HTS	Superpower SCS12050	12 mm wide 0.1 mm thick	8,000 kg/m^3	10 K	20 T	651 A	400 A
				45 K	5 T	520 A	300 A
LTS	SuperCon NbTi	1 mm diameter	7500 kg/m^3	4.2 K	5 T	700 A	528 A

Table 9 shows the comparison between HTS (at 45 K) and LTS for hypothetical magnets of the given current, assuming a magnet inner radius of 40 cm. The wires are assumed to operate at 60% of their critical current in field of 5 T, 528 A for the LTS and 300 A for the HTS as shown in Table 8. The HTS number of turns is the total in all pancakes. The HTS mass calculation uses an aggressive substrate estimate of 30 um, 20 um less than the tape that is commercially available but in use experimentally, for a total tape width of 0.045 mm. [11]

Table 9. LTS and HTS (45 K Mass Comparison

Current	HTS Turns	Dimensions	HTS Mass	LTS Turns	Coil Width	LTS Mass
500 kA	1666	2.4 x 3.8 cm	18.94	947	3 cm	15.73
1 MA	3333	4.8 x 3.8 cm	37.89	1,894	4.2 cm	31.92
2 MA	6666	7.2 x 5 cm	76.91	3,788	6 cm	65.17
5 MA	16,666	7.2 x 12.5 cm	209.2	9,470	9.4 cm	169.5
10 MA	33,333	12 x 15 cm	429.8	18,940	13.3 cm	353.8

As can be seen, the LTS winding are less massive.

Cryocooler Sizing Methods

We have developed new functions for sizing cryocoolers using curve fits to published mass and power data. [12] [13] ter Brake's survey from 2002 includes 235 (terrestrial) cryocoolers operating between 4 and 120 K. He notes that since the 1990s, lifetime of Stirling coolers has increased by an order of magnitude to typically 5 years or more. He gives a fit for the mass as a function of lift power Q_c and cold tip temperature:

$$\text{mass} = \alpha(T) \times Q_C^{\beta(T)}$$

where the coefficients are given as

$$\alpha(T) = 157\exp(-0.0533\mathrm{T})$$

$$\beta(T) = 0.009T + 0.1275$$

The model will compute a mass for any input power, so the user must use judgement in associating a power with a temperature – at 4 K, a cryocooler can remove perhaps 0.1 to 1 W, while at 80 K, a cooler could lift thousands of watts. Figure 16 shows the model for the temperatures given in the reference, with two different power scales.

Figure 16. Cryocooler Mass Scaling (ter Brake)

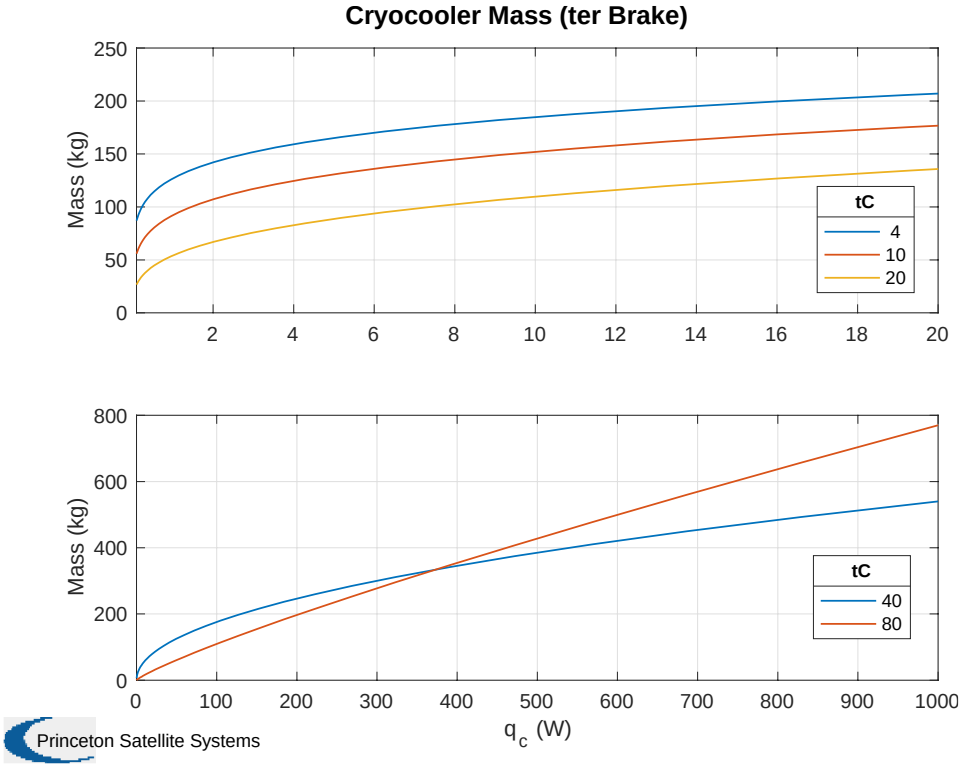

This paper also gives an overall fit for mass as a function only of power, independent of operating temperature. This fit is given as

$$\mathrm{mass} = 0.0711P^{0.905}$$

This simple model does have a basis in cooler design. Most of the mass of Stirling and Pulsed Tube coolers is in the compressor, which is sized for the input power. In Brayton coolers, the mass driver is the heat exchanger, which is also sized from the input power. [14]

With this information, we can compute the mass of a coil with the cryocooler included as a function of temperature, for an assumed lift power. For example, assuming a lift power of 5 W, Figure 17 shows that the minimum mass is achieved using a temperature of about 20 K, using

parameters for a PFRC nozzle coil with HTS (15 T, 15 cm inner radius). The cryocooler mass at this temperature is nearly equal to the windings mass.

Figure 17. Nozzle Coil Cryocooler Mass Analysis. Lift Power of 5 W

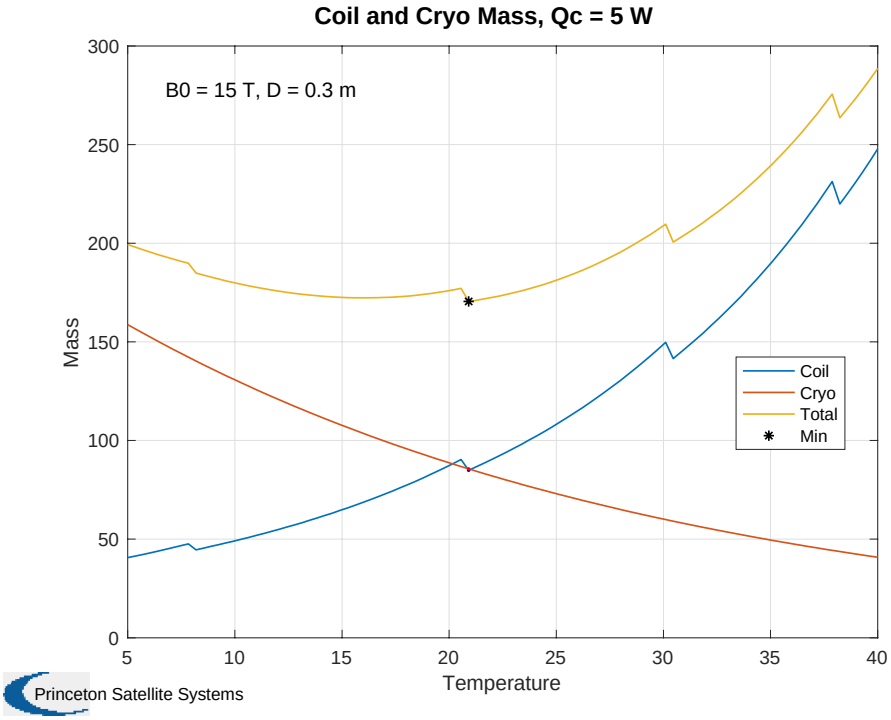

If the cryocooler were only lifting 1 W, the total mass drops from 170 kg to 135 kg and the optimal temperature to 15 K.

The axial magnets, if built using LTS, are constrained to operate at 4 K. Figure 18 shows the ter Brake model at 4 K for a lift power from 0.1 to 10 W. The input power at 10 W is less than 10 kW, while the cryocooler mass ranges from 100 to 180 kg.

The axial magnets could also be built from HTS and given the more modest field constraints could plausibly be operated at a higher temperature, decreasing cryocooler mass. Due to their proximity, multiple magnets can likely be served by a single cryocooler. Figure 19 shows an example tradeoff with a single 2 T magnet and cryocooler pair, with a lift power of 5 W. If the same lift power can instead serve multiple magnets, the optimum temperature skews colder.

Figure 18. ter Brake Cryocooler Model for LTS at 4 K

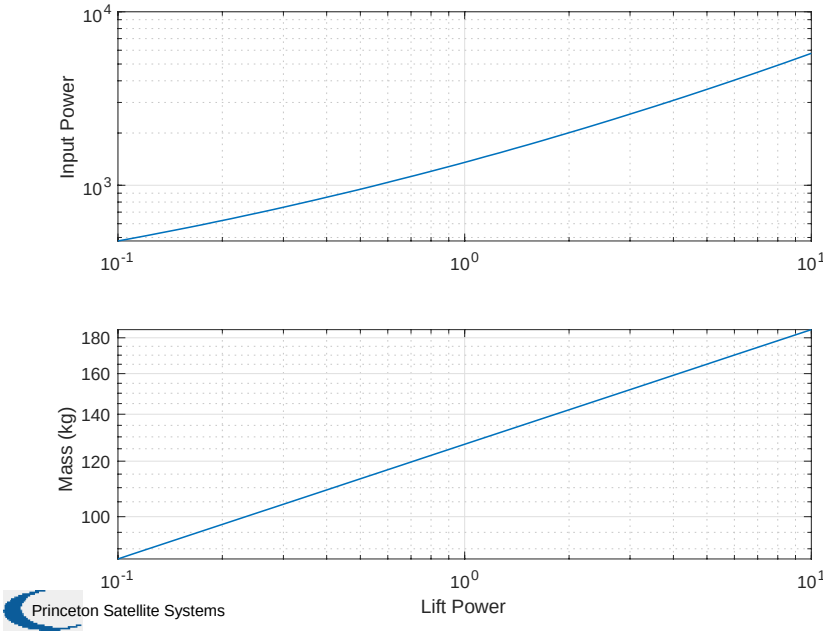

Figure 19. Axial Magnets HTS with Cryocooler. Lift Power of 5 W

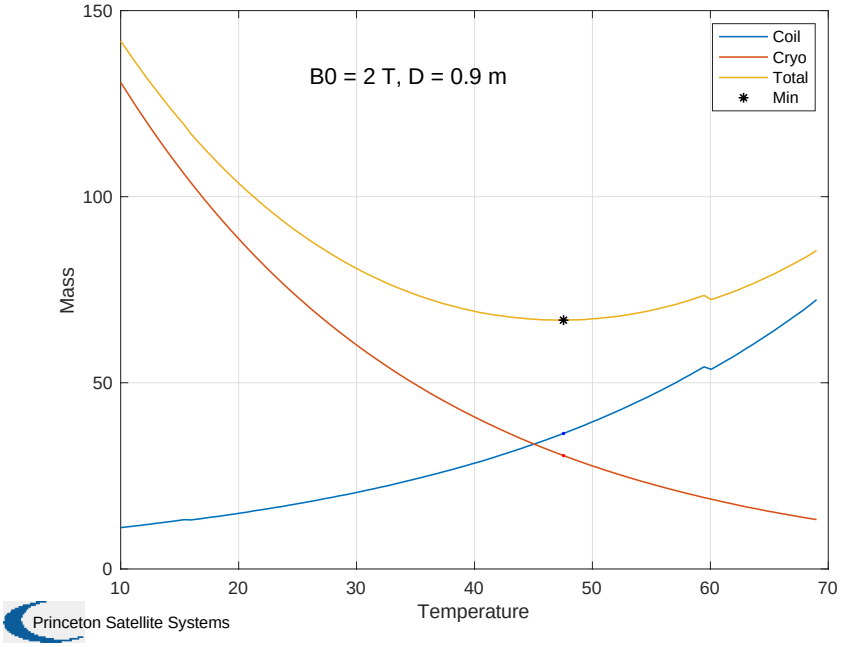

These models will overestimate the mass for a space cryocooler, where efforts are made to minimize mass. For example, Northrop Grumman has a high-capacity three-stage cryocooler with a compressor mass of 18.7 kg which can lift 0.1 W at low temperature [15], but the lightest cooler in ter Brake's model at 4 K is 100 kg. This is comparable to the compressor of the terrestrial cryocooler that will be used in our 0.5 T test LTS magnet.

3.1.4 Magnet Design Conclusions

Table 10 shows magnet masses for an FRC using the Grad-Shafranov solver to compute currents, with LTS axial magnets and HTS nozzle magnets.

Table 10. Six-Magnet FRC Design, LTS + HTS

Magnet	Radius (cm)	Field (T)	Current (kA)	Wire	Mass (kg)
1	40.0	1.784	1,136	LTS @ 528 A	38.9
2	39.4	1.681	1,054	LTS @ 528 A	34.7
3	38.2	1.437	874	LTS @ 528 A	27.3
4	36.3	0.969	560	LTS @ 528 A	15.6
5	33.7	0.527	283	LTS @ 528 A	7.0
6	30	0.320	153	LTS @ 528 A	3.3
Nozzle	13	16	5,600	HTS @ 400 A	69
Total Mass					**391 kg**
Cryocooler	**Lift Power (W)**		**Temp (K)**		
Axial	5		4.2		163.8
Nozzle (2)	0.5		10		79.24
Total Mass					**712.8 kg**

Table 11. Six-Magnet FRC Design, All HTS at 10 K

Magnet	Radius (cm)	Field (T)	Current (kA)	Field	Current	Mass (kg)
1	40.0	1.784	1,136	5 T	1030 A	13.5
2	39.4	1.681	1,054			12.4
3	38.2	1.437	874			10.0
4	36.3	0.969	560			6.06
5	33.7	0.527	283			2.82
6	30	0.320	153			1.35
Nozzle	13	16	5,600	20 T	400 A	69
Total						**230 kg**
Cooler	**Lift Power (W)**					
Axial	5					130.75
Nozzle (2)	0.5					79.24
Total Mass						**518.75 kg**

As can be seen, when the cryocoolers are included, there is the potential for additional mass savings by building the axial magnets out of HTS if run at 10 K, the same temperature as the nozzle coils. We do not yet know an exact lift power budget for the cryocoolers, but it is clear that using fewer cryocoolers with higher lift power should provide mass savings.

The structural mass to react the axial loads between magnets is only expected to be a few kg. The nozzle magnets will require additional circumferential support as the stresses predicted by ANSYS for a 20 T coil are over 800 MPa.

3.2 Shielding Design

From the Phase II Proposal:

> In Phase I, we assumed particularly conservative values for neutron flux, neutron spectrum, and HTS resiliency to neutron irradiation. The DFD should produce 10× lower neutron fluxes than we assumed in Phase I and the HTS should tolerate 10× higher fluences. Moreover, we restricted our analyses to B_4C shielding, based on its mechanical and electrical properties, particularly at high temperature. Other materials merit consideration, such as B_4C/H_2O mixtures, pure B, and LiH. Earlier studies indicted these could provide at least a 20% reduction in mass. For our Phase I study, the shielding mass was up to 40% of the rocket mass. A large improvement in specific power could be seen through shielding trade-off studies. Shielding thickness will have to be balanced against the mission duration.

Shielding is without question a big driver of specific power. If the shielding between the plasma and superconducting magnets cannot be reduced to 10 cm or less, the engine is really not viable. However, many factors will come into play, including the shape of the reactor vessel and how much it tapers; whether the distribution of the neutron flux will be such that shielding thickness can taper along the vessel length; and smart layering of materials. Figure 20 shows a schematic of the PFRC with the rough locations of the shielding indicated.

Figure 20. PFRC Schematic with Conceptual Shielding

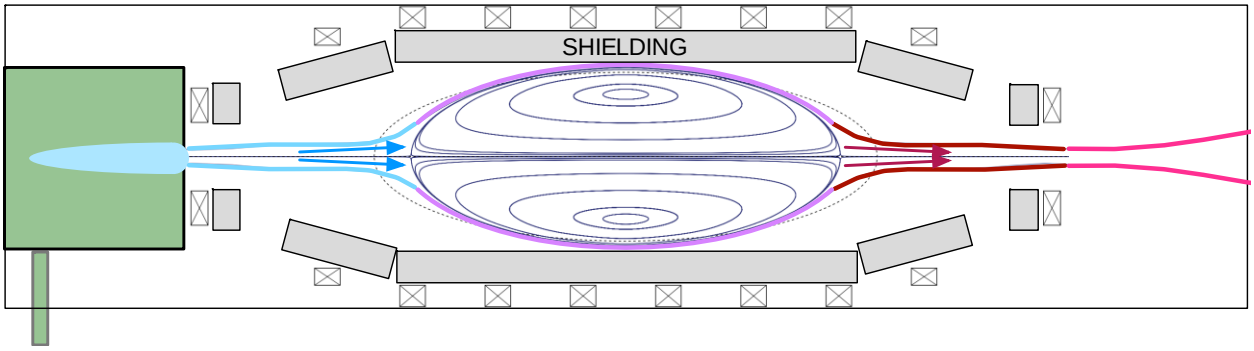

Our early analysis focused on B_4C as a shielding material due to the high neutron capture of the B10 isotope. However, this is only applicable once the neutrons have been thermalized. The

shielding needs to include a moderating material to thermalize the high-energy neutrons before they can be captured. This leads us to consider LiH, which has one-third the density of B_4C.

In the following sections, we will review the neutron scattering and capture properties of the candidate materials and compare LiH to B_4C. We will present fluence estimates for the PFRC. Finally, we will compare simple attenuation models to the results computed previously using the ATTILA radiation transport software.

3.2.1 Materials Properties

In general, low atomic number materials are needed to scatter the neutrons and thermalize them and then high absorptivity materials are needed to capture them. Elements with low atomic number used for scattering include hydrogen, carbon, and oxygen. These materials should have a high scattering cross-section with a low probability of capture. They must moderate or thermalize the fast incoming neutrons, from >1 MeV to <0.1 eV. Materials commonly used include polyethylene, paraffin, concrete, and water; for use in space, LiH**.**

Elements with high capture for thermal neutrons (n, α) include boron (10), cadmium, and gadolinium. Boron yields lower energy gamma radiation on capture than H, C, or O. Materials commonly used include borated polyethylene, B_4C, BN, boric acid in water, and boron-aluminum alloys. Finally, high atomic weight elements reduce the dose from gamma radiation (n,γ), for example lead and tungsten. The important considerations in designing the complete shielding are DPA (displacements per atom), heating, helium generation, and human exposure. Figure 21 shows the neutron cross-sections for hydrogen, lithium-6, and boron-10 from the National Nuclear Data Center.

The elastic cross-section is for scattering and thermalizing the neutrons, i.e. moderating them. The plot shows that hydrogen clearly has the highest elastic cross-section. The non-elastic cross-section includes capture. Hydrogen's elastic cross-section is even higher than lithium-6 and boron-10's capture sections at high energies.

Figure 21. Neutron cross-sections, *National Nuclear Data Center, www.nndc.bnl.gov/sigma*

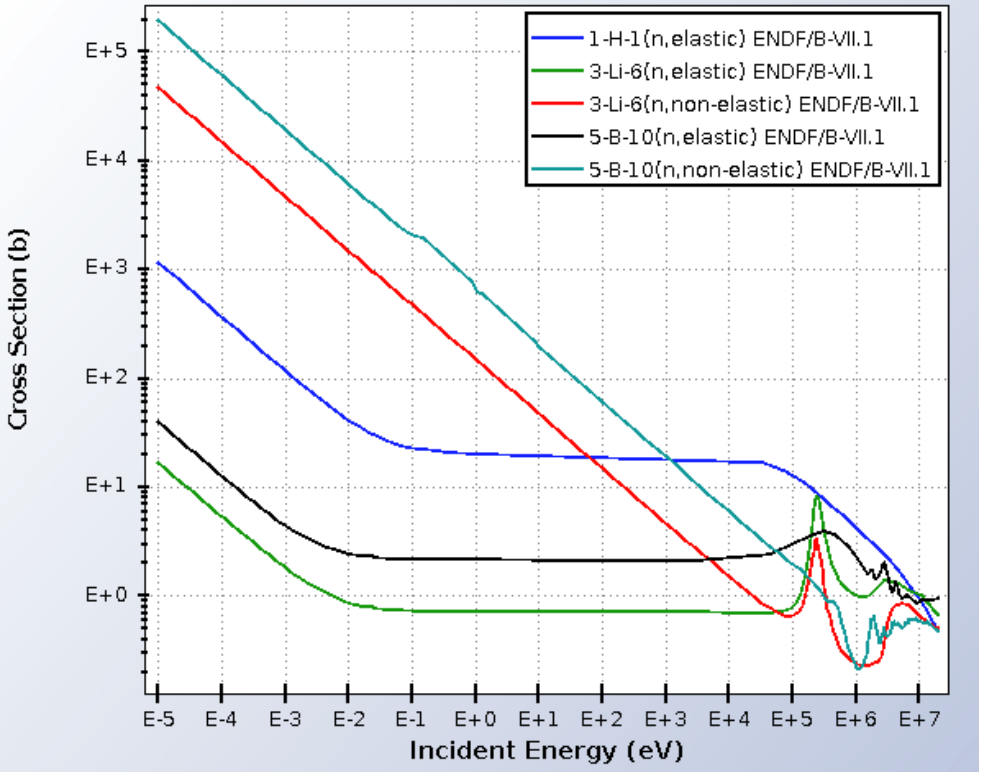

The microscopic cross-sections for our elements of interest are as follows:

- Hydrogen
  - @ < 0.1 eV ~ 80 barn (1e-24 cm^{-2})
    - Best scattering at all energies
  - @ 2.5 MeV ~ 2 barn
- Helium
  - @ < 0.1 eV ~ 1 barn
  - @ 2.5 MeV ~ 1-10 barn
- Boron
  - ^{10}B @ 0.025 eV ~ 3840 barn (capture)
    - Produces ^{7}Li & He
  - B @ 0.025 eV ~ 760 barn
  - ^{10}B @ 2.5 MeV ~ 2 barn
- Lithium
  - ^{6}Li @ 0.025 eV ~ 1000 barn (capture)
    - Produces He & tritium
  - Li @ < 0.1 eV ~ 70.5 barn (capture)
  - ^{6}Li @ 2.5 MeV ~ 1.5 to 3 barn
  - ^{7}Li: @ 2.5 MeV ~ 1-2 barns
- Carbon ~ 1-5 barn

- Xenon @ > 1 MeV ~ 8 barn

As indicated, B10 and Li6 have exceptionally high capture cross-sections for thermalized neutrons. The natural abundance of B10 in boron is 20%. The natural abundance of Li6 in lithium is only about 5%. Li6 has the undesirable side effect of producing tritium, so it may be preferable to limit Li6 in the moderating layers and use B10 as a capture material in final layers.

3.2.2 Attenuation Calculations

The mean free path of the neutron in the material is calculated as $\lambda = 1/N\sigma_t$, where N is the density in atoms/cm^3 and σ_t is the microscopic cross-section for the reaction of interest (elastic scattering or capture). The total attenuation is calculated as $I = \exp(-\Sigma t)$, where I is the transmitted intensity, Σ is the macroscopic cross-section computed from the sum of the microscopic cross-sections scaled by the element densities in the material.

Table 12 shows the results of the cross-section calculations for both fast and thermal neutrons. The mean free path for fast neutrons in LiH and B_4C is about the same, near 3.6 cm. This means that the thickness which attenuates 90% of the neutrons is about 8.5 cm for both materials.

Table 12. Mean Free Path and Attenuation for LiH and B_4C

	LiH	**^{6}LiH**	**B_4C**	**$^{10}B_4C$**
Density	0.78 g/cm^3		2.465 g/cm^3	
Atomic Density	5.9099e+22 /cm^3		B: 1.1408e+23 /cm^3 C: 2.8519e+22 /cm^3	
Fast Micro Cross-Section (b)	H: 2.8 Li: 1.9		B: 2 C: 1.5	
Fast Macro Cross-Section (cm^{-2})	0.271		0.278	
Fast Mean Free Path (cm)	3.60		3.69	
50% Attenuation Thickness	2.5 cm		2.56 cm	
90% Attenuation Thickness	8.3 cm		8.5 cm	
Thermal Cross-Section (b)	70.5	1000	760	3840
Thermal Mean Free Path (cm)	0.24	0.017	0.011	0.002

As Table 12 shows, once the neutrons are thermalized, they are captured in only a thin layer of either LiH or B_4C. The exact thickness of the capture layer is determined via analysis of the DPA, heating, helium generation, etc. and the lifetime requirements on the shielding. This requires high fidelity neutronics tools.

3.2.3 PFRC Neutron Fluence

The neutron fluence of the PFRC is reduced to minimal levels in the following ways:

1. Small reactor size gives favorable surface area to volume ratio

2. Ratio of 3He to D is above 1, trading some power density for lower fluence
3. Rapid exhaust of tritium eliminating D-T reactions
4. Beam-like 3He and D distributions may allow D to be half the temperature of 3He

Given effects 1, 2 and 3, we would expect the neutron power from D-D reactions to be about 0.5-1% of the fusion power. If we also consider the possibility of effect 4, this could be as little as 0.2% of the fusion power. For a fusion power of 5 MW, this is the difference between 3.2 kW/m^2 of neutron wall loading and 6.4 kW/m^2. Figure 22 shows a contour plot of the neutron power in the PFRC as a function of total fusion power, assuming there are no D-T reactions. The horizontal axis shows the fuel ratio and the vertical axis the plasma temperature. Our target region is the upper right corner, where the neutron power ranges from 0.3 to 0.5%. In this example, the electron temperature was 30 keV and the D and 3He are at equal temperatures (no effect 4).

The lifetime fluence parameter used for ITER's superconductors is 1e22 n/m^2. The expected lifetime fluence for DEMO is 3-5 times higher and for a commercial tokamak reactor is expected to be higher still. Therefore, we can use as a design parameter for the magnets a lifetime fluence of 5e22 n/m^2. See Figure 5 and Figure 6 which show irradiation effects on high-temperature superconducting tapes.

Figure 22. Neutron Power in D-T Suppressed PFRC. D and 3He at equal temperature.

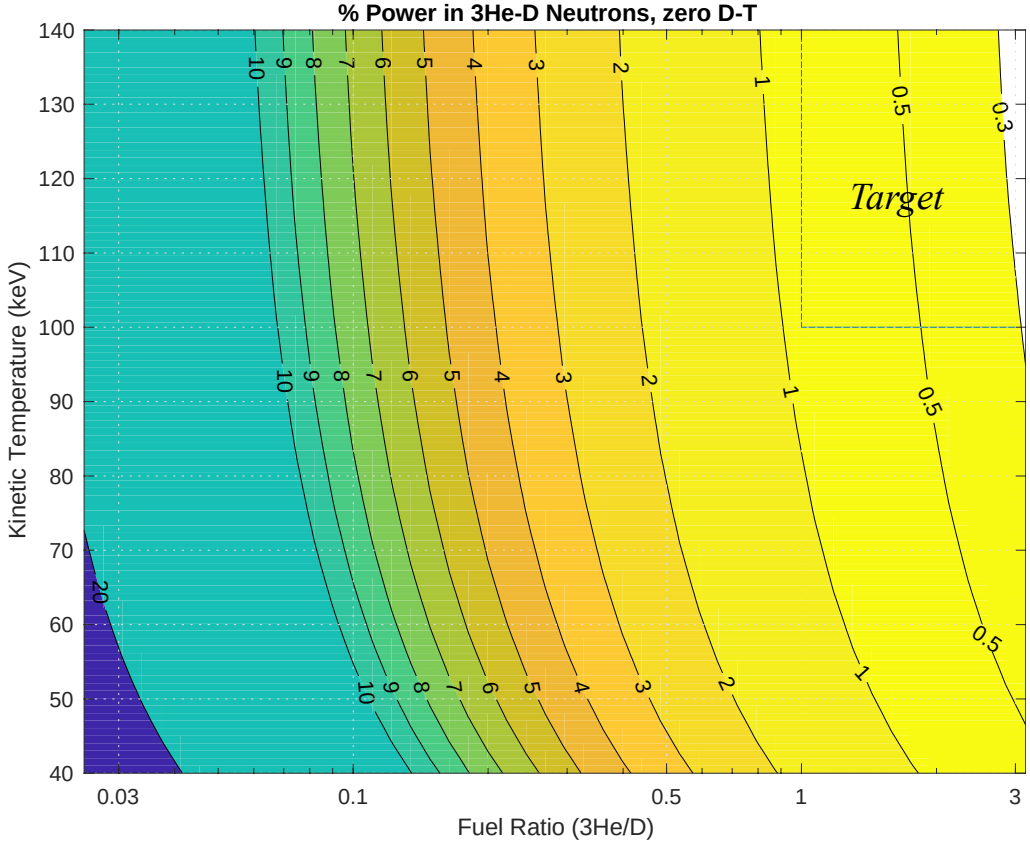

Table 13 shows a summary of calculations of neutron wall loading in the PFRC. The plasma parameters are adjusted to produce the given fusion density in MW per m of reactor length. The nominal 3He temperatures are 100 keV, with an electron temperature of 50 keV and an electron density of 4.3e20 m^{-3}. The wall radius is at 0.5 m and the plasma radius is 25-30 cm. The fuel ratio is given in the first column, from 1:1 for the first case to 3:1 for the last four cases. For the 0.2% case, the deuterium temperature is reduced to 70 keV. For the 0.15% case, the 3He temperature is also raised to 140 keV. In the final 0.1% case, we apply an additional 50% reduction in D-D reactions such as may occur given beam-like distributions.

Table 13. Fluence Calculations for PFRC

Fusion Power	Neutron Power	Wall Load	Flux	1-year Fluence
2.0 MW/m @ 1:1	1%	12.34 kW/m^2	3.1e16 $n/m^2/s$	9.9e23 m^{-2}
1.5 MW/m @ 2:1	0.5%	4.44 kW/m^2	1.1e16 $n/m^2/s$	3.6e23 m^{-2}
1.0 MW/m @ 3:1	0.3%	3.06 kW/m^2	7.8e15 $n/m^2/s$	2.5e23 m^{-2}
1.0 MW/m @ 3:1	0.2%	2.16 kW/m^2	5.5e15 $n/m^2/s$	1.7e23 m^{-2}
1.0 MW/m @ 3:1	0.15%	1.38 kW/m^2	3.5e15 $n/m^2/s$	1.1e23 m^{-2}
1.0 MW/m @ 3:1	0.1%	1.08 kW/m^2	2.8e15 $n/m^2/s$	8.7e22 m^{-2}

Note the flux and fluence columns. This is the 1-year fluence that the magnets would see if there were no shielding. In the lowest possible neutron flux case, the 1-year fluence is in the range of the superconductor lifetime limit. Shielding reducing this fluence to 10% should be roughly equivalent to a 10-year lifetime.

Figure 23. Shielding Thickness for 5e22 n/m^2 Design Fluence

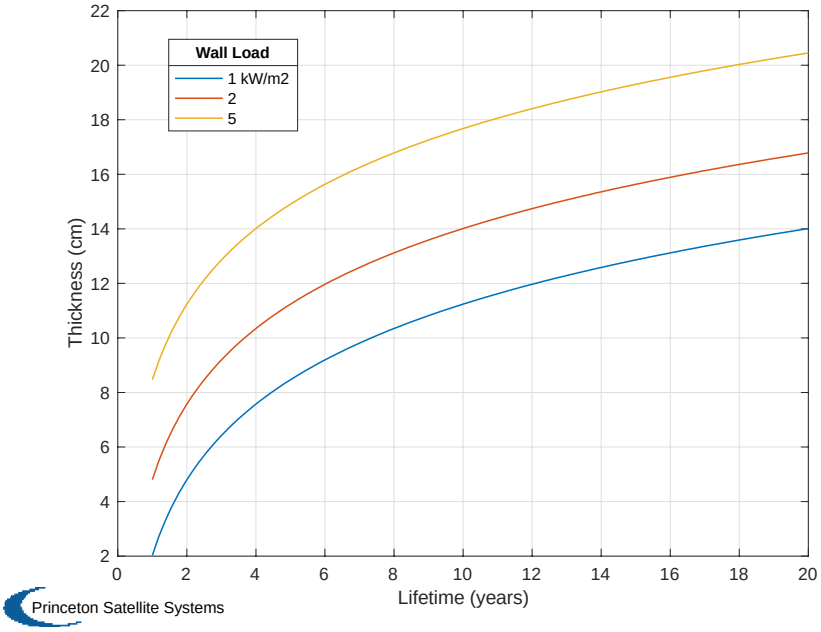

Figure 23 shows the attenuation results from the previous section coupled with these wall loads and fluences, to show an estimate of shielding thickness needed as a function of desired engine lifetime. This applies a 5e22 n/m^2 design fluence limit on the superconductors.

These results suggest that one design possibility for a "sprint" DFD engine, for example for rapid transit to Mars, is to use no magnet shielding whatsoever. Such an engine may have an operational lifetime of 1 year, which would allow several Mars roundtrips.

3.2.4 Comparison to ATTILA Results

These results are consistent with early 2D calculations performed using the ATTILA package for radiation transport simulations. Several PPPL interns performed calculations for only B_4C in 2014. [16] The wall loading assumption was 6.4 kW/m^2, which we have shown above to be pessimistic. The ATTILA results found that both Helium production and DPA at this loading will not contribute to structural deterioration.

Figure 24 shows the ATTILA grid and an example output from one run. Figure 25 shows the results of a set of runs as a function of shielding thickness, for Boron-11, natural boron, and Boron-10.

Figure 24. ATTILA Grid and Example Output

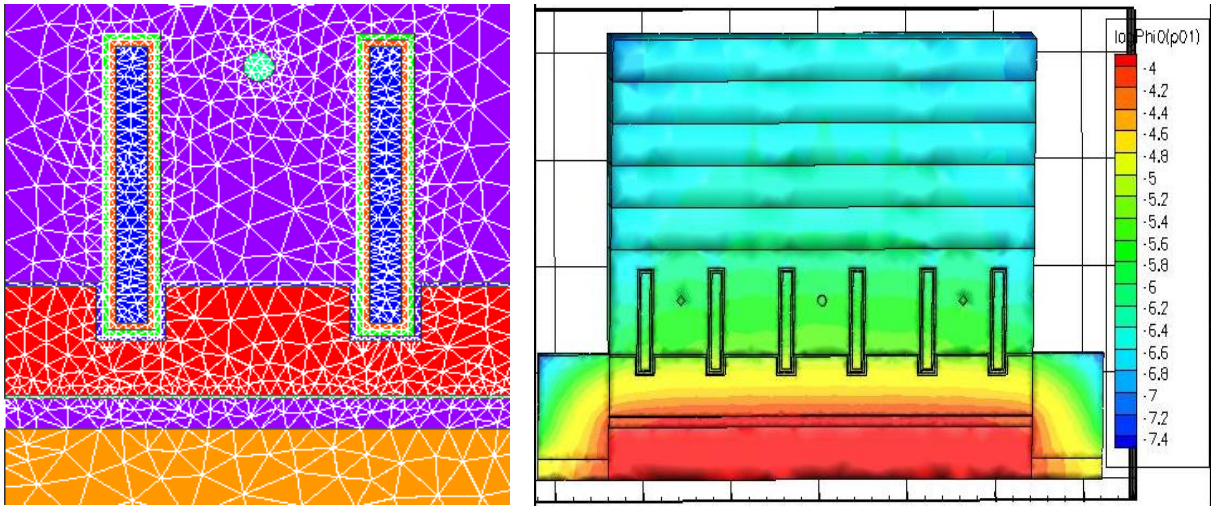

Figure 25. ATTILA 30 Year Fluence vs. Shielding Thickness for 6 kW/m^2 Neutron Power

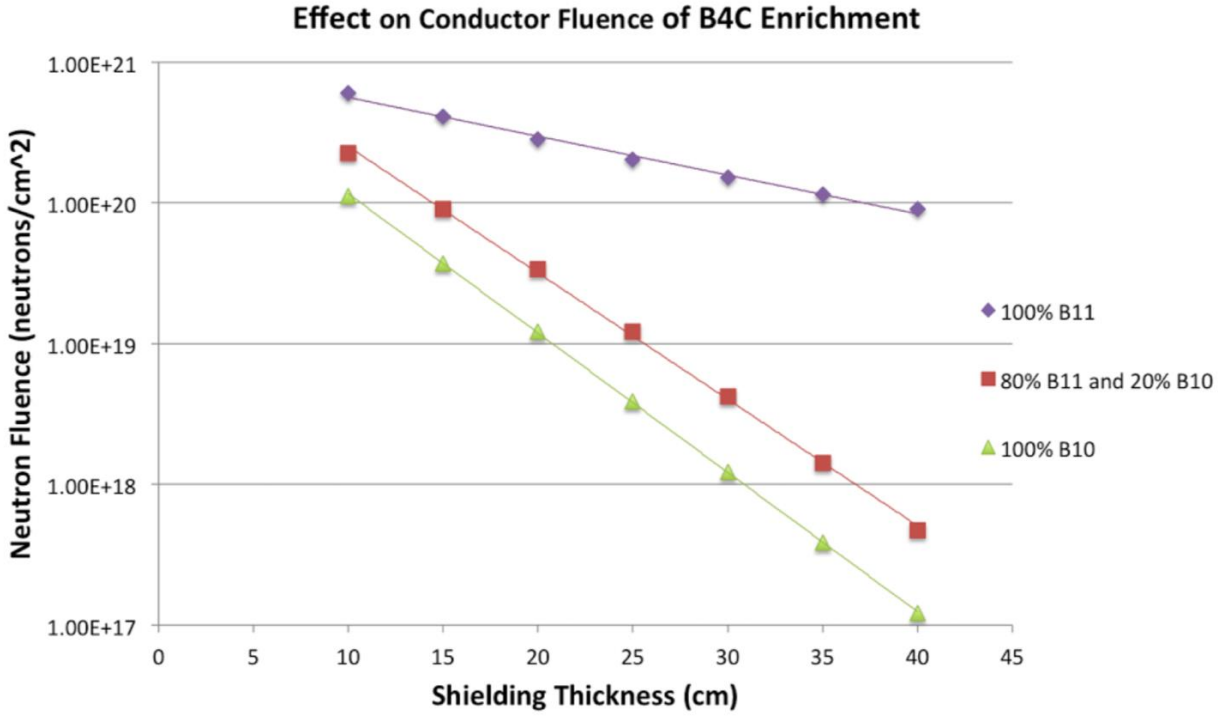

Extracting a few points from the B10 dataset, we see that every additional 10 cm in thickness gives about one order of magnitude improvement in the total fluence on the superconductors:

- 30 cm thickness
  - 30-year fluence 1e22 n/m^2
- 20 cm thickness
  - 30-year fluence 1e23 n/m^2
- 10 cm thickness
  - 30-year fluence 1e24 n/m^2

These results are consistent with a macroscopic cross section of about 0.25-0.27 cm^{-2}, which is precisely what we calculated using simple microscopic cross sections in Table 12. The input fluence is roughly 1.5e21 n/cm^2. In Table 14 we compare the numbers directly using the same units as Table 13, for a one-year fluence. 10 cm of shielding provides about a 93% attenuation in neutron flux.

Table 14. One-Year Fluence from ATTILA Calculations and Simple Attenuation Model

	ATTILA	Attenuation
Thickness	6 kW/m^2	1 kW/m^2
0 cm	5e23 m^{-2}	8.3e22 m^{-2}
10 cm	3.3e22 m^{-2}	5.5e21 m^{-2}
20 cm	3.3e21 m^{-2}	5.5e20 m^{-2}

30 cm	3.3e20 m^{-2}	5.5e19 m^{-2}

3.2.5 Shielding Design

Figure 26 shows an axial cross-section view of the shielding concept. The red central area indicates the fusing plasma region, and the green band the cooler scrape-off-layer. The blue channels are for the thermal conversion system working fluid. The working fluid will contribute to neutron moderation. Additional shielding will be required between the channels and the magnets, as shown. The x-ray absorption layers are not shown.

Figure 26. Shielding Concept with Coolant Channels, Axial View

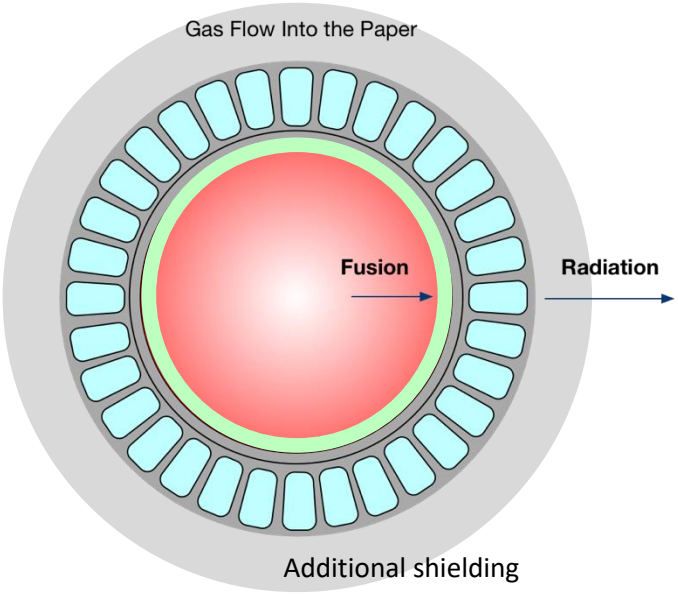

Figure 27 shows a transverse cross-section showing the magnet windings in their cryostat beyond the shielding. The flow direction of the working fluid is shown. The x-ray absorber is shown conceptually near the inner wall of the fluid channels. The first wall will also contribute to neutron moderation.

At a high level, if we want the specific power of the engine to be about 1 kW/kg, the shielding must be in the 100's of kg for a 1 MW reactor. Consider a very simple calculation of 10 cm of shielding. The assumptions are: a 32 cm vessel inner radius, cylindrical shape, and 1 m length. We also require a layer of tungsten to absorb the x-rays from synchrotron radiation; assume a 0.5 mm layer at the same 0.32 m radius:

- B_4C: 585.84 kg
- LiH: 181.33 kg
- W: 19.367 kg.

Figure 27. Shielding Concept, Transverse Cross-Section View

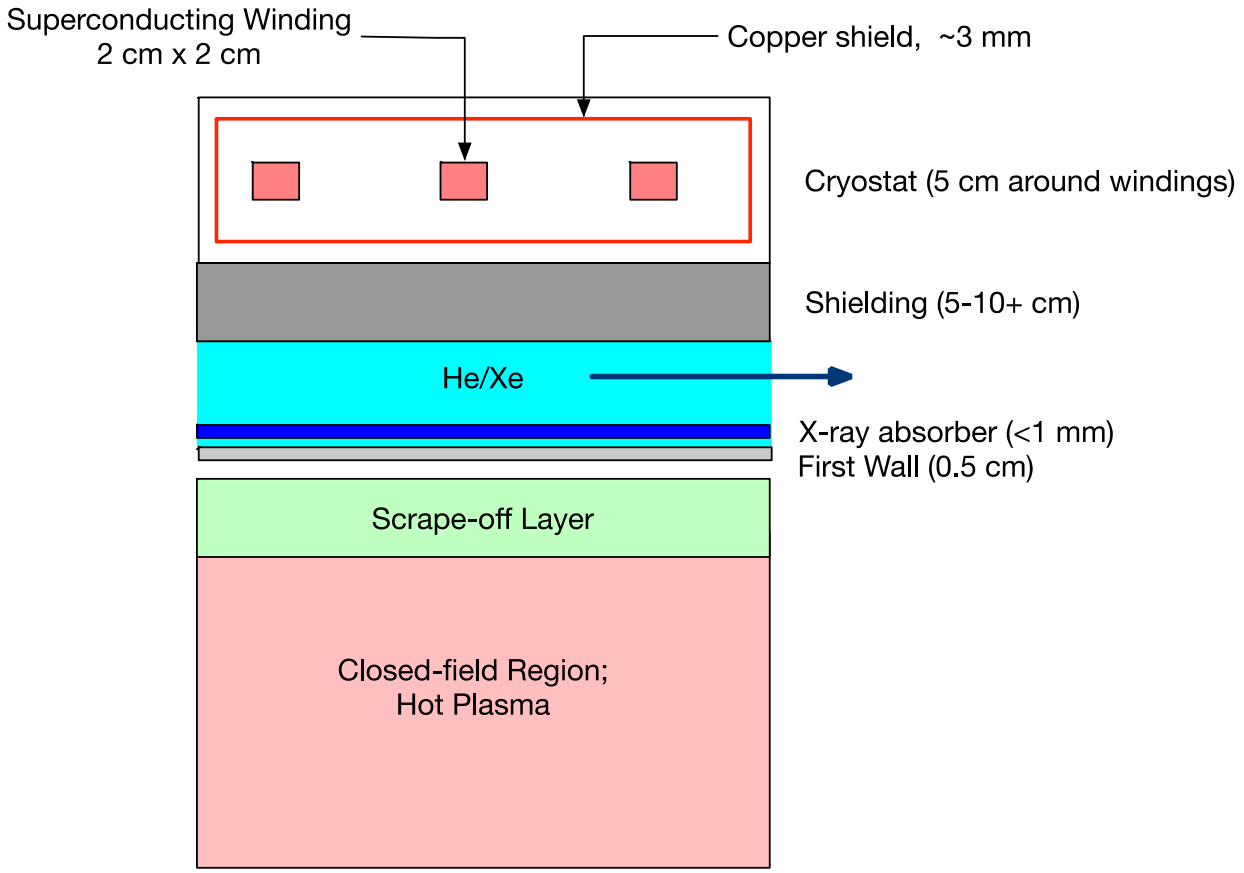

Our results show that we want the shield to be mostly LiH for neutron moderation, as is typical in other fusion propulsion shield designs. Only a small thickness of ^{6}LiH or $^{10}B_4C$ is needed for neutron capture once the neutrons are thermalized.

In future work, we would like to run ATTILA calculations with a more modest input fluence and a combination of materials including LiH moderator and the working fluid. We hope to reduce the final shielding layer to as few cm as possible once all the various layers are taken into account. In addition, we need to compute shielding needs along the length of the engine, since a fully cylindrical shield will be impractical. We anticipate that a higher thickness may be required near the midplane and a reduced thickness approaching and beyond the plasma x-point.

3.3 Synchrotron Modeling

From the Phase II Proposal:

> Existing synchrotron models are based on tokamak topologies. Simple models indicate a wide range of potential synchrotron losses, and to more fully quantify our configuration requires expert analysis. Staff at PPPL will develop a synchrotron model for our specific topology;

this is a complex task because the magnetic field strength in an FRC varies strongly with radius. At the simplest level, the radiated power increases with the square of the magnetic field and linearly with density and temperature, B^2nT; the temperature and density in an FRC are highest where the field is lowest, requiring detailed plasma parameter profiles. Moreover, radiation from the FRC core is absorbed in its higher field region, hence radiation losses depend on surface area more than volume. An additional complication is the reflectivity of the FRC walls, which reduces the losses and will influence the scrape-off-layer. A detailed model is needed.

We have produced 0D, 1D, and 2D models of synchrotron emission from the DFD, each with their own assumptions. At the broadest level, we have established that the reflectivity of the first wall to microwave (100s of GHz) radiation is essential to mitigating synchrotron losses from the plasma. We also find that sufficient reflectivity is well within the range of standard materials.

Synchrotron radiation is the name given to cyclotron radiation from high-energy electrons. All electrons moving through a magnetic field all emit this radiation. To escape from a plasma, the synchrotron radiation must leave in the form of electromagnetic waves in the plasma, which complicates calculations of generation, transmission, and re-absorption. Electromagnetic waves may be absorbed, refracted, or reflected within a plasma. The frequency of the wave is the fundamental cyclotron frequency and its harmonics, $\omega_{ce} = eB/m$.

3.3.1 0D Synchrotron Model

The 0D model simply evaluates the cyclotron radiation density equation in the NRL formulary at the assumed peak density, magnetic field, and temperature:

$$P_c = [6.21 \times 10^{-28}\mathrm{W/cm^3}] \times \left(\frac{\mathrm{B}}{\mathrm{Gauss}}\right)^2 (n_e \times \mathrm{cc}) \left(\frac{T_e}{\mathrm{eV}}\right)$$

This model can be considered a worst-case scenario, and indeed predicts that cyclotron/synchrotron emission is the dominant mechanism for energy loss from the plasma.

Additional corrections to the 0D model include:

- The effect of a quadratic n_e with radius introduces a factor of 0.4 when volume-averaged
- The assumption that only 10% of the volume is able to radiation without re-absorption introduces a factor of 0.1

In order to achieve still more accurate results, the model must resolve the radial dimension, which we do in the 1D model described next.

3.3.2 1D Synchrotron Model

Radially-resolved calculations show that the proportion of power lost to synchrotron in the 0D model with 10% emission volume is correct to within about 10%. For a 25-cm-radius, the

elongation $\kappa = 6$, $\langle\beta\rangle = 0.8$, and $B_{max} \sim 5$ T, FRC reactor producing 10 MW_{th} fusion power, that corresponds to about 5 MW of synchrotron power. The main difference from the 0D model was to eliminate the 10% volume assumption and to calculate directly the radial profile of the synchrotron power using a plausibly broad, quadratic T_e profile, a rigid-rotor-current hyperbolic tangent (tanh) B profile, and an n_e profile found self-consistently assuming a plasma β of 0.8. The volume is assumed to be ellipsoidal. The peak B, n_e and T_e were taken from a PFRC-4 0D fusion power model. No re-absorption in the plasma is assumed. No wall reflection is assumed. See Figure 28. Detailed studies of parametric dependence were not undertaken with the 0D or 1D models; we used the most accurate 2D model for this purpose.

Figure 28 Synchrotron 1D Model with Parabolic T_e profile

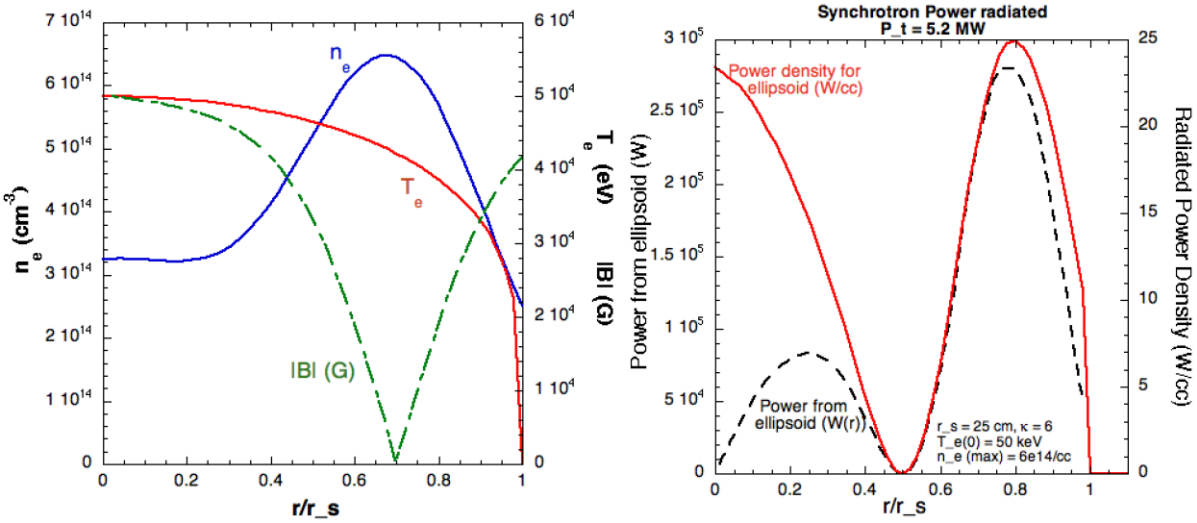

3.3.3 2D Synchrotron Model

The 2D model uses profiles of B and plasma pressure determined self-consistently by the Grad-Shafranov solver or by the analytic Hill's Vortex equilibrium, resolved in *r* and *z*. Another important distinction is that electron temperature is found self-consistently by equilibration between heating via ion collisions and the various loss mechanisms. Ion and electron temperatures are constant over the FRC volume. Figure 29 shows the Hill's Vortex magnetic field used in this model. The synchrotron output for a specific run-case is visualized in Figure 30.

This model does not consider the complex phenomenon of transmission of electromagnetic waves through an over-dense plasma. This makes it a conservative model, as electromagnetic radiation must be transmitted through the magnetized plasma in the form of X- or O-mode radiation, both of which are damped in the so-called over-dense parameter regime, where $\frac{\omega_{ce}}{\omega_{pe}} < 1$. In effect, synchrotron emission from dense plasma in a weak magnetic field is damped. The volume in which this is true for the 1st and 2nd harmonic of the cyclotron frequency is depicted by the dotted lines in Figure 31. The volume between the dotted lines in this figure is over-dense, which likely suppresses a portion of the power emitted within.

Figure 29. Magnetic Field Profile of an Elongated Hill's Vortex FRC (E. Evans)

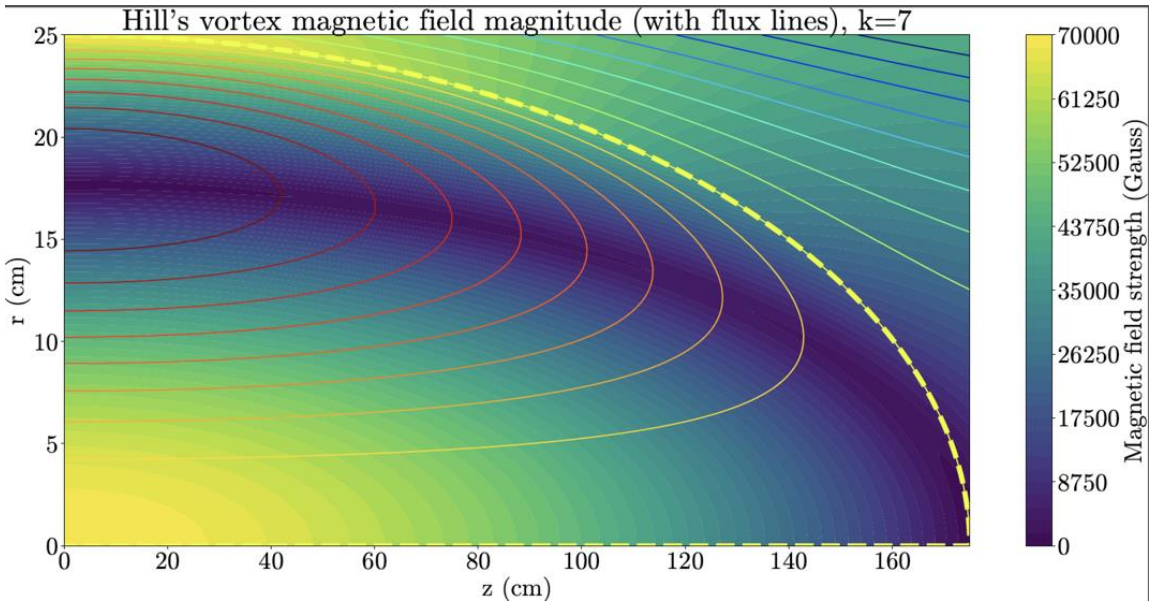

Figure 30. 3D Plot of Synchrotron Emission from the 2D Model (E. Evans)

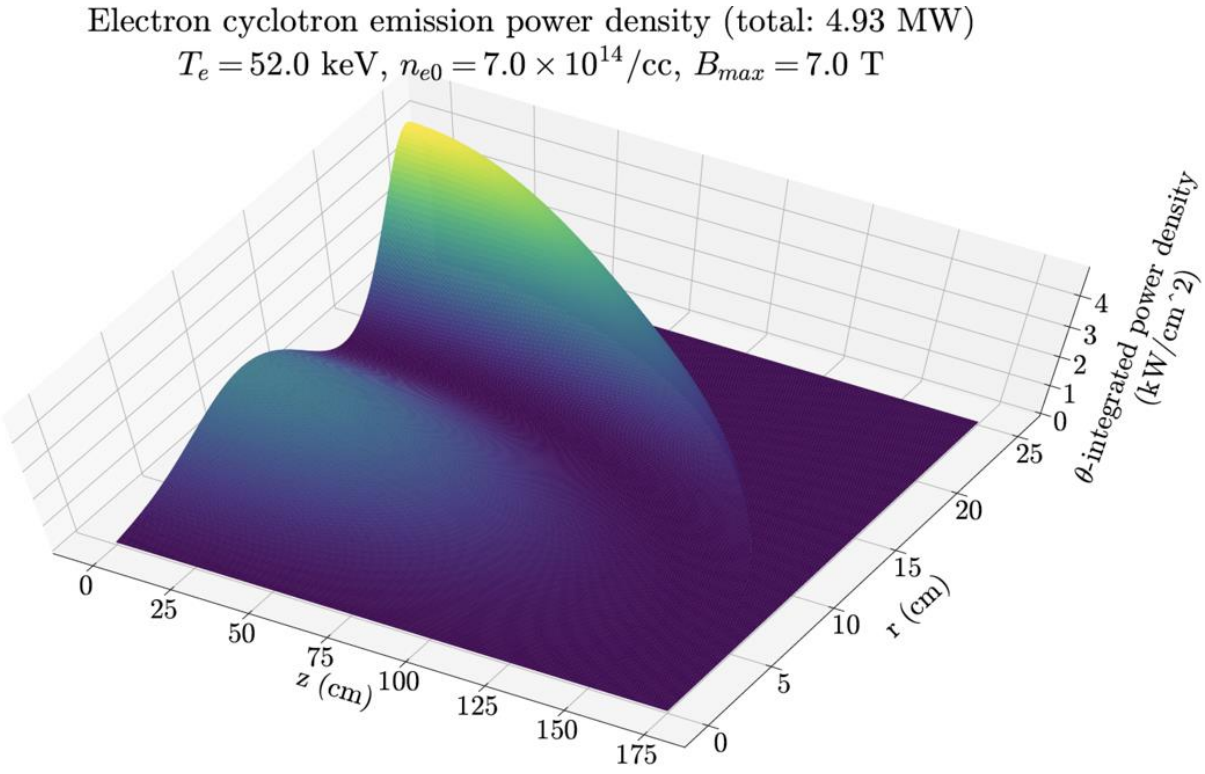

Figure 31. 2D profile of synchrotron emission of Hill's Vortex FRC with plausible B, n, T.

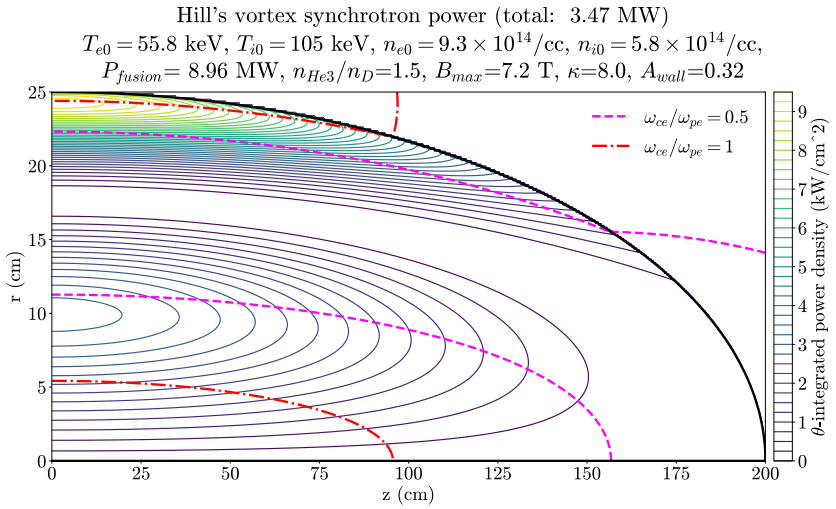

This model does not *consistently* model reflection from a conductive reflector and re-absorption by the plasma. The effects of reflection are included by a factor which decreases the Synchrotron losses according to the model: $P_S \rightarrow \sqrt{1-R} \times P_s$, where R is the wall reflectivity [17], R~0.999 for copper at 100 GHz. This model accounts for multiple re-reflections between the plasma and wall, with absorption occurring at each reflection.

Because of the self-consistent T_e procedure described above, the net overall synchrotron power was not reduced by this factor $\sqrt{1-R}$. This is because, as a consequence of the lower synchrotron losses, the ion-heated electrons equilibrate at a higher temperature, increasing the synchrotron emission. Increasing R does decrease net P_s, but not by as significant a factor as is given above.

Furthermore, because T_e increases, Bremsstrahlung power loss, in the form of X-rays emitted by the plasma increases. The net effect is complex, and is shown in Figure 32, Figure 34, Figure 35, and Figure 33. These figures show the competing effects of lower synchrotron losses, higher temperatures, and higher Bremsstrahlung losses. Figure 32 shows the synchrotron power, which decreases to 0 as the wall reflectivity approaches 1, as expected. Figure 33 shows the increase in Bremsstrahlung with reflectivity, due to increasing temperature. Even at the highest electron temperatures over 70 keV, Bremsstrahlung is not more than 25% of the fusion power. In Figure 34, as wall reflectivity increases, the electron temperature increases as synchrotron losses decrease. At the same time, the peak electron density decreases. The power available to the fusion products, i.e. for thrust in a DFD, increases, Figure 35.

Figure 32. Synchrotron power decreases as wall reflectivity increases, but not as quickly as a constant-temperature model would predict.

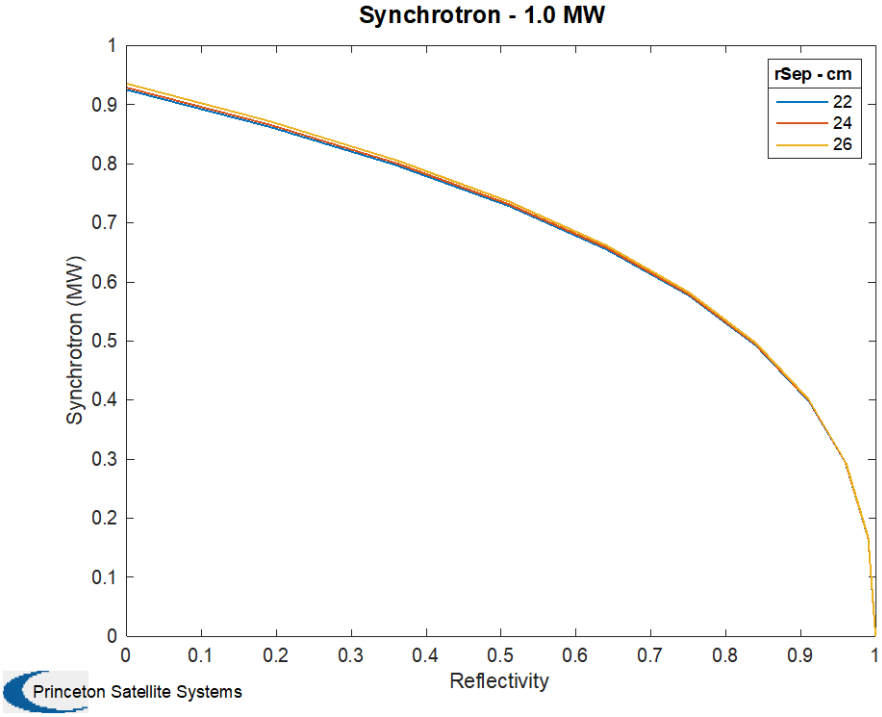

Figure 33. Bremsstrahlung power increases as wall reflectivity increases due to increased electron temperature.

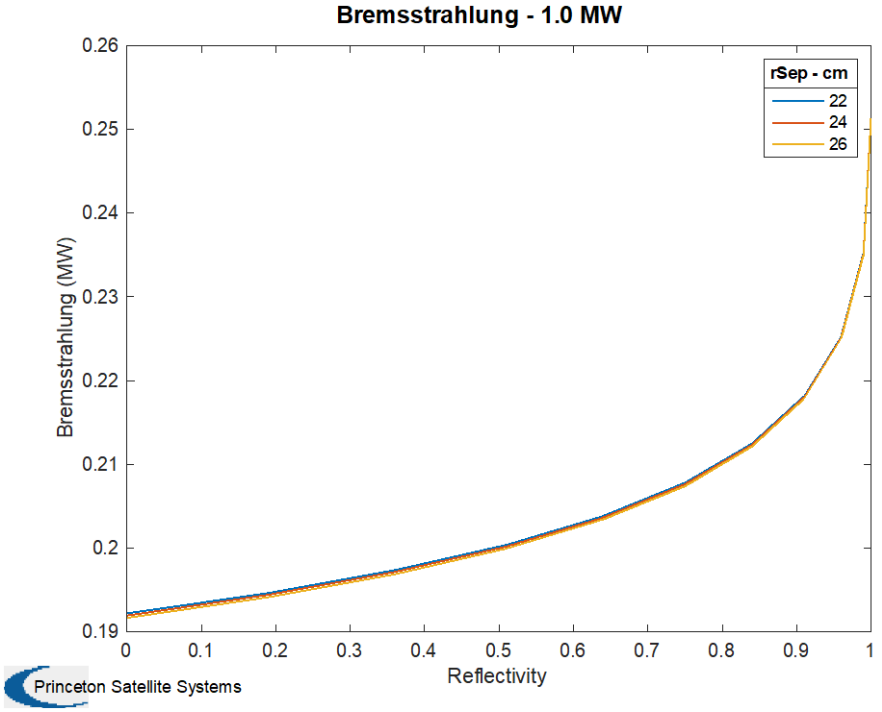

Figure 34. Electron temperature and density as a function of wall reflectivity.

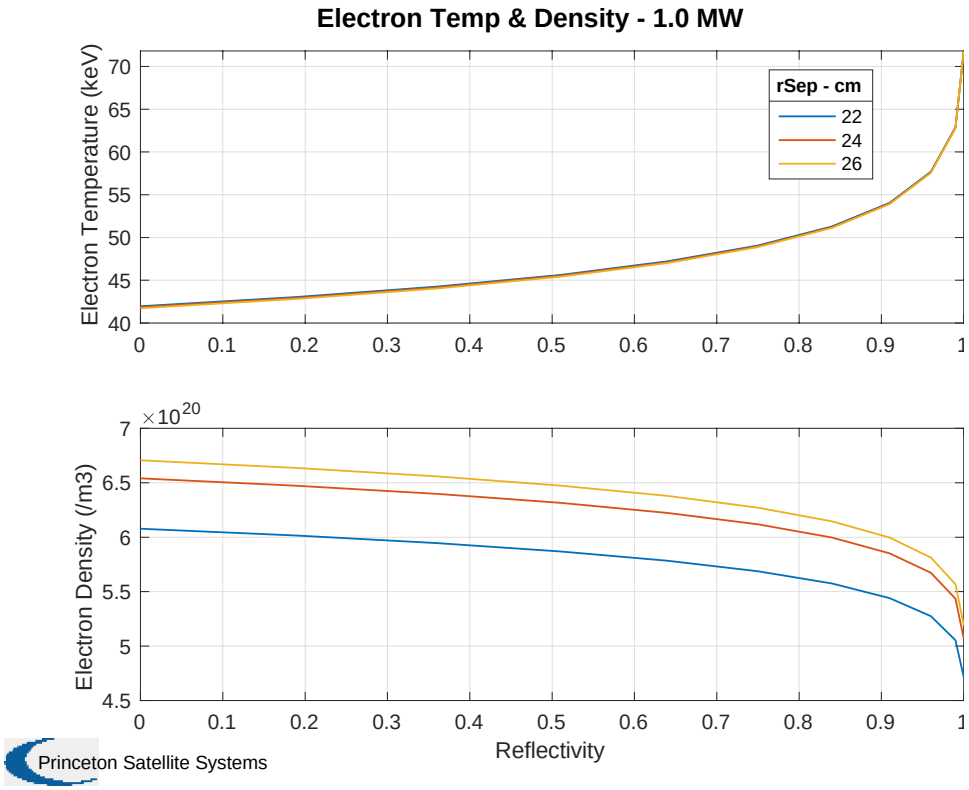

Figure 35. Power to Fusion Products

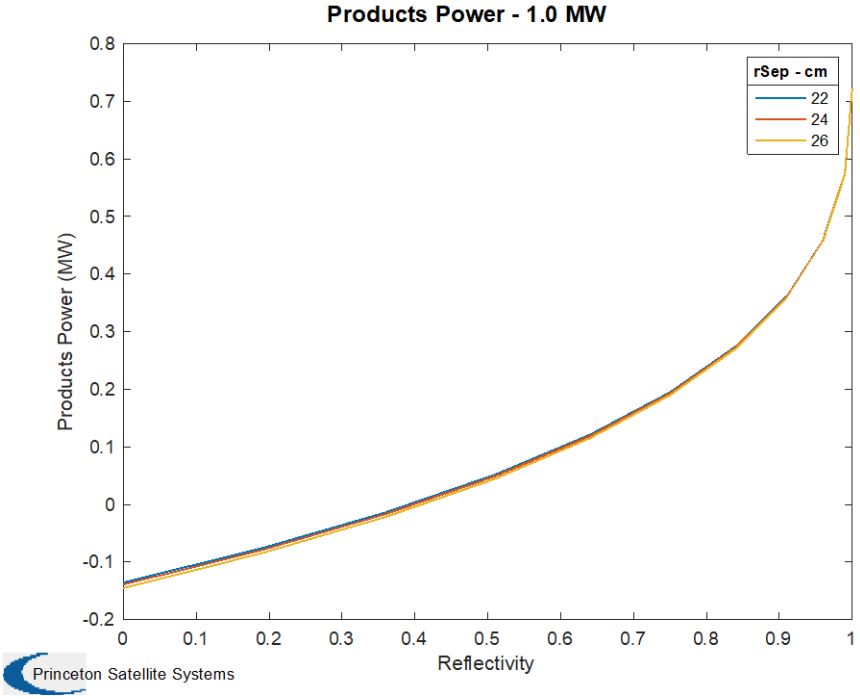

It should be noted that synchrotron losses and Bremsstrahlung losses are lost from the plasma, but not lost from the system. They are deposited in the vessel as heat and converted to electricity by the thermal conversion system. The tradeoff in R is the ratio of synchrotron/Bremsstrahlung power to fusion product power, the former of which becomes electrical power and the latter of which becomes thrust power.

The figures above are for a 1 MW DFD with a fuel ratio of 2.5 3He:1 D. We find that higher power DFDs are best created by simply changing the elongation κ of the FRC; these follow the same trends.

We can compare the 2D output to our 0D model. We use the computed electron temperature, density, and elongation from the 2D model, with the same assumed ion temperature (105 keV). Using the peak density from the 2D model overestimates the fusion power by about a factor of 4, which is corrected by using an average density that is half of the peak value. Figure 36 shows the resulting total power, Bremsstrahlung power, and synchrotron power. The total power is very close as is the bremsstrahlung power, with the 0D model slightly overestimating bremsstrahlung at the highest reflectivities. The 0D synchrotron power is plotted at 10% of the total volume using the NRL relation. As can be seen, while the 2D model shows a dramatic decrease in synchrotron with increasing reflectivity, the 0D model predicts a dramatic decrease as a result of the increasing electron temperature and volume needed to maintain the target power of 1 MW.

Figure 36. Total Power, Bremsstrahlung and Synchrotron for 0D and 2D Models

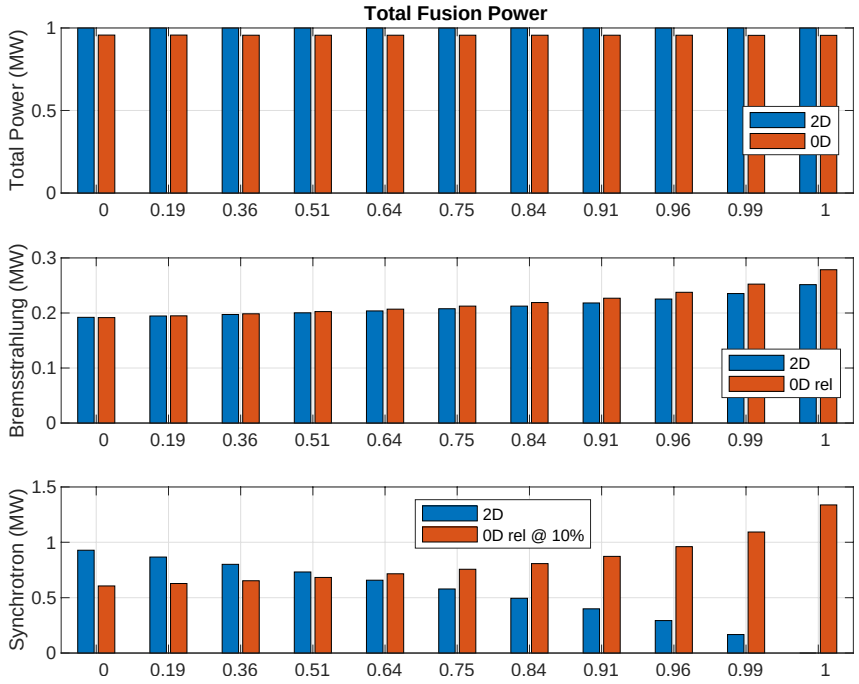

This allows us to directly compare a 10% volume fraction of the 0D model to the 2D result, in Figure 37. We have numerically computed the point where the two models intersect, marked

with an asterisk. From this plot, we see that the models are equal when the reflectivity is about 57%.

Figure 37. Comparison of 0D (10%) and 2D Synchrotron Models for 1 MW Reactor

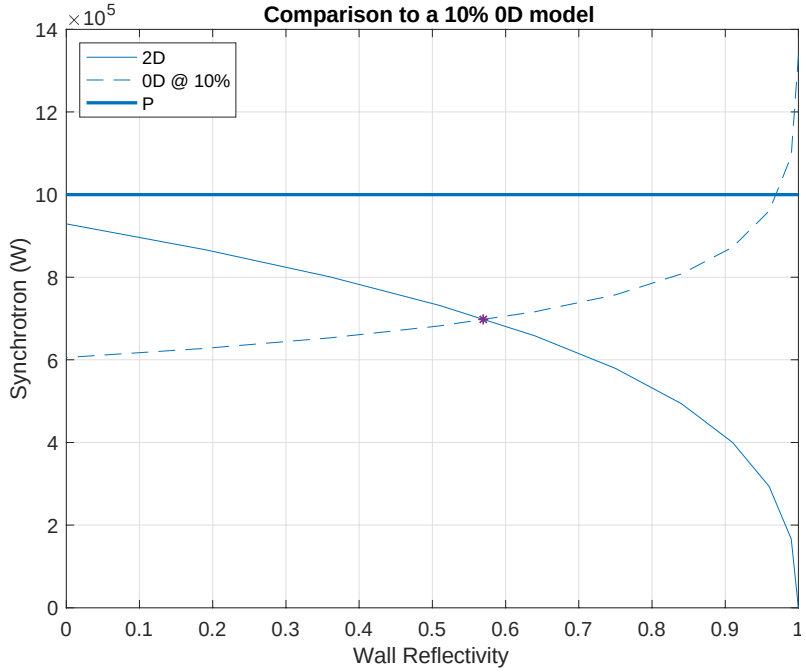

We can use this point to produce a scaling of the 0D 10% model, using the ratio of the reflectivity factor $\sqrt{1-r}$ to the found value. This gives us a simple analytical synchrotron model that is a function of wall reflectivity,

$$P_{sync} = 0.1B^2 n_e T_e \frac{\sqrt{1-r}}{\sqrt{1-\tilde{r}}}$$

Where we have neglected the units correction terms for clarity.

Based on the results of this model, if we want to maximize the power to the fusion products such as to maximize thrust, we want a very high wall reflectivity. If the wall can be 95 to 98% reflective, synchrotron losses can be reduced to 25 to 31% of the total fusion power. This is well within the range of standard materials, as copper has a wall reflectivity at 100 GHz of 0.999. [18] Alternatively, more synchrotron can be pushed to the wall deliberately with a lower reflectivity, which may be preferable for terrestrial power production.

Figure 38. 0D 10% Model Fit Using r=0.57 Scale Factor

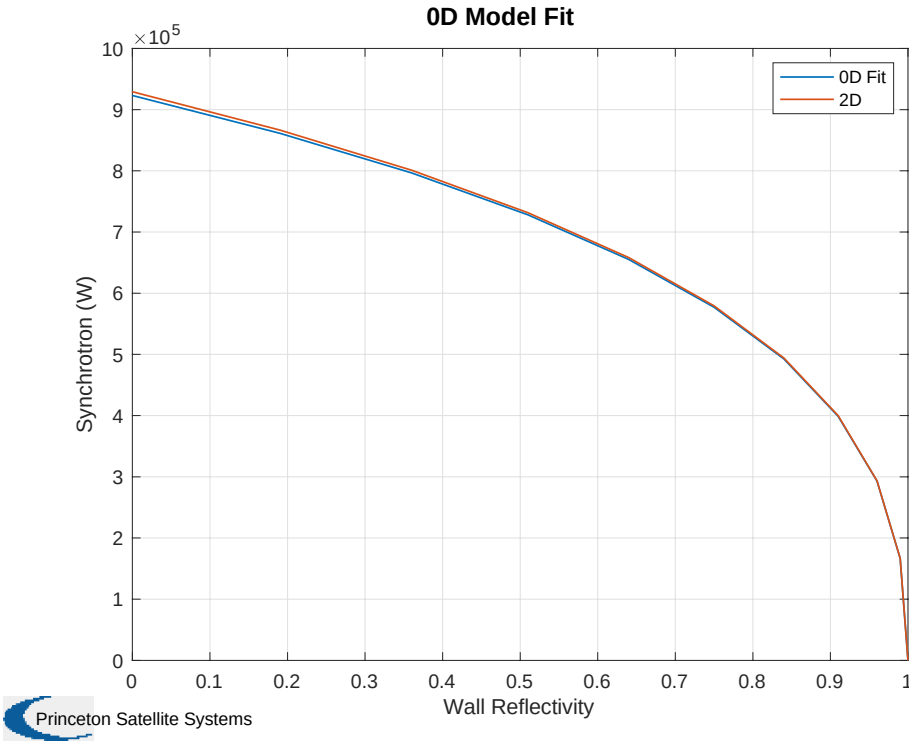

For DFD, we now assume an operating reflectivity of $R = 0.95$ for our point reactor model. At this point, for a 1 MW reactor, electron temperature $T_e = 57.4$ eV, synchrotron power $P_s = 0.307$ MW, Bremsstrahlung power $P_b = 0.22$ MW, and power into the fusion products (which produce thrust) $P_p = 0.44$ MW. These fractions are the same for different power DFDs. Table 15 gives a summary of the reactor parameters for this point.

Table 15. 1 MW Point Reactor, 95% Synchrotron Reflected

Parameter	Value
T_e	57.4 keV
T_i	105 keV
Peak n_e	5.69e14 /cc
Average n_e	2.85e14 /cc
3He:D	2.5
r_s	24 cm
κ	5.4
Peak B	5.5 T
Fusion Power	1 MW
Bremsstrahlung	0.225 MW
r_{Wall}	0.95
Synchrotron	0.307 MW

The microwave-reflecting portion of the wall will be a thin layer of metal such as copper (skin depth 200 nm). The conductive layer must not completely encompass the plasma, as this would block the RMF. Non-conductive breaks must run along the axial direction, of less than a quarter-wavelength (1 mm) width.

3.4 Thrust Augmentation Experiments

From the Phase II Proposal:

> The conversion of the PFRC reactor to the Direct Fusion Drive is dependent on the thrust augmentation system. Theoretically, this can provide a range of thrust and specific impulse for a single engine configuration, by varying the gas flow rate and possibly the mechanical aperture size. This flowing of additional gas around the FRC region has been analyzed using 1D and 2D fluid codes for a single scrape-off-layer geometry. The PFRC-2 experiment has recently been equipped with a pulsed gas valve which can increase the pressure in the gas box by a factor of 10 in a span of two to three milliseconds. However, PPPL does not have the manpower or funds to utilize it. We can take advantage of this setup to explore the dynamics of the scrape-off-layer and help validate the results of the software codes. A long pulse length of the FRC is required for these gas flow studies, perhaps 50 ms. Fortunately, the PFRC-2 is achieving pulses of 300 ms or more. This will be sufficient to pulse the gas and measure the results during a single FRC pulse. PPPL staff will gather the data from the PFRC-2 and PSS staff will assist in analyzing it.

We have simulated the SOL of the DFD under thrust augmentation conditions using the PFRC-2 experiment. The configuration is shown in Figure 39. Gas is puffed into the Source End Cell (SEC) using a supersonic valve which was added to machine specifically for this project. (Now there are two on the machine, and gas can be puffed into the SEC or the Center Cell (CC) without a vacuum opening.) Two SEC puffing experiments were conducted:

1. The RMF plasma of the PFRC-2, a hot, dense FRC plasma which is contained in the CC and around which cooler plasma flows. This simulates the full DFD system, both the core and the SOL.
2. The seed plasma of the PFRC-2, a cold, tenuous plasma which flows through the SEC, CC, and FEC. This simulates the SOL only, without the fusion core.

The process of thrust augmentation is primarily concerned with the flow of plasma along the length of the DFD. In the DFD, this plasma flows into space. In the PFRC-2, this plasma flows into the FEC, hits a tantalum paddle, and recombines into gas. Because of this, one of the measurements taken during the experiments was the time-resolved pressure in all three chambers of the PFRC-2. The measurements were made using Baratron-brand capacitive manometers in each chamber. With these measurements, we were able to infer the flow of plasma between the chambers.

Because the plasma flows as a plasma, not a gas, we also measured an electrostatic quantity: The floating potential of the tantalum paddle in the FEC. Due to an effect called the Langmuir sheath, this potential is proportional to the temperature of the plasma with the following relation:

$$V_{fl} = -\alpha T_e \approx -3.69 T_e$$

where V is the paddle floating potential measured in Volts, α is a gas-specific quantity, and T_e is the electron temperature measured in eV.

Figure 39. Magnetic field of the PFRC-2 in RMF-FRC mode, simulating the SOL and core of the DFD. Each chamber's name is given, in both PFRC-II and DFD terminologies.

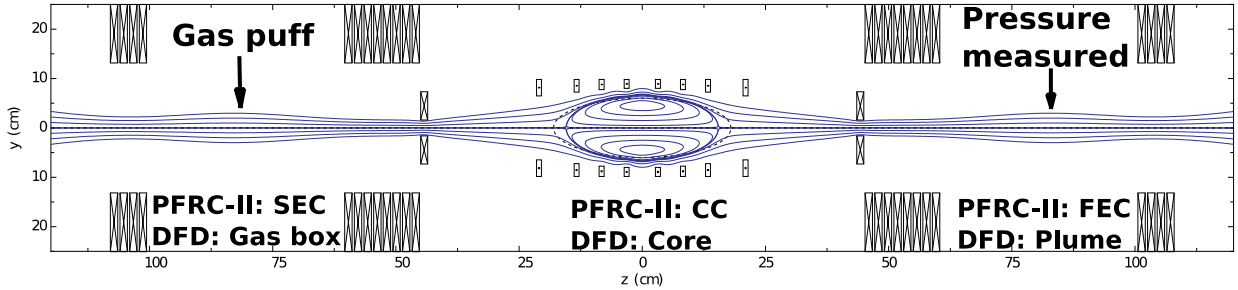

The next two sections provide results from the two experiments.

3.4.1 RMF Plasma

The RMF plasma of the PFRC-2 simulates the core and SOL of the DFD. When we performed RMF experiments, we measured a large gas pressure drop in the CC during the RMF pulse. Figure 40 shows this behavior. The red trace in the top pane shows the CC gas pressure; it falls by more than 70% over the course of the RMF pulse.

We attribute this behavior to ionization of the neutral gas by the hot (~ 200 eV), dense (~ 10^{12}/cc) FRC plasma which has formed. The neutral gas flows into the FRC due to its thermal motion, where it is ionized into plasma. Subsequently, collisional transport causes plasma to diffuse out of the FRC. We currently theorize that it flows along the magnetic field into the SEC and FEC but have not measured this process.

From the perspective of a strict analogy to the DFD, this is bad news. The SOL in the DFD is populated by the gas box, and flows uniformly from the gas box, through the core chamber, out into space. This measurement indicates that the SOL in the PFRC-2 is principally formed by material diffusing out of the FRC.

However, it does serve as a proof-of-principle for the plasma-mediated flow of gas between chambers of the DFD. A pressure drop of this magnitude implies that 500 ng (nanograms) of hydrogen gas was displaced over the course of 5 ms.

Figure 40. An oscilloscope screenshot showing a large decrease in gas pressure in the CC during an RMF pulse.

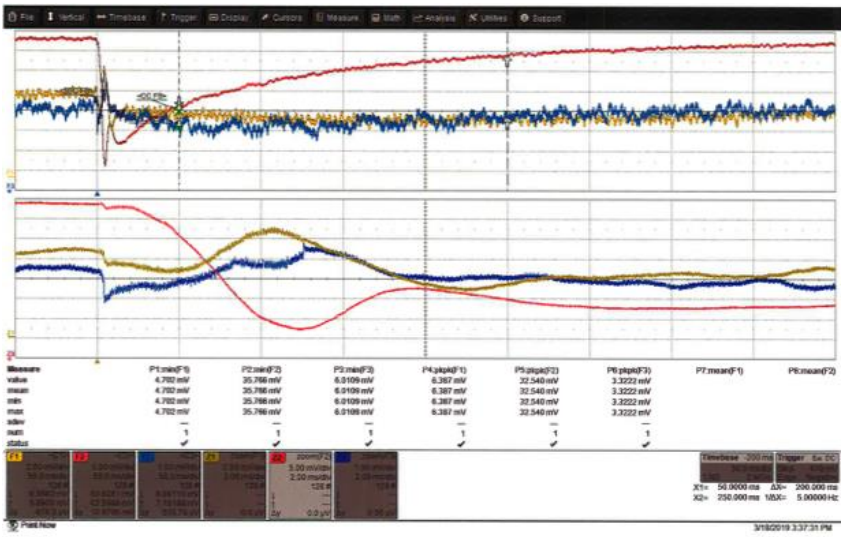

When we performed RMF experiments, we measured that the paddle in the FEC floated at -800 V during the RMF pulse, and -50 V when RMF was not active. From the Langmuir sheath criterion, we infer that the seed plasma temperature is about 15 eV, and that 215 eV plasma flows into the FEC during RMF operation. This measurement is shown in Figure 41.

Figure 41. Floating Paddle Potential

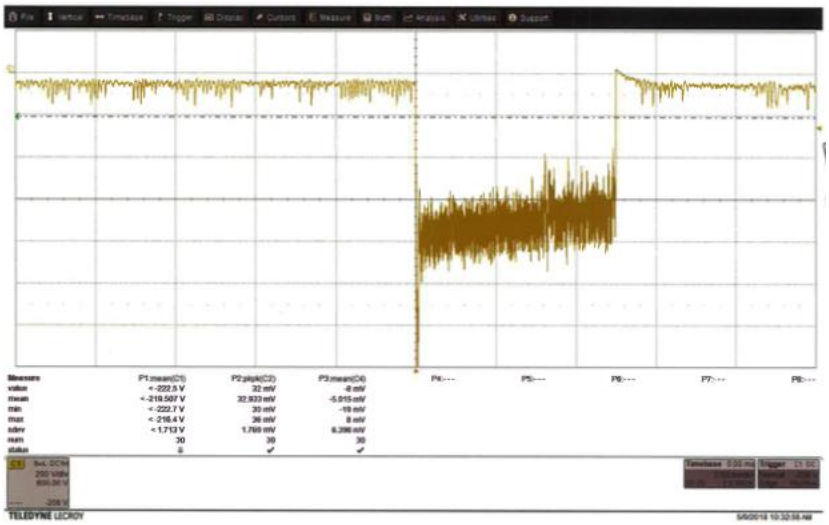

This measurement again lends itself to the interpretation that the SOL in the PFRC-2 is populated by FRC plasma which has left. This temperature is near the FRC temperature measured using X-ray detectors. There is no way to infer from the paddle floating potential the density of this plasma.

Differences in plasma density propagate at the ion sound speed. Differences in gas density propagate at the gas thermal velocity. For H2 gas in air vs H+ plasma at Te = 200 eV, this is a difference in velocities of 104, implying that plasma hastens the flow of gas by this factor.

3.4.2 Seed Plasma

To disentangle the effects of densifying the SOL and the decaying FRC, we performed experiments with the seed plasma only. This more closely mimics the DFD, as the DFD core will be more collisionless due to its higher temperature, so that the SOL will be primarily populated by the gas box rather than diffusion across the separatrix. We established a seed plasma in the PFRC-2, then injected more H2 gas into the SEC and measured the pressure and electrostatic response in the FEC.

Figure 42 show the results of this measurement. From left to right, top to bottom in Figure 42: Signal in the SEC showing an immediate increase in pressure and a decay over hundreds of ms. Signal in the CC showing gradual conduction of gas from the SEC to the CC over hundreds of ms. Signal in the FEC showing immediate conduction of gas from the CC to the FEC, too fast for gas flow. Another pressure diagnostics (ion gauge) in the FEC The SEC FB (Fast Baratron) measurements can be easily explained: When the gas puff begins, gas immediately flows into the SEC, increasing its pressure by 75%. The CC FB measurements can be explained likewise: The gas takes hundreds of milliseconds to flow through the 10 cm2 nozzle into the CC.

Figure 42. Pressure signals during seed plasma SEC gas puff shows plasma-mediated flow.

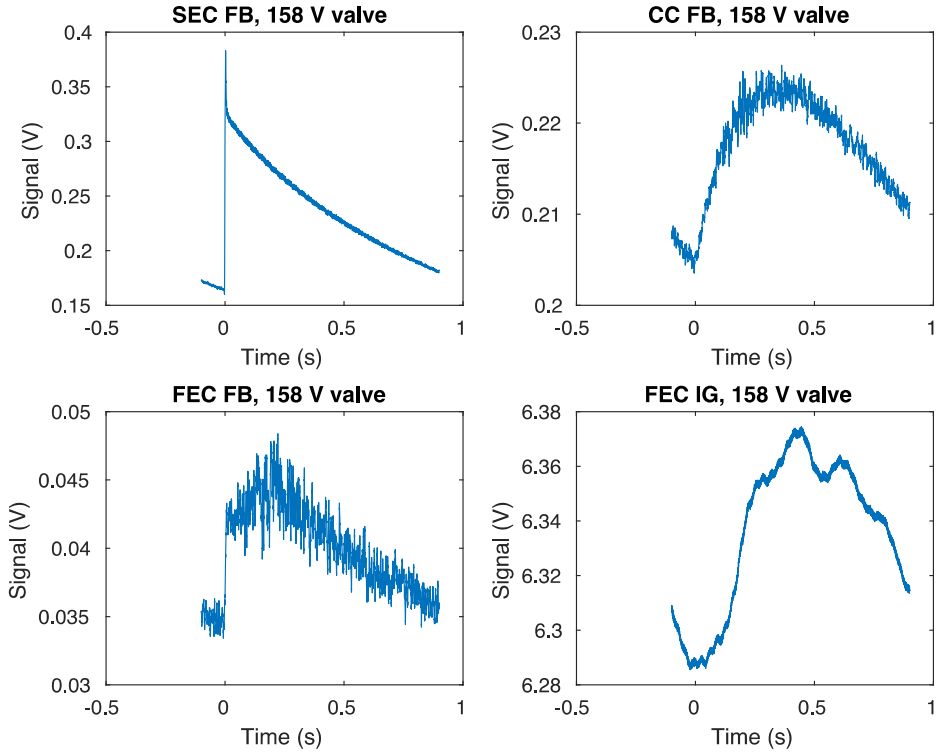

Figure 43. Pressure signals during SEC gas puff with no plasma, providing a control case.

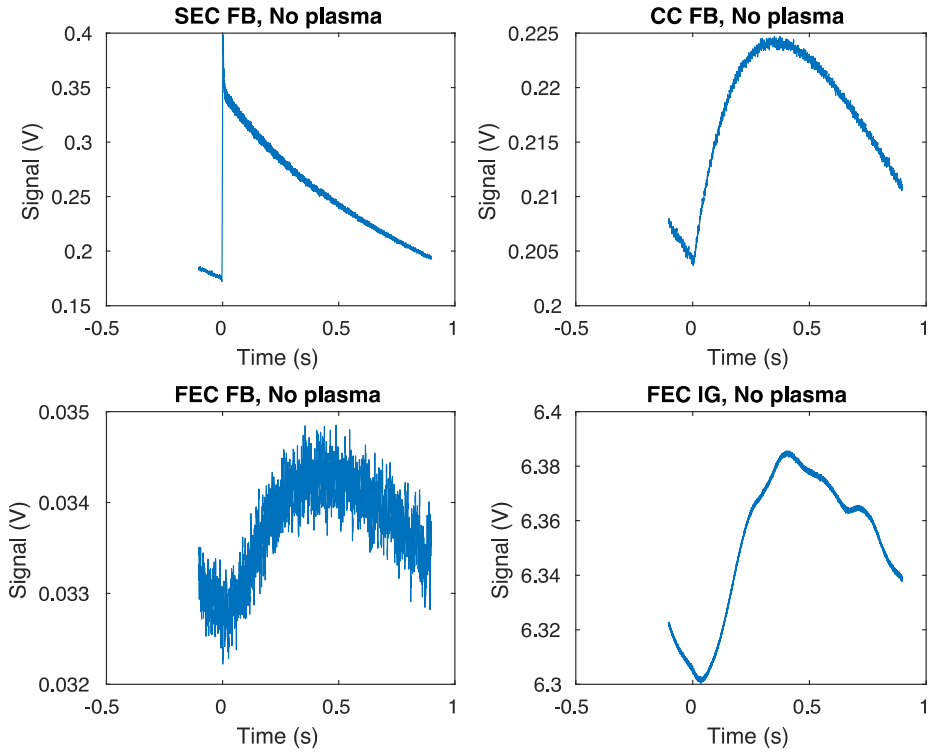

The FEC FB behaviors differ between the two cases: Figure 42 shows this quantity when seed plasma is present. Figure 43 shows this quantity when there is no plasma present. When the plasma is present, it takes only 5 ms for the pressure in the FEC to increase, and it increases 40%, as opposed to the hundreds of ms it takes to increase 6% when there is no plasma.

This experiment serves as another proof of concept, without diffusion along an FRC separatrix to muddy the waters. It is much closer to the DFD configuration, in that gas and plasma come from the SEC, flow through the CC without much augmentation, and end up in the FEC. In this configuration, increasing the gas in the SEC by 75% increased the gas flow to the FEC by 40% when a cold, tenuous plasma was present, as opposed to 6% when there was none.

3.4.3 Summary

Thrust augmentation experiments were planned to demonstrate the plasma-mediated flow of gas in a DFD-like configuration. We found that a straightforward comparison is impossible, as the PFRC-2 is much more collisional than the DFD will be, populating the SOL with plasma diffusing across the separatrix.

Despite this confounding factor, we have demonstrated the plasma-mediated flow of gas in a mirror-FRC system, and the plasma-mediated flow of gas upon the addition of a gas puff in a linear system.

3.5 RF Modeling

From the Phase II Proposal:

> During our Phase I we have developed a concept for replacing the current linear amplifiers with switching amplifiers, which have theoretically almost 100% efficiency. We need to continue to explore the handling of the harmonics in this case and the resulting coupling with the plasma. The objective is to quantify the resulting efficiency for the subsystem to within a few percent. This task will focus on antenna design and the power system interface. Actual amplifier design has been proposed under other programs (NASA STTR T2.01-9960).

Our NIAC work on this task was supplemented by a Phase I STTR we won, but we did not win a Phase II. A multi-transistor Class E amplifier was designed, see Figure 44.

Figure 44. Three transistor high power board.

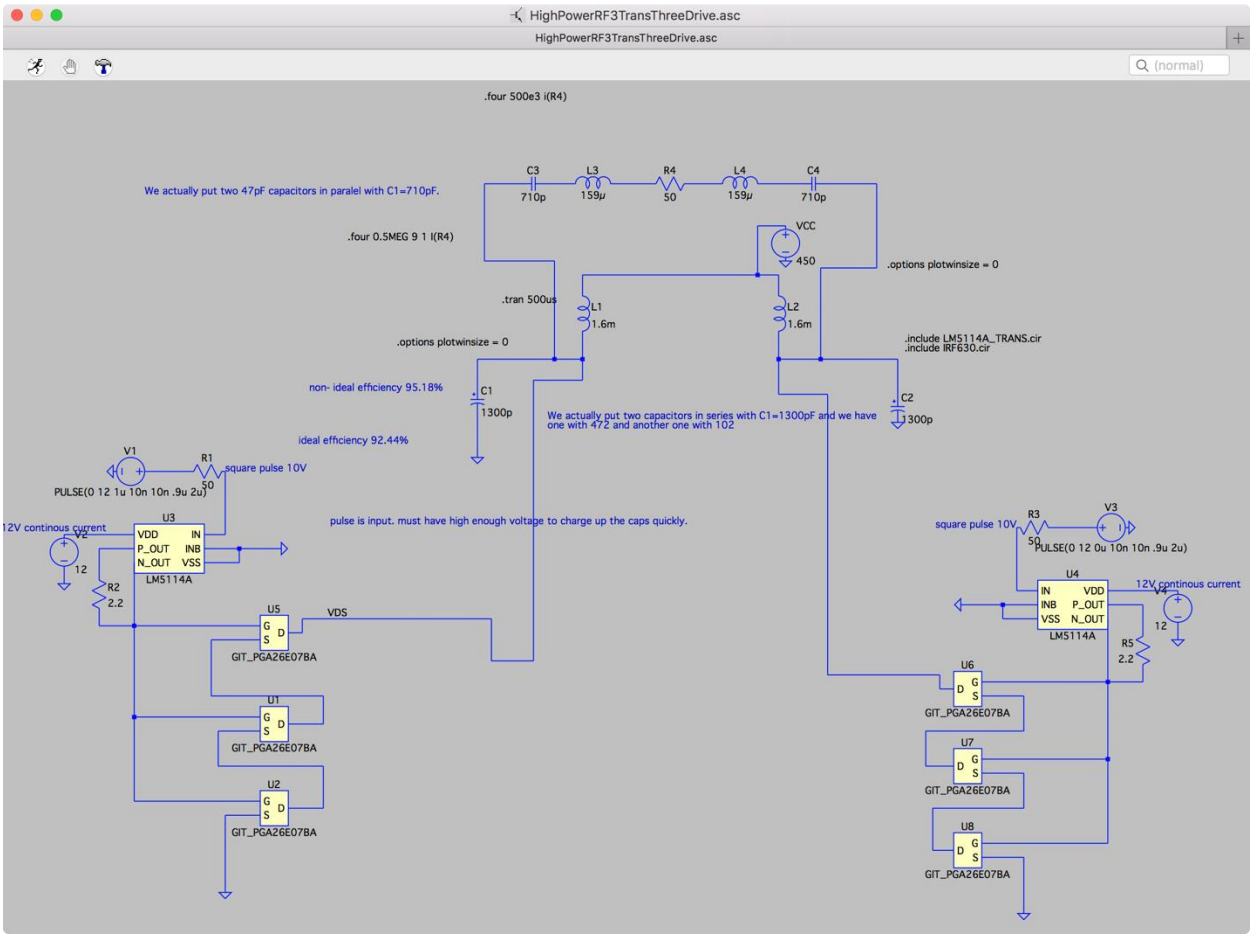

Each board can handle up to 10 kW using three GaN transistors in series. The boards are cooled using Thermacore k-Core graphite thermal material. It has 4 times the thermal conductivity of copper. Each coil element that faces the plasma would have a separate board. This eliminates the

need for combiners. The boards are driven digitally so synchronizing them is simple. This reduces the complexity of the analog circuitry.

3.5.1 Alternative Amplifiers

The goal of the amplifier board is to

1. Have high efficiency
2. Have low harmonics
3. Be tunable with no loss of efficiency
4. Can be built with components to allow 10 kW or more to be produced on a single board

While we call our amplifiers RF, their actual frequency is 1 MHz which is relatively low.

We investigated a wide range of amplifier classes. The first to be studied was the Class E amplifier. This is discussed above. It consists of a switch and a tank circuit that filters the resulting square wave producing a single frequency. If two switches are used, 90 degrees out of phase, the odd harmonics can be removed.

Class A, B and C are linear amplifiers. There theoretical maximum efficiency of Class A is 50% which is too low for this application. Class B can reach 78.5%. Class C have theoretical drain efficiencies of 100% but the amplitude of the current pulses must reach infinity making this impractical.

Class D, E and F are switching amplifiers. In Class D operation two transistors are used in a push-pull configuration. While capable of 100% efficiency it requires high switching speed. Class D is similar to Class E in the push-pull configuration.

Class E requires lower switching speeds and is very tolerant to switching speed and component uncertainty. The components are selected for one frequency. If implemented in a push-pull configuration, odd harmonics can be eliminated.

An alternative is an inverse Class E [19] with a digitally tunable parallel resonator on the output port. This can achieve 75% efficiency with a 2:1 frequency range. The Class E operates in the zero-voltage switching mode while the inverse operates in the zero-current switching mode, hence the “inverse” in the name.

Class F [20] can achieve 100% drain efficiency in theory by using harmonic resonators in the output matching network to shape the drain voltage and current waveforms.

3.5.2 Antennas

The current interface to the plasma uses 2-phase rectangular hoop antennas. Each rectangle is two hoops displaced radially. There are a total of 4 antenna pairs on each side of the centerline. We studied other antenna configurations but have not demonstrated that any particular antenna

configuration is superior to the current design. It was only late in the program where we began developing tools that would allow studies of aspects the plasma antenna interface. In addition, we do not yet have experimental verification of the ion heating with the current antennas which are needed to verify the tools under development. Full verification would require Particle in a Cell (PIC) simulations that could not be done under the NIAC Phase II budget.

An issue with an operational machine is that it may be necessary to put the antennas inside the pressure vessel if the conducting vessel is conducting. This means different antennas will be needed though the driving boards would not change.

3.5.3 New RMF Simulation

We have authored a new MATLAB RMF function that allows for high fidelity simulations of multiple individual particles in RMF fields. This is related to the Fortran RMF code authored by Alan Glasser and is similarly limited to sinusoidal waveforms. However, this version is more flexible, allowing us to add multiple RMF frequencies and arbitrary static field distributions. Both electrons and multiple species of ions can be simulated. Any number of (non-interacting) particles can be modeled. Confining fields (from the FRC) and external fields can also be simulated. This provides a powerful tool for studying plasma behavior in FRCs driven by RMF. Multiple RMF fields can be added at different frequencies. This will allow us to study control methods for reducing electron drag on ions and other effects. These techniques may greatly improve the performance of FRC based fusion engines like DFD. The graphics that are part of the function are useful for understand the complex plasma dynamics. Figure 45 shows an example particle trajectory. This function fills a void in our DFD plasma physics tool chain.

Figure 45. Particle orbits with a 50 gauss RMF field and a 100 gauss axial field

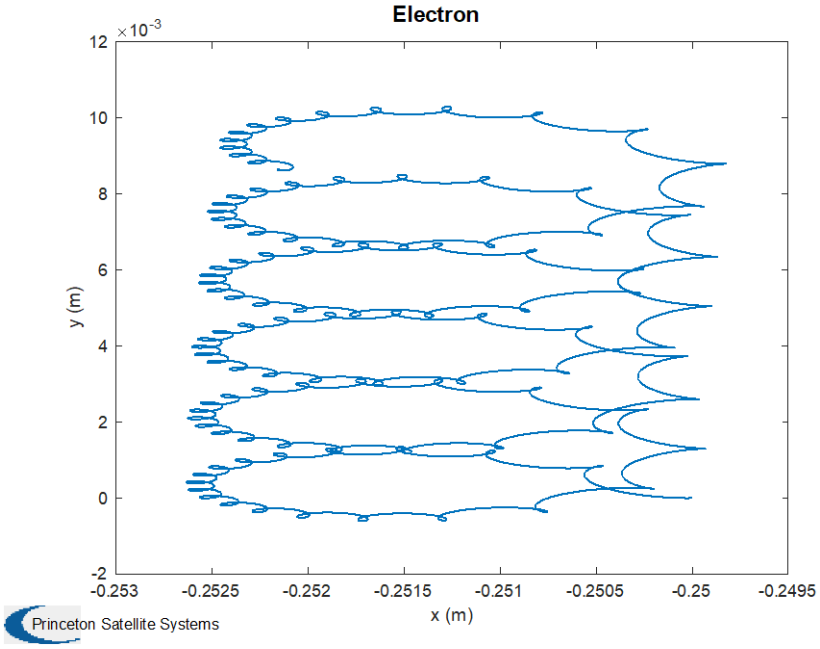

3.5.4 New 3D Electromagnetic Field Simulation

We have authored a new MATLAB EM function that allows for high fidelity simulations of 3D time varying electric and magnetic fields using Finite Difference Time Domain equations [21]. [21] This resolves finite-wavelength effects and produces self-consistent electromagnetic fields (unlike the RMF code). The current RMF code assumes a sinusoidal waveform. The new general-purpose code can handle any coil shapes and any waveform. The FDTD method is based on the approach of K. Yee (Figure 46). It allows efficient computation. It will be integrated with the particle engine shown above. This will allow arbitrary current distributions and arbitrary waveforms to be studied.

Figure 46. Yee cube. The H and E components are computed on different nodes.

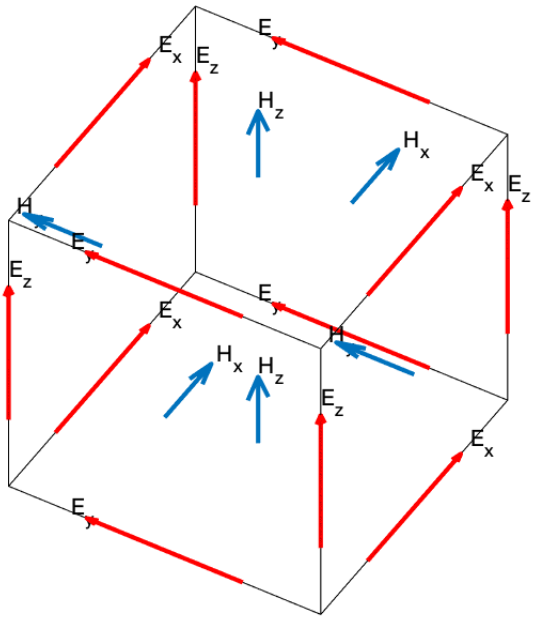

3.6 Closed-Loop Operation

From the Phase II Proposal:

> A new physics activity under this task is the evaluation of DFD engine performance in a power-generation mode where the propellant is captured and recycled. A capture mechanism would need to be inserted into the exhaust stream, to intercept the "propellant," which now only serves as "coolant." That is, once in Pluto orbit, there is no reason to expel the coolant gas as propellant. Capturing it for reuse will reduce the amount of D2 that would be needed. The heat from the propellant may then be captured and fed into the existing power conversion system, which may need to be adjusted in size for this mode. However, there is an interesting tradeoff in whether to recover the additional power or just cool the propellant for storage and radiate the power to space. To accomplish this study, we will modify the multi-fluid code

(UEDGE) to incorporate this novel new set of boundary conditions. We also need to evaluate the impact on the other systems, from the Brayton cycle to the radiators.

We have analyzed the plasma conditions in the capture volume to size a conceptual closed-loop system. The scrape-off-layer plasma hits the rear wall, recombines into atomic hydrogen and depositing the plume heat on the wall, where it can be radiated or converted into additional electricity. The atomic hydrogen can be pumped out of the chamber using turbopumps, or, transported out of the chamber via a superpermeable membrane. In tokamak terminology, this capture chamber is called a *divertor*. Figure 47 shows a diagram of the divertor chamber, with a tungsten-coated strike plate at the back, and membranes lining the side walls. Cooled hydrogen flow would then be pumped back to the source end of the reactor using ordinary roughing pumps. Our calculations show that this chamber can be about 1 m in length and diameter. To simplify operations, we assume that there is no mechanism for fusion product extraction and storage. Tritium is simply allowed to circulate in the SOL flow.

Figure 47. Diagram of the divertor chamber. Hydrogen flows in from left as plasma, is recombined on the divertor plate, superpermeates through a membrane (dashed line), and is pumped away.

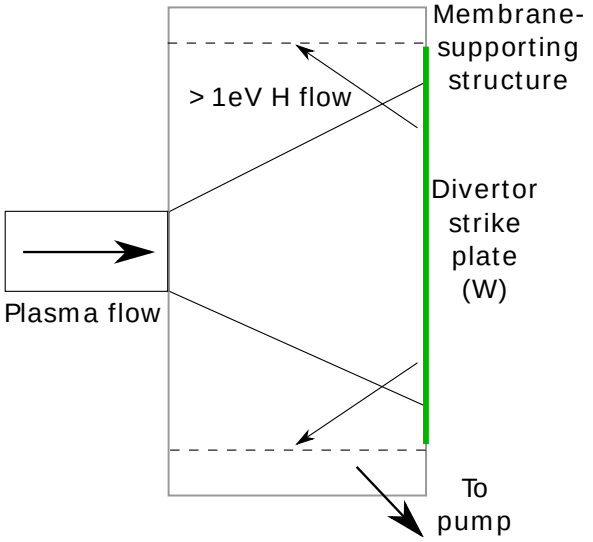

Superpermeability is a phenomenon in which a dozen-micron-thick metallic membrane may become largely transparent to eV-energy atomic hydrogen, while remaining opaque to thermal molecular hydrogen or higher-Z species. This allows a superpermeable membrane to act as a pump specifically for hydrogen. Superpermeability is currently considered for use near Tokamak divertors for hydrogen-specific pumping.

The membrane would replace about 275 kg of turbopumps with just 20 cm^2 of membrane surface. Superpermeability, which has been demonstrated experimentally, is a delicate chemical condition which can be degraded by temperature, plasma bombardment, and impurities. A dedicated development program would be required to bring the technology to maturity, but it has the potential for this component to have almost negligible effect on the reactor's specific power.

Table 16. Closed loop operation parameters and components

Parameter	Value
Chamber diameter	1 m
Chamber length	1 m
Tungsten thickness	<1 mm
Total tungsten mass	< 10 kg
Membrane area	20 cm^2
Membrane thickness	<50 microns
Total membrane mass	~ 1 kg
Chamber pressure	0.3 mTorr
Duct pressure	0.3 Torr
Gas box input pressure	100 psi

3.6.1 Superpermeability

Superpermeability is a phenomenon observed in which a macroscopic (dozens of μm thick) metallic membrane can become almost transparent to the flow of hot (>1 eV) atomic hydrogen. The transmittance of atomic hydrogen can be above 90%. The phenomenon is highly selective of hot atomic hydrogen of any isotope; H, D, or T may pass while He, H_2, etc. may not. The membrane material may be any of a number of metals, such as palladium, stainless steel, niobium, or iron.

During the hydrogen's passage through the bulk metal, it is cooled. During the desorption process, it reacts with another hydrogen atom to become molecular hydrogen (H2). [22] The process of superpermeability can compress the hydrogen gas by many orders of magnitude (> 10^4), having the effect of pumping hydrogen from one side of the membrane to the other.

The mechanism of superpermeability is chemical in nature. [22] [23] By one of many means, a surface coating occurs on the upstream side of the membrane which prevents molecular H_2 from adsorbing. Once a hydrogen atom is within the bulk metal of the membrane, this layer acts to prevent the formation of H_2 on the upstream side, so the hydrogen must diffuse through the bulk material and desorb on the downstream side.

The chemical treatments of the upstream and downstream side are very sensitive. Ion impact from plasma can clean them off and degrade superpermeability. Membrane temperature can enhance or inhibit their formation. Impurities on either side show strong dependence.

Superpermeability (sometimes called metal foil pumping) has been suggested for use near Tokamak divertors. [23] [24] [25] In these proposed concepts, superpermeable membranes line the pump duct near the divertors, so that a large proportion of superthermal deuterium and tritium produced by surface recombination is incident on the membrane after a small number of bounces. Furthermore, thermalized molecular hydrogen gas is incident on a hot filament (sometimes called an atomizer), which has the effect of dissociating the molecules into atoms

each with the Franck Condon dissociation energy (2.2 eV). This is sufficient for superpermeability.

The membranes are backed by roughing pumps. Tokamak studies find the following advantages of this concept:

- Membrane and roughing pumps do not need to be recharged, unlike cryopumps
- Hydrogen is automatically separated from other species
- Tritium is kept very close to the Tokamak

In the PFRC, the divertor strike plate itself is not a superpermeable membrane, as it must withstand potentially 1 - 2 MW/m^2 of power density in the form of plasma flow. Rather, the walls of the divertor chamber with line-of-sight to the divertor strike plate support areas of superpermeable membrane. See Figure 47.

Superpermeable membranes are typically 10 - 100 μm thin. Because of this, they are quite fragile. A large area of micron-thin membrane is impractical. Any large area will of necessity be only superpermeable over a portion of its surface area, with the rest being thicker mechanical support. This decreases the effective superpermeability fraction, χ, by this ratio.

Much of the plasma power goes into heating the divertor strike plate, but a fair portion is also incident on the walls of the divertor chamber and therefore on the superpermeable membrane. The tables of Ito et. al. contain backscattering number coefficients and energy coefficients for hydrogen incident on many surfaces. [26] For hydrogen atoms incident on tungsten at energies lower than 10 eV, the backscattering number coefficient is about 60% and the backscattering energy coefficient is about 45%. This means that 45% of the plasma power is incident on the walls of the divertor chamber.

It may not be possible for the superpermeable membrane to withstand this power flux. In this case, the membrane should not have direct line-of-sight to the strike plate; rather atoms should have to bounce a small number of times before being incident on the membrane. There is a minimum possible energy per particle however; below about 1 eV, superpermeability is degraded. As transiting hydrogen atoms are cooled during superpermeation, most of this 1 eV is transferred to the membrane.

As can be seen from the tables of Ito et. al., a large portion (40%) of low-energy hydrogen atoms incident on a tungsten surface do not backscatter. In this case, they accumulate until the tungsten is saturated with hydrogen, whereupon they desorb as molecular hydrogen with the temperature of the surface.[8] This thermal molecular hydrogen may not be superpermeated.

A hot filament, like the kind proposed for use in Tokamaks, can be used to dissociate molecular hydrogen. [24] [25] Upon dissociation, each hydrogen atom attains the Franck Condon dissociation energy, 2.2 eV. This is sufficient for superpermeation. The filament can be placed anywhere in the divertor chamber, where it will act as a localized pump for molecular hydrogen.

We will now calculate a suitable area of superpermeable membrane to pump the divertor. The thermal flux Γ of a Maxwellian distribution of atoms at temperature *T* with particle density *n* is

$$\Gamma = 1/4nv$$

where

$$v = 2\sqrt{\frac{2T}{\pi m}}$$

Total particle pumping rate is

$$R = \chi \Gamma A$$

where *R* is the particle rate, χ is the permeation fraction, Γ is the flux of incident particles, and *A* is the pump inlet area. R is computed from the Sheath Conduction Factor γ, which is the energy in units of electron temperature that an ion-electron pair delivers to the strike plate. In our case γ is about 8 (Langmuir sheath model), so $P = \gamma R T_e$. For every MW of plume power entering the divertor, this gives a particle rate R of 3e22 ions/s/MW. Assuming a temperature of T_e = 30 eV, to pump 1e13/cc atomic deuterium at 1 eV with χ = 0.9 will require 6,300 cm^2 or 0.63 m^2 of superpermeable membrane.

The alternative to superpermeable membrane would be standard turbopumps, which might be 100 kg each. Several would be required. A typical compression ratio for a turbopump is 100×. For superpermeable membranes, 10^4× has been achieved. This is another large increase, allowing the backing pump to pump gases at 100× higher pressures.

3.6.2 Chamber Plasma Parameters

The capture chamber of the PFRC is exactly analogous to a divertor in a tokamak. We will apply a two-point, or 0D, model of a conduction limited divertor to size our chamber. The model suggests that the DFD can operate in conduction-limited mode with high SOL density $n_{SOL} \sim 3 \times 10^{19}/m^3$, however even in the sheath-limited regime, the lower energy flux of the DFD makes the divertor plasma temperature sufficiently low to allow a tungsten divertor.

The recycling coefficient is the probability that an ion incident on the divertor wall will be re-incident on the plasma rather than being pumped away. In a high-recycling divertor, the same atom may be re-ionized and recombined many times before it leaves the system. In the extreme limit of a high-recycling divertor, volumetric recombination and impurity radiation causes significant loss from the plasma before it reaches the divertor plate. This is called a detached divertor and is used when the power flux to a surface would otherwise be too high. [27] [28]

A divertor is said to be in the Conduction Limited Regime (CLR) when the power flow from the SOL into the divertor is limited by the electron thermal conductivity along B. Both the high-recycling divertor and the low-recycling divertor are in this regime. The detached divertor is not. The electron thermal conductivity is a measure of what energy flux is produced when there is an electron temperature gradient. The electron thermal conductivity κ is a strongly varying function of temperature, becoming more conductive at high temperatures with a 5/2 coefficient:

$$\kappa = \kappa_0 T^{5/2}$$

where κ_0 is a constant, not dependent on the plasma density or temperature, which has numerical value $\kappa_0 = 2000$ Watts/eV$^{7/2}$ m or $\kappa_0 = 6.3 \times 10^7$ MW/keV$^{7/2}$ m over the parameter regime of interest. [29]

The two-point model is a model which relates the temperatures and densities at two points: One where power is deposited into the SOL and one which is just upstream of the sheath where the SOL hits the divertor plate. These are termed n_u, T_u for the upstream density and temperature and n_t, T_t for the target plasma density and temperature. The best explanation of this model is in Stangeby, although earlier papers produced equivalent models. [30] [31]

The upstream plasma is assumed to have no net flow. The target plasma is assumed to be flowing into the divertor plate at the ion sound speed, M = 1 where M is the Mach number. The equation for pressure balance between the two points is therefore

$$2 n_t T_t = n_u T_u$$

where the factor of 2 comes from the dynamic pressure of the M = 1 flow. At each point, energy flux q is assumed to be flowing downstream. Since the flux is $q = -\kappa \nabla T$, integrating we have

$$T_u^{7/2} = T_t^{7/2} \frac{qL}{\kappa_0}$$

where L is the connection length along the field line. L can be 100 m in tokamaks but can only be of order 1 m in the DFD. The point just downstream of the sheath also must have energy flux q,

$$q = \gamma \, e \, n_t \, T_t \, C_t$$

where γ is the energy conduction factor (the energy, in T_e, deposited into a surface per ion-electron set) determined from Langmuir sheath theory, $\gamma \approx 8$ in this case, e is the electron charge to convert units between T_t and q ($e = 1.6 \times 10^{-19}$ Joules / eV; if energy units are consistent this is not necessary), and C_t is the ion sound speed.

We have implemented a MATLAB solver which finds T_u, T_t, n_t given q, n_u, L. The solver is stable both in the parameter regime in which $T_u \gg T_t$ and in the parameter regime in which $T_u \sim$

T_t. Results of the model for the JET tokamak and three potential operating points for the DFD are given in Table 17.

Table 17 Conduction Limited Divertor Calculations

Quantity	JET	low-n DFD SOL	mid-n DFD SOL	high-n DFD SOL
q	10^8 W/m^2	10^6 W/m^2	10^6 W/m^2	10^6 W/m^2
n_u	3 x 10^{19} m^{-3}	10^{18} m^{-3}	3 x 10^{18} m^{-3}	3 x 10^{19} m^{-3}
L	50 m	1 m	1 m	1 m
T_u	97 eV	32 eV	15.6 eV	8.4 eV
T_t	39 eV	32 eV	15.1 eV	0.52 eV
n_t	3.7 x 10^{19} m^{-3}	5 x 10^{17} m^{-3}	1.6 x 10^{18} m^{-3}	2.4 x 10^{20} m^{-3}

In the table, it can be clearly seen that even a low-density SOL, while not sufficient to cause a large temperature drop, is entirely sufficient to maintain a reasonable target temperature T ~ 30 eV. An increase in density is sufficient to cause a sizable temperature drop, down to temperatures at which a detached divertor model must be used, T ~ 0.5 eV.

The two-point is a 0D model, as it considers only two isolated points. When 2D measurements are performed on tokamaks, an odd effect is observed: the SOL plasma circulates, with hot plasma coming to the divertor via the radially outward field lines and cold plasma returning to the main chamber via the radially inward field lines. The cause of this circulation is not yet well known. Despite this, the two-point model is fairly good at predicting the results despite lacking some important dimensions.

Where the two-point model breaks down is when volumetric processes such as recombination, plasma-neutral momentum loss, and impurity radiation are important. These occur at low temperature, $T_t < 10$ eV. [32] There is not an equivalent model for detached divertors, or as one author states "As detachment is a 2D strongly coupled nonlinear process a quantitative description is only possible with extensive code simulations." [33]

3.6.3 Divertor Erosion

The strike plate in the divertor will be impacted by several populations of particles: bulk SOL plasma, fast core charge exchange neutrals, fast fusion products, SOL impurities, and sputtered divertor particles. We have formulated an analytic model of the net erosion of a tungsten plate. Our analysis shows that impurities and previously sputtered tungsten have the largest effect. However, redeposition of the sputtered tungsten occurs just a few mm away, so that the net effect is minimal and easily mitigated.

Divertor erosion and redeposition in Tokamaks is a developed field, with dedicated experiments and codes. Simulations find that the erosion rate from tungsten divertors is "predicted to be zero" and that the redeposition portion is "essentially unity," [34] and experiments find agreement, "Sputtering performance excellent for Te < 50 eV. Long erosion lifetime with essentially zero

plasma contamination." [35] In other words, redeposition has been predicted to reduce sputtering erosion to barely measurable levels.

Sputtering

Sputtering is observed in the FEC of the PFRC-II experiment, during low power RF mirror operation. Ions, accelerated by the measured potential drop between the CC and the FEC, are incident on a tantalum paddle which terminates the plasma column. This configuration is observed to sputter-coat a nearby sapphire window with tantalum. The threshold energy for a hydrogen atom to sputter a tantalum atom is quite high, ~400 eV.

The divertor plasma will be deuterium-dominated. When plasma is incident on a surface the ions attain the sheath energy E_i:

$$E_i = Z\alpha T_e$$

$$\alpha = \frac{1}{2}\left(\ln\left[\frac{m_i}{2\pi m_e}\right] + 1\right) \approx 3.69$$

where E_i is the energy that the ion gains upon falling through the sheath, Z is the charge state of the ion, T_e is the electron temperature, m_i is the majority ion mass (here, deuterium, giving α of 3.69), and m_e is the electron mass. The sputtering thresholds for incident ions on Tungsten [36] are:

- H: 409 eV
- D: 217 eV
- T: 145 eV
- He: 109 eV
- C: 38 eV

If an ion impacts a surface with less than this energy, no sputtering occurs. The sputtering threshold is a function of the energy necessary to remove an atom from the lattice (8.9 eV for tungsten) and the mass ratio of the incident and target species (183.8 g/mol for tungsten). Thus, to prevent thermal deuterium from the divertor edge from sputtering a tungsten surface, we have the condition $T_e < 59$ eV. If the SOL energy impacting the divertor is less than this, we can essentially neglect sputtering from the SOL plasma itself.

Fusion products of D-3He and D-D are tritium (1.01 MeV), helium-3 (0.82 MeV), helium-4 (3.5 MeV, 3.6 MeV), protium (3.02 MeV, 14.7 MeV), and neutrons (2.45 MeV, 14.1 MeV). The neutrons are lost to the walls. The fusion products slow down significantly before exiting through the nozzle; how much they slow down, and their energy spread is still an area of active research. As a worst-case scenario, we can assume that the fusion products impact the divertor plate at the energy which maximizes sputter yield. Assume that helium-4 ions impact the divertor

with 5 keV of energy. The sputtering yield of helium on tungsten at this energy is 5.0 × 10−2 (atom/atom) [37]. Per Mw-year of incident energy, this is 167 grams of tungsten.

Impurities are known to greatly affect the erosion rate in tokamaks. Impurity particles are both higher charge state and higher mass, both of which can increase sputtering yield by orders of magnitude. However, impurities can also inhibit erosion, such as a well-studied tendency for carbon atoms to adhere to tungsten divertors, shielding them from impacts. [38]

For an impurity example, consider a carbon impurity atom. Z is +4, so that the energy E_i when the impurity hits the surface is 442 eV for a T_e of 30 eV. The sputtering yield of carbon on tungsten at 442 eV is approximately 0.2. If the SOL plasma comprised 0.01% carbon atoms, the sputtering yield would be 7 kg per MW-year. This sputtering rate is significantly reduced if the T_e at the edge is significantly colder, as in a detached or high- recycling divertor. In tokamaks, the source of carbon impurities is usually graphite tiles.

Finally, consider self-sputtering of the tungsten divertor material. In the parameter regime of interest, sputtered tungsten atoms are ionized shortly after leaving the surface. This tungsten ion is incident on the surface yet again, and due to its high charge state picks up many times the T_e of energy. The sputtering yield of tungsten on tungsten is greater than 1 at approximately $E_i \sim 700$ eV; if this condition is met, there can be a self-reinforcing cascade of tungsten self-sputtering which disrupts the plasma. [34] It is this condition which leads tokamak designers to limit plasma temperatures striking tungsten to below 50 eV.

Redeposition

The characteristic ionization distance λ, which is also the characteristic redeposition distance, may be computed using the rate constant for ionization in a Maxwellian plasma:

$$\lambda = \frac{v_a}{\langle \sigma v \rangle (T_e) n}$$

where λ is the ionization mean free path, v_a is the velocity of the sputtered atom (ejection energy is approximately the sublimation energy, 8.9 eV for tungsten [39]), n_p is the plasma density, and $\langle \sigma v \rangle (T_e)$ is the rate constant for ionization in a Maxwellian plasma of temperature T_e. This quantity is obtainable for tungsten via integrating cross sections found via experiment or computation. [40] λ is inversely proportional to n_p. λ is a decreasing function with T_e, but sublinearly so that λ increases by a factor of ∼2 when T_e is decreased from 30 eV to 10 eV. At T_e =30 eV, np =8×10^{12}/cm^3, λ∼5 mm. This is the distance the atom travels across the surface.

For the analytical redeposition model, assume that there is a material with a 1D height profile h(x). The material has lattice constant (inter-atomic spacing) Δh. There is an incident flux of material $\Gamma(x) = 1/(\tau(x)\Delta h 2\gamma)$ sufficient to sputter away a monolayer Δh in time τ(x).

The erosion from this surface $(\partial h)_E$ is simple to calculate:

$$(\partial h)_E = -\Delta h^3 \gamma \Gamma(x)$$

The redeposition model must assume some profile for the distances from the emitted point at which the particles are re-deposited. We assume a Gaussian profile with standard deviation λ, previously shown to be about 5 mm in the parameter range of interest. This gives us a redeposition model of

$$(\partial h)_R = \int x' \frac{\Delta h^3 \gamma \Gamma(x)}{\lambda\sqrt{2\pi}} e^{-\frac{(x-x')^2}{2\lambda^2}}$$

Where the net sputtering is the combination of gross sputtering and redeposition:

$$\partial h = (\partial h)_E + (\partial h)_R$$

At first look, this appears to be a diffusion process. However, it is not. The right-hand-side of the redeposition equation cannot be made into a Green's function because the process is not linear: only the top monolayer of a surface is susceptible to sputtering at a time. This model has aspects in common with, and aspects which differ from, a diffusion model. As in a diffusion model, particles tend to move from areas of high flux Γ(x) to areas of low flux. Contrary to a diffusion model, particles' scale lengths into a hollow do not grow over time.

Table 18 shows the impact of a taper in the incident flux over some distance, L, as a function of the ratio of L to the characteristic ionization distance λ. For a sharp edge to the flux, L<< λ, the net erosion is one-half of the gross erosion. As the flux decays over a longer distance, the net erosion is further mitigated. Given λ for a T_e of 30 eV is only 5 mm, even 10 λ is just a few cm.

Table 18. Maximum ratio of net erosion to gross erosion

Case	Maximum net erosion / gross erosion
L << λ	0.5
L = λ	0.3
L = 2 λ	0.2
L = 5 λ	0.08
L = 10 λ	0.04

Figure 48 and Figure 49 show results of the model for two values of the ratio of L to λ. The first case shows a small L with a net erosion of one-half of the gross erosion. (Erosion only is shown in a separate line so that the effect of redeposition is clear). The second case shows a value of 2λ, where the net erosion is 20% of the gross erosion (reduction of 80%). Note the shape of the redeposited material with a raised edge. These results indicated that erosion may be further mitigated, potentially, by sweeping the plume to change the strike point over time. This would smooth out the ridges and trenches that form at the edge of the plasma beam.

Figure 48. Step Model in Flux, L < λ – Erosion reduced by one-half.

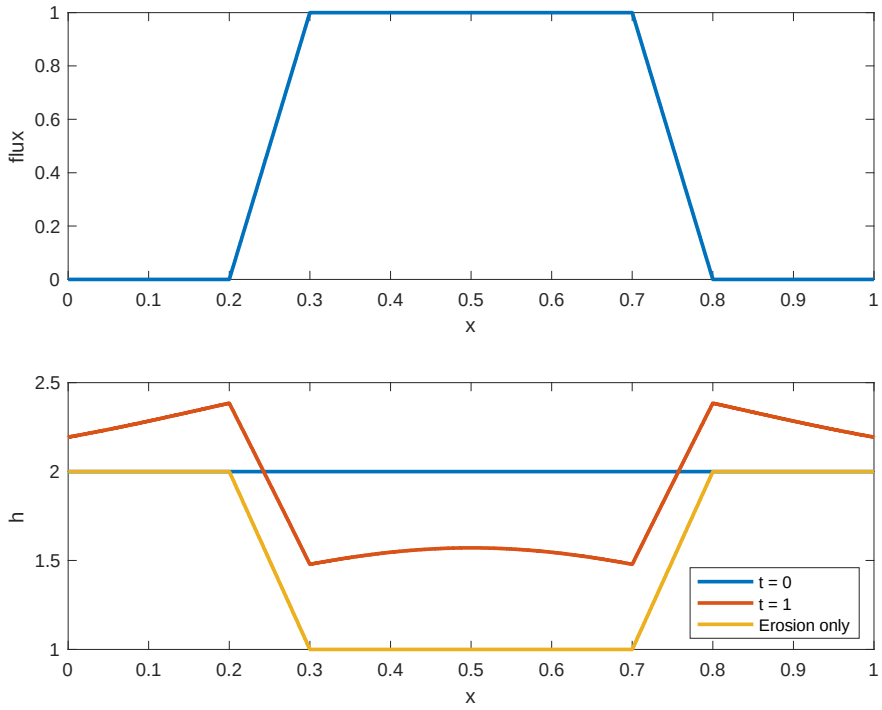

Figure 49. Step Model in Flux, L = 2λ - Erosion Reduced by 80%.

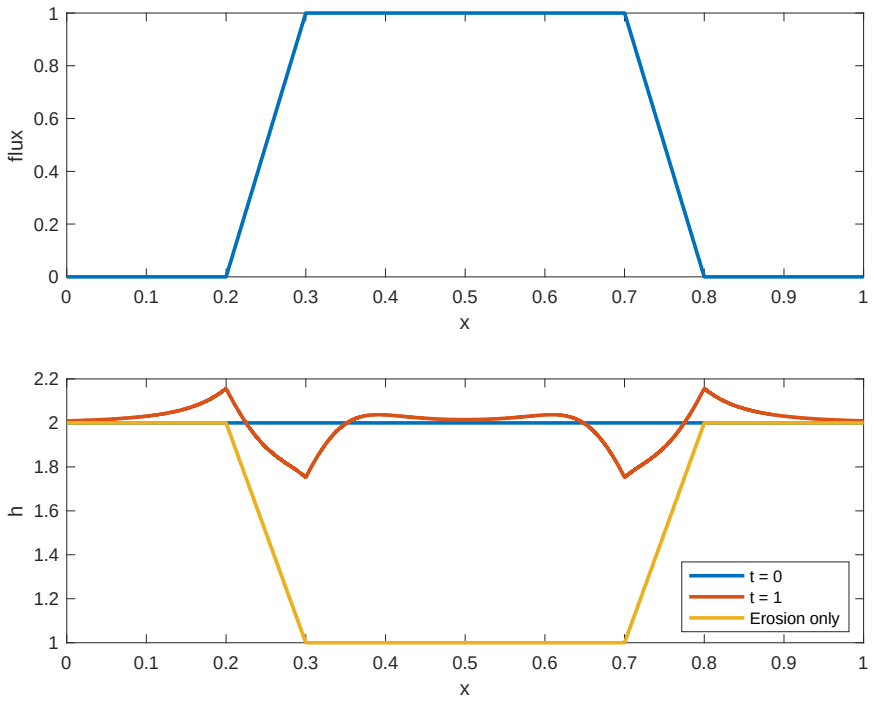

A more nuanced and accurate analysis of erosion in the DFD divertor in the future, considering impurities etc., will likely require the use of the tools developed for tokamaks.

3.6.4 UEDGE Modeling of Closed-Loop System

As well as using the analytic two-point model, we have modeled the closed-loop operation of the DFD using the 2D multifluid code UEDGE. UEDGE is able to capture more effects than a 0D model, including spatially resolved flows, ion-neutral interactions, and the effect of an expanding magnetic field.

This last effect, the expanding magnetic field, has proven to be important. Figure 50 shows the electron temperature as a function of position within the SOL. This behavior is as expected, with the electrons hottest (25 eV) in the core chamber and cooling (to 5 eV) in the divertor chamber. In the two-point model, this would be due to the finite thermal conductivity of the ~2.5 meters between the core midplane and the divertor plate, and we would expect a consequent increase in electron density. However, in Figure 51 we see that the electron density actually decreases due to the effect of the expanding magnetic field.

Figure 50. UEDGE Closed-Loop Electron Temperature (B. Taylor)

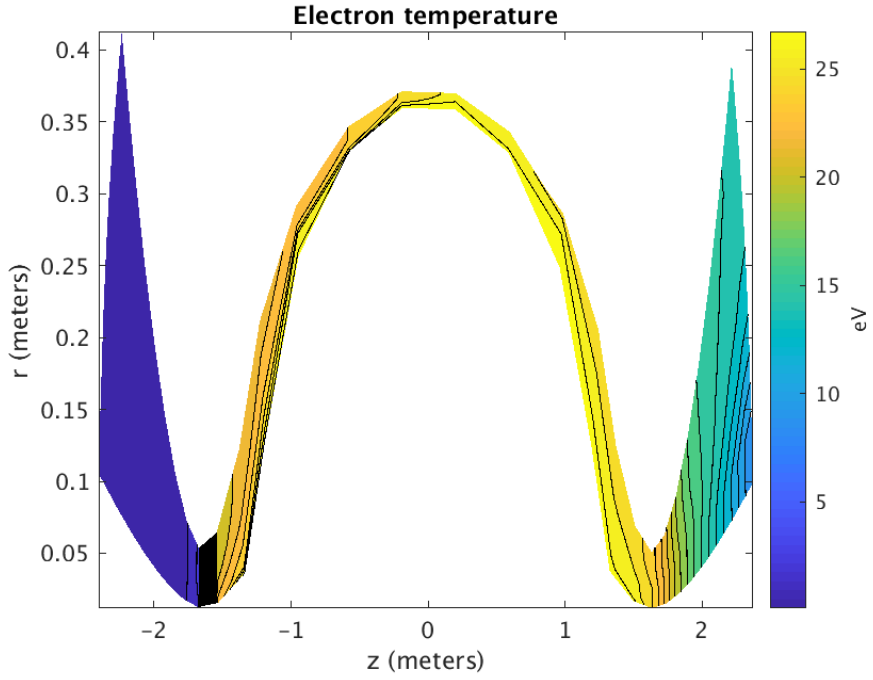

The UEDGE model largely agrees with the two-point model otherwise, predicting similar densities and temperatures in the SOL. The parameter ranges predicted from UEDGE are $n_e \approx 1 \times 10^{18} - 1 \times 10^{19}/\mathrm{m}^3$, $T_e \approx 5 - 15$ eV. This puts the power flux to the wall at $q \approx 0.5 - 1\ \mathrm{MW}/\mathrm{m}^2$, less than or in marginal agreement with the two-point model.

The effect of recycling on the divertor can be seen in Figure 52. The recycling coefficient is the probability that an ion will be neutralized, rather than lost, at the wall. It is an input to UEDGE and is a proxy for inverse pumping speed. As the recycling coefficient increases, the temperature

of the SOL in the core chamber does not change by much, but the temperature at the divertor plate ("exhaust plate" in the figure) decreases by a large amount. This qualitatively demonstrates one consequence of the two-point divertor model, that temperature at the target is much more sensitively dependent on density perturbations than the core SOL temperature.

Figure 51. UEDGE Closed-Loop Electron Particle Density (B. Taylor)

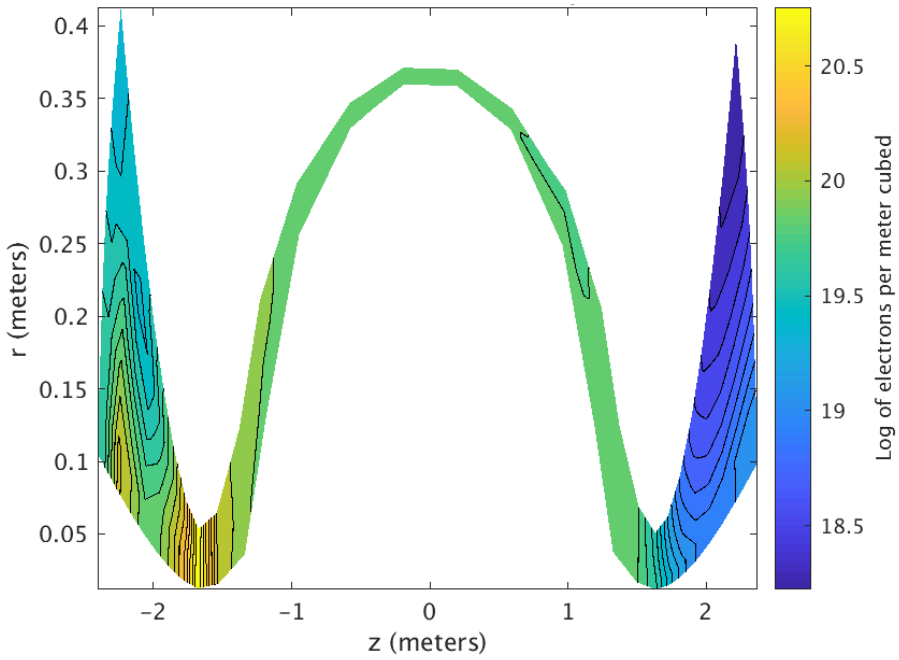

Figure 52. Effect of Recycling on Electron Temperature (B. Taylor)

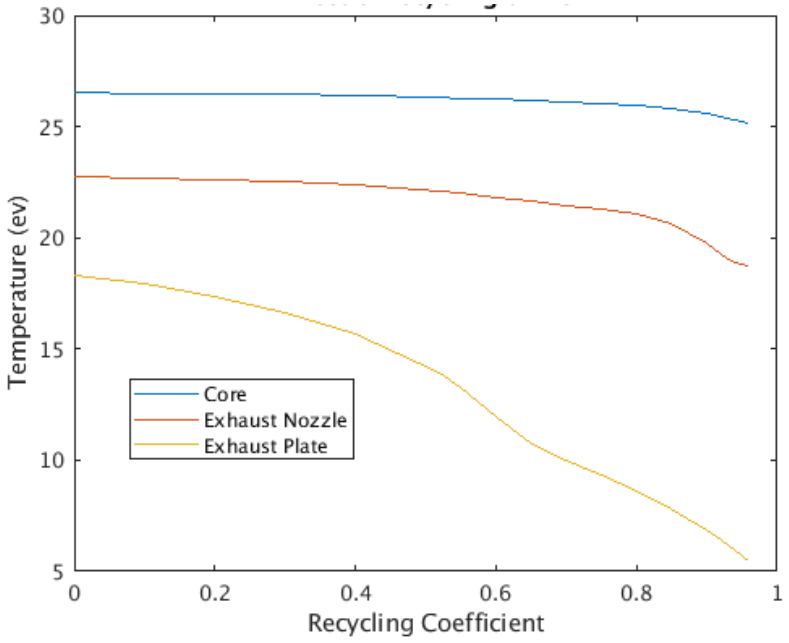

The UEDGE model also gives quantitative predictions of the divertor chamber neutral gas pressure. With the same conditions above, $n_e \approx 1 \times 10^{19}/\mathrm{m}^3$, $T_e \approx 5$ eV, the core chamber contains $10^{14}/\mathrm{m}^3$ of neutral gas, corresponding to a fill pressure of 3×10^{-6} Torr, and the divertor chamber contains $10^{19}/\mathrm{m}^3$ of neutral gas, corresponding to a fill pressure of 0.3 mTorr.

3.6.5 Notional Chamber Design

In conclusion, a low-density SOL in our divertor will be sufficient to maintain a target temperature T ~ 30 eV which enables use of a tungsten-coated strike plate. Eroded Tungsten is expected to redeposit nearby, maintaining sufficient coating thickness. The tungsten layer can be less than 1 mm thick, on the order of 10 kg. We have not exhaustively compared metals and other metals like tantalum could be considered in the future. We envision a set of vanes or petals comprising the chamber end plate which can be closed for closed-loop power operation and opened for thrusting operation. These vanes must be actively cooled and connected to the system's thermal system; they will be absorbing about half of the reactor output.

Superpermeable membranes can be used to pump the atomic hydrogen (and deuterium and tritium) out of the chamber. These add almost negligible mass to the chamber, although they must be supported by structural members. Additional roughing or backing pumps will be needed to pump the hydrogen back to the source end of the reactor. These should not contribute more than a few kg to the overall mass.

Finally, if we are extracting more power in the form of heat from the divertor chamber, we need to size up the thermal conversion system, including the radiators. The thermal conversion system itself is expected to be perhaps 15% of the total reactor mass, but the radiators are as much as 30% of the reactor mass. Figure 53 shows the scaling with input power for two sets of radiator temperatures with anticipated future mass properties. On the optimistic side, a change from 500 kW to 800 kW input heat is an increase in radiator mass from 200 to 325 kg; on the pessimistic side, it increases from 775 kg to 1240 kg, in both cases an increase in mass of 60%.

Figure 53. Radiator Scaling as a Function of Input Power and Temperature

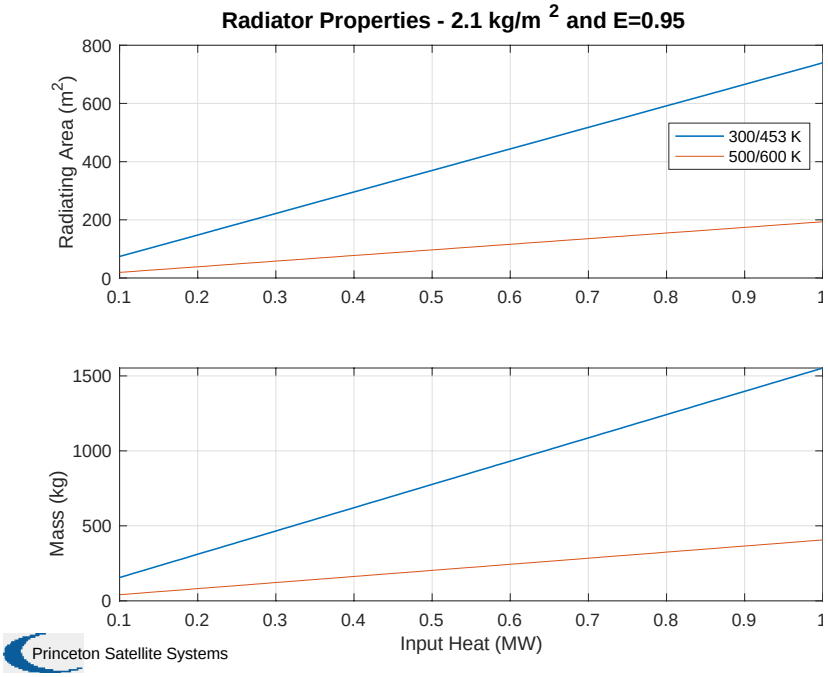

3.6.6 Thermophotovoltaic Conversion

While performing our analysis of the closed-loop power mode, we have discovered a new potential method of thermal conversion. The concept pairs a simple gas "working fluid" with molecular spectral lines with a tuned photovoltaic semiconductor, with a bandgap just below the emission lines. This static system has the potential to have efficiencies normally limited to dynamic conversion systems, on the order of 30-50%.

The breakthrough operating principle behind the system is that a working fluid composed of simple molecules thermally emits photons strongly at specific photon energies (spectral lines). The spectral efficiency of a photovoltaic cell is maximum (approaching 100% in the limit of zero cell temperature) at its semiconductor band gap energy. With appropriate choice of emitter and photovoltaic cell, energy conversion efficiency can exceed the Shockley-Queisser limit of around 40%. Figure 54 shows the principle.

Figure 54. Operating Principle of Radiative Conversion

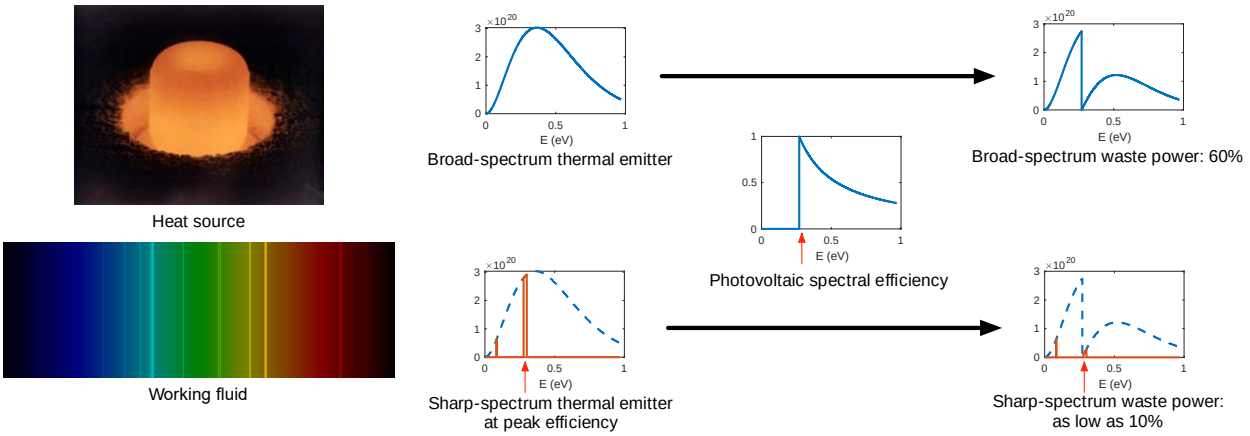

If the photovoltaic is cold, the conversion efficiency can in principle exceed 90%. Preliminary analysis suggests that, at a practical radiator-limited temperature and including conductive heat loss to the window, a likely efficiency is 25 - 50%.

This photovoltaic direct conversion system that we are developing is a novel form of thermophotovoltaic (TPV) [41], a technology which has historical interest from NASA for high-efficiency, high specific power thermal conversion [42] [43]. The operating principle of a thermophotovoltaic is as follows: a hot emitter is heated to a temperature at which it emits significant power via thermal radiation, after which a photovoltaic of low band gap (typical 0.5 eV) converts the thermally emitted spectrum into DC electrical power. TPV may use an emitter which emits in the blackbody spectrum, or may use solid selective emitters [44] [45] or spectral filters [43] [41] to engineer the incident spectrum into a favorable shape for efficiency of the photovoltaic panel. The TPV concept has approached the point of utility before, with one system sized for an RTG for use in space achieving 19% efficiency. [43]

The system we describe here is a TPV which uses a simple molecular gas working fluid as the selective emitter and spectral filter. Simple molecules such as CO_2, H_20, Ammonia, etc. have thermal emission spectra composed as sharp, isolated peaks in which 90% of the thermally radiated power may be emitted in the energy proximity of the semiconductor band gap. [46] [47] This is generally better performance than solid-state selective emitters [44] [45], and has the added benefit of being a compressible working fluid which may couple to a dynamic heat engine such as a Brayton cycle.

In this proposed system, the heat source (in our case, fusion) heats a working fluid whose thermal emission spectrum is composed of isolated peaks rather than broad-spectrum blackbody-like emissions. This working fluid is then piped to a photovoltaic panel made of a semiconductor whose band gap is marginally less energy than the energy of a strong emission peak of the working fluid. A large portion of the power lost from the working fluid is lost as radiation at that photon energy, being efficiently converted to DC power via the photovoltaic cell. A window of an IR-transmissive material separates the working fluid from the photovoltaic cell. An example

of such a paired working fluid, semiconductor, and window is Carbon Dioxide, Lead Selenide, and sapphire. Figure 55 shows a schematic.

Figure 55. Schematic of a Radiative Conversion System

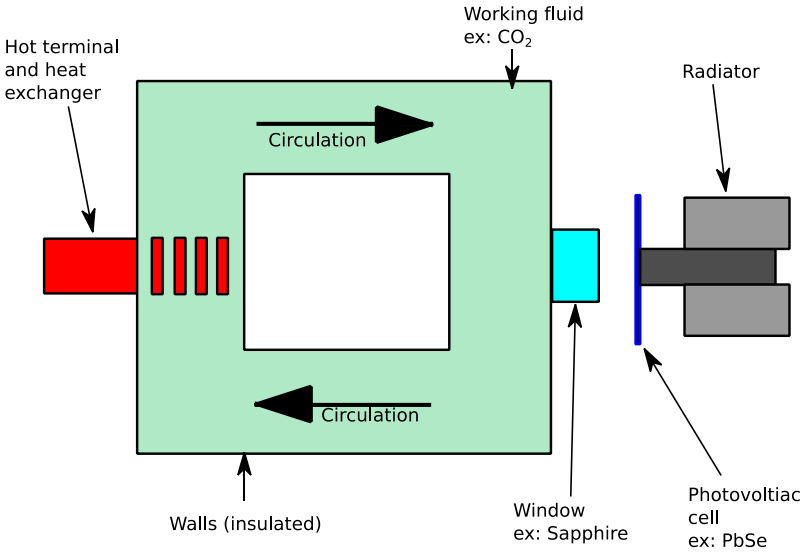

Under this NIAC Phase II, we have performed numerical modelling in MATLAB of a TPV receiving an incident thermal emission spectrum from a molecular working fluid under typical conditions.

To model the thermal emission of the gas, we have used the HITRAN molecular line database. [46] [47] A HITRAN output file may contain tens of thousands of spectral line intensities, so we have implemented functionality to determine whether a given temperature, pressure, and path length of gas is optically thick within a photon wavelength regime. This allows us to predict the thermal emission spectra of a variety of gases at a variety of conditions and geometries. We have tested many gases for applicability in this system, including H_2O, CO_2, NO, NO_2, C_2H_2, CO, CS, HF, HCN.

To model the behavior of the photovoltaic panel, we have implemented the idealized model of Shockley and Queisser [48] [49], which includes the effect of radiative recombination. This model allows us to determine the efficiency, power density, and operating voltage/current for a semiconductor of a definite band gap, at a definite temperature, receiving a definite incident radiation spectrum. For comparison, silicon and gallium arsenide photovoltaic panels achieve more than 80% of this idealized efficiency under realistic conditions [48].

Coupling the HITRAN emission model to the Shockley Queisser photovoltaic model, we have determined a candidate semiconductor/gas combination which may be suitable: PbSe and CO_2, with band gap at 0.27 eV. At 2000 K gas temperature, 1 atm gas pressure, and a gas layer of 1 cm thick:

- At a photovoltaic cell temperature of 0 K (idealized), predicted efficiency is 90%
- At 300 K cell temperature, predicted efficiency is 43%
- At 400 K cell temperature, predicted efficiency is 30%
- At 500 K cell temperature, predicted efficiency is 18%.

For IR windows, to separate the gas from the panel, sapphire and CaF are both suitable materials. They combine transmissivity in the wavelength range of interest with a low emissivity at longer wavelengths. [50] [51]

3.6.7 Other Direct Conversion Options

Other direct conversion options are possible, such as electrostatic and MHD. Neither is a good fit for the PFRC.

The SOL plasma is expected to be 10^{12} /cc, $T_e \sim 30$ eV. The Debye length, or the depth that electric fields penetrate into the plasma, is on the order of 10^{-3} cm [52]. For this reason, for the DEC method of separation to be feasible, we would have to make our plasma far more tenuous via expansion, as described by Post. [53] However, in order for the Debye length to be 10 cm, the plasma would have to be expanded to 100 times the cross sectional area.

The same argument need not apply to MHD direct conversion, in which plasma following curved field lines generates a voltage in the RxB direction. We have not studied this method in detail, as much research is required in order to evaluate MHD direct conversion's applicability to fully-ionized, magnetized plasma. Regardless of whether this method is applicable, it is expected to require heavy refractory-metal electrodes and superconducting bending magnets. It will also require a significant volume.

3.7 Updated DFD and Mission Design

From the Phase II Proposal:

> As with our Phase I, once the previous tasks are nearly complete, we will be able to update our engine and system design models. Our nominal mission architecture remains the Pluto orbiter and lander, requiring two approximately 1 MW engines, but we may consider additional interplanetary missions requiring larger engines. The objective for our design tools is to size an engine anywhere between 1 and 10 MW and to then size a spacecraft appropriately based on the needed fuel, propellant, and payload masses for a given mission.

We will present first some additional mission studies using DFD to travel from Mercury to near interstellar space. Then we will present updated point reactor designs at the 1 MW and 10 MW levels. Our specific power estimates remain in the range of 0.75 to 1.25 kW/kg.

3.7.1 Mission Analysis

DFD, with a specific impulse in the range of 10,000 to 20,000 seconds and a specific power about 1 kW/kg, is suitable for almost any interplanetary mission. When NASA recently released a solicitation for rapid, deep space propulsion, four candidate missions were identified: Mars, Jupiter, Pluto, and 125 AU for an interstellar precursor mission. We have sized a DFD engine for each candidate mission. Table 19 shows the propulsion parameters used for DFD based on the UEDGE model developed during our Phase I.

Table 19. DFD Preliminary Propulsion Parameters, UEDGE Model

Fusion Power	**1 MW**	**10 MW**
Jet Power	0.46 MW	5.6 MW
Thrust Range	4-5 N	35-55 N
I_{sp} Range	8000-8500 s	9,900-12,000 s
Jet Efficiency	0.35-0.37	0.47-0.56
Fusion Efficiency	0.17-0.18	0.27-0.31
Specific Power	0.75 kW/kg	1.25 kW/kg
Structural Fraction	0.04	0.04

These parameters are placed in the context of other advanced propulsion technologies in Figure 56. DFD generally has a power range from about 1 MW to 100 MW, where 100 MW is achieved with multiple engines, as shown by the shaded area in the plot. The feasible exhaust velocity is shown with a circle. Within that circle, the Mars, Jupiter, Pluto and 125 AU missions are shown.

Figure 56. Performance Envelope of DFD

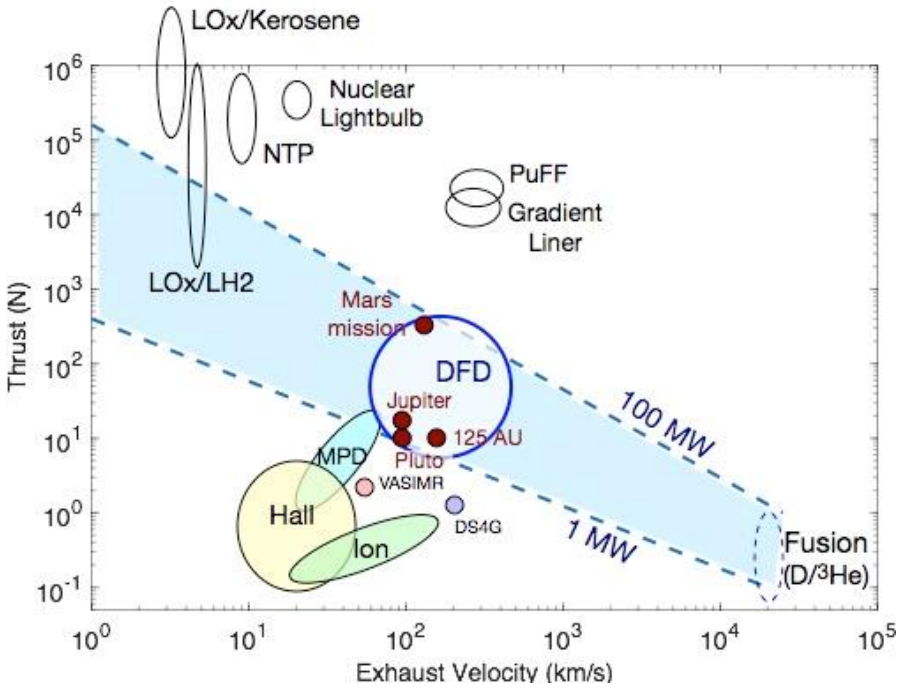

Table 20 gives specific parameters for the four candidate missions. The Mars mission has a large payload; DFD cannot accomplish this mission with our nominal specific power range, although it is possible with a longer duration: 110 days as opposed to 45 days. For comparison, the parameters that would be necessary to make the 45-day target are also shown. We would need a higher specific power, for instance by eliminating shielding, higher efficiency, and if we allow for aerobraking on arrival, then the 45-day mission would be feasible. The 125-AU mission requires a modestly higher exhaust velocity to reach the destination in 10 years versus 12. These results assume continuous, constant-thrust trajectories.

Table 20. Example DFD-Propelled Missions

Target	Payload (Mg)	Power (MW)	u_E (km/s)	σ (kW/kg)	η	Trip Time	Delta-V (km/s)	IMLEO (kg)	^{3}He (kg)
Mars	40	60	110	1.25	0.3	110 days	29.4	112000	0.98
Mars*	40	270	110	4	0.6	45 days	69.6	192000	1.5
Jupiter	1	1	80	0.75	0.2	1.2 years	55	4950	0.05
Pluto	1	0.6	80	0.75	0.2	5 years	159.67	10048	0.16
125 AU	1	0.8	200	1.0	0.4	10 years	244.3	6770	0.43

* Assumes 5 km/s aerobraking

We have also newly analyzed a trip to Mercury. A planar trajectory is shown in Figure 57. The transfer takes less than 140 days using a single 0.9 MW DFD. Given the transfer time of the recently launched BepiColumbo mission is about 7 years, this is a very dramatic improvement.

Figure 57. Four-month transfer from Earth to Mercury using 21 km/s delta-V and 0.9 MW

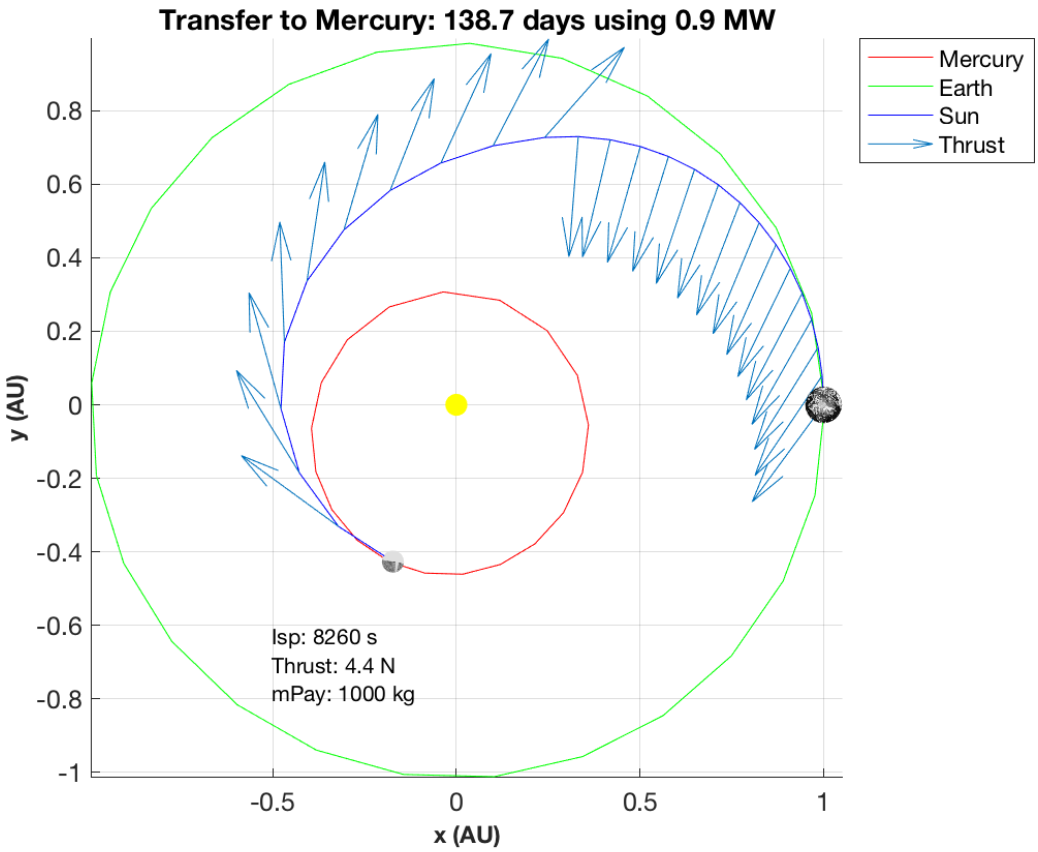

3.7.2 DFD Reference Design

The DFD reactor reference design includes the following components:

- Superconducting magnets, axial and nozzle
  - Windings mass
  - Structural mass
  - Cryocooler mass
- X-ray absorbing layers (Bremsstrahlung)
- Microwave reflecting layers (Synchrotron)
- Shielding
- RF heating subsystem
- Electricity conversion subsystem
- Radiators

In order to estimate sizes for these components, it computes the following:

- Fusion power given fuel ratio, ion and electron temperatures and densities
- Power lost to ionizing the SOL plasma (“gas box”)

- Neutron power loss
- Radiation power loss
    - Power converted to electricity
    - Power radiated as heat

A variety of assumptions and parameters are required to fully specify a model, including:

- RMF heating power as a fraction of total fusion power
- RF drive efficiency
- Electricity conversion efficiency
- Amount of tritium and deuterium side reactions
- Synchrotron wall reflection
- Shielding attenuation factor
- Radiator areal mass, emissivity, and temperature
- Scrape-off-layer thickness

Table 21 shows the nominal engine design parameters that are common to all point designs presented in this report. The plasma beta, which is the ratio of the plasma pressure to the magnetic pressure, is estimated based on the distance between the flux conserving magnet surface and the edge of the plasma. The electron temperature of 55 keV is based on the latest synchrotron models with high wall reflection (Section 3.3.3). We assume that all of the tritium reactions are suppressed by rapid ejection of the tritium ash via the scrape-off-layer (f-T of 0), while allowing all of the D-D side reactions (f-D of 1). The RF and gas box power fractions are estimates. There is a mass margin of 10% for additional structure and components such as cabling.

Table 21. Nominal engine parameters

Parameter	Value
Beta	0.88
Scrape off layer thickness	0.05 m
Plasma radius	0.25-0.3 m
Helium3 - Deuterium ratio	2.5:1
Electron density	4.6e20 m^{-3}
Deuterium temperature	120 keV
Helium-3 temperature	80 keV
Electron temperature	55 keV
f-T, factor for Tritium side reactions	0
f-D, factor for Deuterium side reactions	1
RF power fraction	0.11
Gas Box power fraction	0.2
Structural mass fraction	0.1
Synchrotron wall reflection	95%
Conversion efficiency	0.6

Radiator cold/hot temperatures	[300 453]
Radiator areal mass	4.2 kg/m^2

There are many tradeoffs that can be made in terms of the plasma densities, ion temperatures, and reactor size when computing a specific point design. It is most conservative to assume a single ion temperature for both ion species, but if the helium-3 can be heated differentially from the deuterium, and up to 140 keV, the specific power is higher. If we increase the assumed plasma density, the magnet field will be higher requiring larger magnets, but the length needed to produce a given power will be less. For these point designs we used a plasma density to give a central field of about 5 T, given beta.

The magnetic field is computed from the assumed beta and the plasma parameters. The magnets are sized assuming HTS at 20 K for the axial magnets and 10 K for the nozzle. The RF and power generation subsystems are estimated using simple scale factors. The shielding is scaled so that for neutron wall loading of about 1.5 kW/m^2, 10 cm of shielding is used. The shielding is modeled as a cylinder the length of the fusing plasma.

Table 22 shows the final point design for a 1 MW reactor. The plasma length is adjusted until the desired output fusion power is reached, given the plasma temperatures and densities. This reactor has a length to radius ratio (kappa) of 1.8. Table 23 gives the mass breakdown by subsystem. Table 24 gives the power breakdown. Table 25 shows the heat budget with 40% sent to the radiators.

Table 22. 1 MW Reactor Point Design

Parameter	Value
Plasma radius	0.25 m
Plasma length	0.9 m
Deuterium number density	7.7e+19 /m^3
Helium-3 number density (2.5:1)	1.9e+20 /m^3
Magnetic field	5.0 T
Shielding	10 cm LiH
Total Mass	1345 kg
Fusion Specific Power	0.75 kW/kg

Table 23. 1 MW Reactor Subsystem Masses

System	Mass (kg)	Percentage
Shielding	160	11.9%
Magnets	285	21.2%
Cryocoolers	147	10.9%
RMF system	118	8.8%
Thermal Conversion	207	15.4%
Radiators	305	22.7%

Structure & Margin	122	9.1%

Table 24. 1 MW DFD Power Budget

Power Component	Value	Percentage
Gas box power	0.14 MW	13%
Neutron power	2.57 kW	<0.25%
Bremsstrahlung power	0.22 MW	20.5%
Synchrotron power	0.15 MW	14.2%
Thrust power	0.56 MW	52%
Total Power	**1 MW**	

Table 25 1 MW DFD Heat Power Budget

Heat Engine	Value	Percentage
Bus power	0.19 MW	38%
Radiated power	0.21 MW	40%
RF power	0.12 MW	22%
Total Heat Power	**0.52 MW**	

Table 26 shows the final point design for a 10 MW reactor. The plasma length is adjusted until the desired output fusion power is reached, given the plasma temperatures and densities. This reactor has a length to radius ratio (kappa) of 7.6. The power fractions are the same as the 1 MW model so they are not repeated, but Table 27 gives the subsystem masses and Table 28 the heat budget, just to show the amount of electrical power available.

Table 26. 10 MW Reactor Point Design

Input Parameter	Value
Plasma radius	0.3 m
Plasma length	5.0 m
Deuterium number density	8.2+19 /m^3
Helium-3 number density (2.5:1)	2.0e+20 /m^3
Magnetic field	5.2 T
Shielding	14.3 cm LiH
Total Mass	9400 kg
Fusion Specific Power	1.07 kW/kg

Table 27. 10 MW Reactor Subsystem Masses

System	Mass (kg)	Percentage
Shielding	1545	16.4%
Magnets	825	8.8%

Cryocoolers	290	3.1%
RMF system	1110	11.8%
Thermal Conversion	1930	20.5%
Radiators	2845	30.3%
Structure & Margin	855	9.1%

Table 28. 10 MW Reactor Heat Budget

Heat Engine	**Value**	**Percentage**
Bus power	1.79 MW	38%
Radiated power	1.93 MW	40%
RF power	1.10 MW	22%
Total Heat Power	**4.82 MW**	

3.8 Conclusions

We have published results from the NIAC study and received follow-on contracts to continue our work. These will be listed in the following sections. We also present nominal roadmaps for bringing DFD to flight. We are pleased to have received follow-on funding from both NASA and the DOE and we will continue to work to advance this technology.

We would like to thank the NIAC program for their support!

3.8.1 Publications, Intellectual Property, and Follow-On Work

During the course of our NIAC Phase II, we published several conference papers.

1. *Modeling the Thrust of the Direct Fusion Drive*, Stephanie J. Thomas, Michael A. Paluszek, Samuel A. Cohen, and Alexander Glasser, AIAA 2018 Joint Propulsion Conference, July, 2018, AIAA 2018-4769, https://doi.org/10.2514/6.2018-4769
2. *Space Nuclear Power Systems – Direct Fusion Drive*, Stephanie J. Thomas, Michael A. Paluszek, Samuel A. Cohen, et al, AIAA 2018 Joint Propulsion Conference, July, 2018, AIAA 2018-4974, https://doi.org/10.2514/6.2018-4974
3. *Fusion-Enabled Pluto Orbiter and Lander,* Michael Paluszek, Stephanie J. Thomas, Samuel Cohen, Nick McGreivy, and Eugene Evans. AIAA SPACE and Astronautics Forum and Exposition, AIAA SPACE Forum, (AIAA 2017-5276) *https://doi.org/10.2514/6.2017-5276*
4. *Direct Fusion Drive for Interstellar Exploration,* S. Cohen, C. Swanson, G. Pajer, S. Thomas, M. Paluszek, et al, Foundations of Interstellar Studies Workshop, CityTech, NY, June, 2017, just published in JBIS [54]

In addition to the above papers, we will also present two papers on DFD at the upcoming International Astronautical Conference in Washington, DC, October: “Direct Thermal Energy Conversion via Tuned Thermal Emitter and Photovoltaic Band Gap” and “Fusion Propulsion for Extrasolar Exploration”.

During the course of our Phase II, we won two FY 2017 STTR contracts in partnership with Princeton Plasma Physics Lab, listed below. This was possible due to our NIAC support. The superconducting magnet STTR was awarded a Phase II which is ongoing.

1. T2.01-9966 High Efficiency RF Heating for Small Nuclear Fusion Rocket Engines
2. T2.01-9960 Superconducting Coils for Small Nuclear Fusion Rocket Engines

We have also been awarded a new grant under ARPA-E’s OPEN 2018 solicitation. This solicitation is for all types of energy research, which support ARPA-E’s mission areas. Fusion was explicitly included in the solicitation for the first time. Our award of $1.25M is intended to support electron and ion heating to 1 keV temperatures. While the PFRC-2 was designed with this objective in mind, the budget was never sufficient to complete the engineering challenges of upgrading both the magnet the RF systems to the necessary power levels. ARPA-E awarded two other fusion programs under OPEN as well, leaving us very optimistic that DOE is likely to continue funding alternate fusion concepts. (The other two awardees are CT Fusion, a spheromak, and Zap, a z-pinch, previously funded under DOE’s ALPHA program). If we meet our milestones under this grant, we will be very competitive for future RFPs.

We have additional SBIR proposals underway and are also submitting a Phase III proposal to the NIAC program. For our Phase III, we have decided to focus on the thermal conversion subsystem coupled with the RF heating subsystem. These are critical components of DFD that can be advanced independently from the fusion physics.

We have also disclosed two inventions and submitted provisional patents:

1. Magnetic Dipole Cancellation
2. Direct Conversion of Thermal Energy to DC Power

3.8.2 Roadmaps

The final portion of our report is an examination of roadmaps and paths to flight. There are a number of critical subsystems of DFD, of which the fusion core is only one:

1. PFRC, fusion core
2. Superconducting magnets – axial (5-7 T)
3. Superconducting magnets – nozzle (20-30T)
4. Magnet cryogenics
5. RF subsystem
6. Fueling system – small (1 kW) neutral beams
7. Plume steering

8. In-space startup system/APU
9. Thermal Conversion
    a. >100 kW Brayton engine
    b. Radiative conversion
10. Low mass radiators (likely carbon-carbon)
11. Propellant management and cryogenic storage
12. Shielding/neutronics

Currently, these subsystems are mostly at TRL 2, although we estimated that the magnet cryogenics, fueling system, and radiators are at TRL 3, and propellant management is TRL 4. Plume steering with additional magnets is purely conceptual at this point and therefore TRL 1.

Figure 58 shows a roadmap developed as part of our team proposal to NASA's Deep Space Rapid Transit Institute. We planned in that Institute, which was not selected for award, to build a new PFRC testbed specifically for propulsion studies, the "PFRC-P". This testbed would have utilized 0.5 T superconducting magnets along its axis. Due to the needs for the Institute to involve multiple universities, the budget for the testbed itself was less than $2M. The Institute research objectives are shown in Figure 59 and included a variety of important modeling activities, materials activities, and physics experiments. The roadmap continues on the PFRC-P with a full fusion demo expected to be completed by 2030, which could be followed by a flight prototype and then a first flight system about 2035 to 2040. Simply put, we envision three machine generations before the first flight system.

Figure 58. Roadmap developed as part of Propulsion Institute proposal

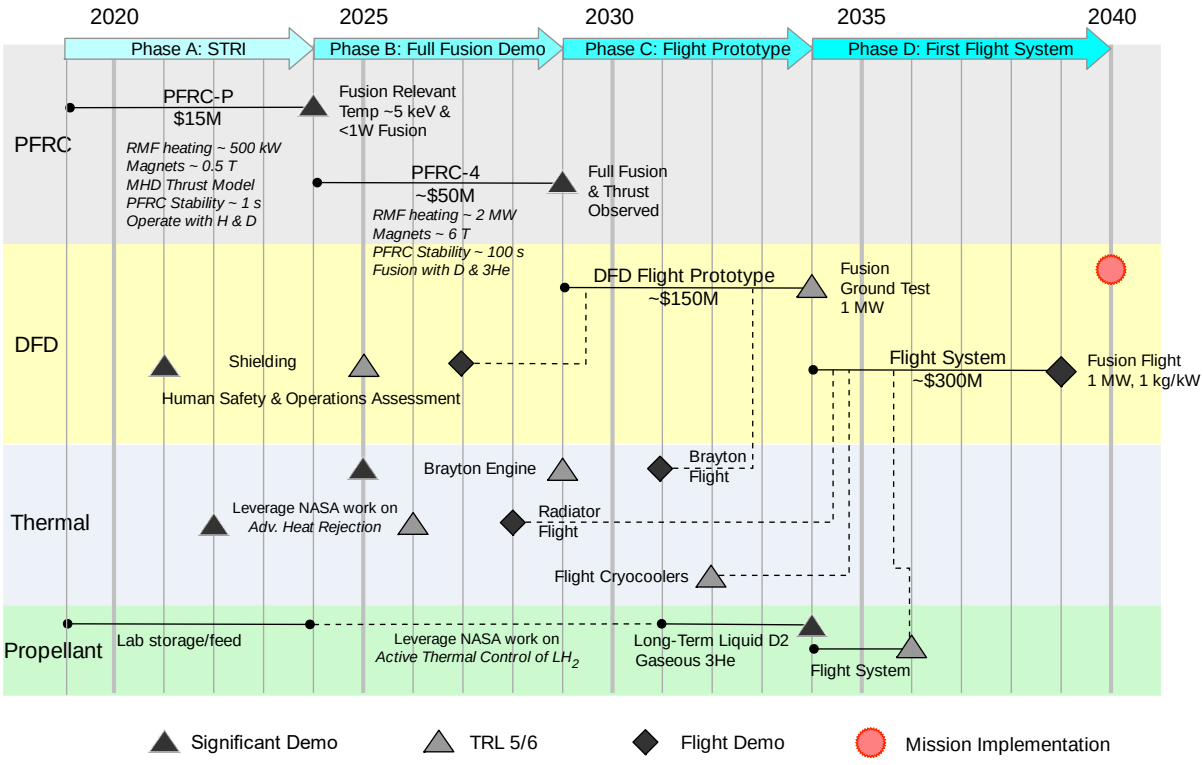

This roadmap shows that the thermal and propellant subsystems are expected to leverage ongoing NASA work on advanced heat rejection and active thermal control of LH2. These subsystems are needed for other technologies. The roadmap is not specific about the thermal conversion subsystem. There is certainly sufficient time in this roadmap to develop space-qualified Brayton engines, although our new radiative conversion system may prove preferable. We are addressing this gap with our NIAC Phase III proposal.

Figure 59. Proposed Propulsion Institute Milestones

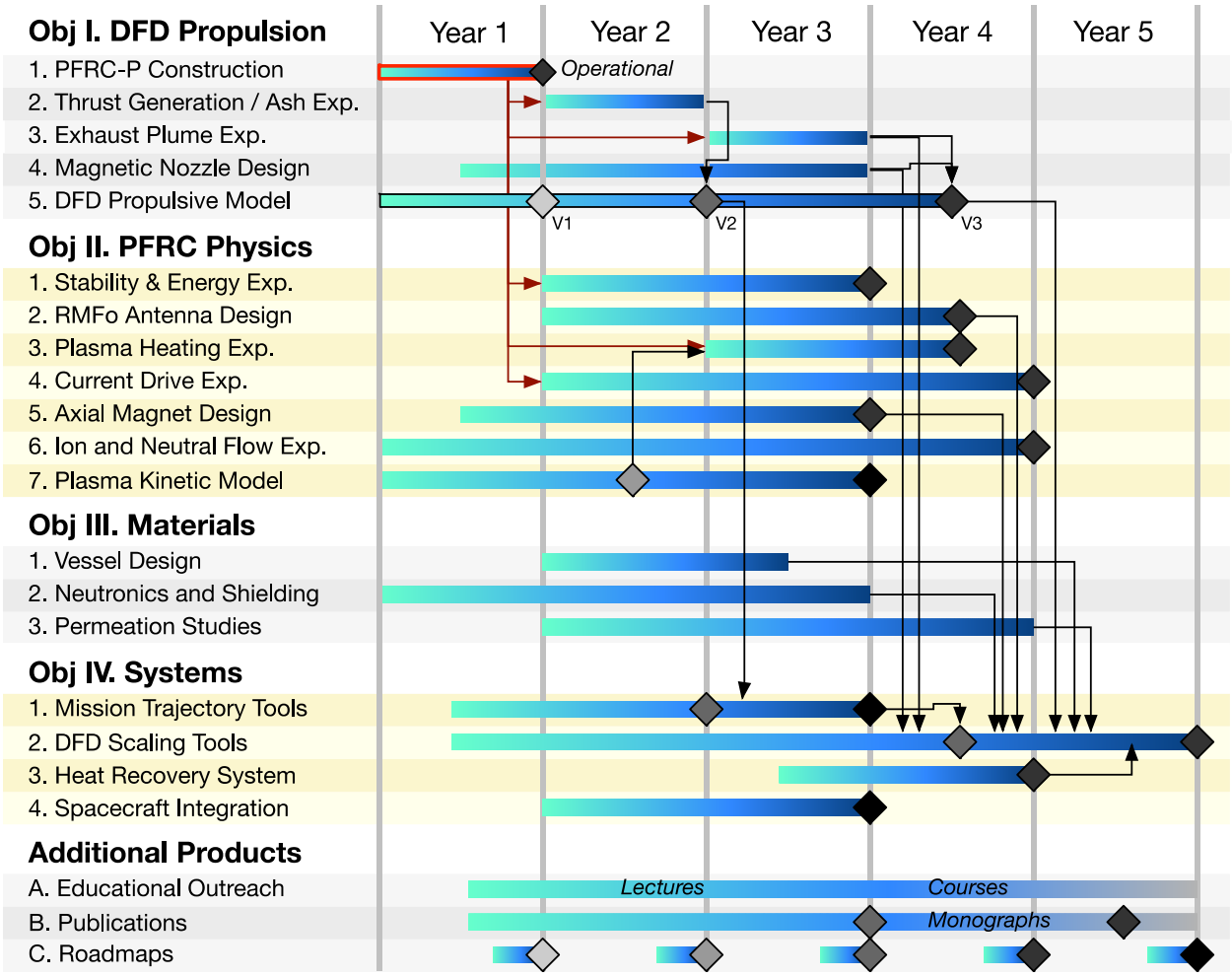

4 Bibliography

[1] G. P. M. B. E. H. J. M. M. P. A. H. G. a. S. A. C. Yosef S Razin, "A direct fusion drive for rocket propulsion," *Acta Astronautica,* no. 1, p. 145–155, December 2014.

[2] G. P. Y. R. J. S. S. C. R. F. K. G. a. M. W. M. Paluszek, "Direct Fusion Drive for a Human Mars Orbital Mission," *International Astronautical Congress,* October 2014.

[3] Y. R. S. C. A. G. J. Mueller, "Direct Fusion Drive Rocket for Asteroid Deflection," *33rd International Electric Propulsion Conference,* October 2013.

[4] L. S. Mason, "Power Conversion Concept for the Jupiter Icy Moons Orbiter," NASA Glenn Research Center, 2003.

[5] J. F. Santarius, "Generic Magnetic Fusion Rocket," University of Wisconsin, 1998.

[6] Y. Z. A. R. K. D. A. a. P. B. A. Sundaram, "2G HTS wires made on 30 um thick hastelloy substrate," *Superconductor Science and Technology,* vol. 29, no. 10, 2016.

[7] C. B. M. B. M. K. a. G. M. Carmine Senatore, "Field and temper- ature scaling of the critical current density in commercial REBCO coated conductors," *Superconductor Science and Technology,* vol. 29, no. 1, 2016.

[8] G. D. M. A. D. Z. a. A. d. C. L. Muzzi, "Cable-in-conduit conductors: lessons from the recent past for future developments with low and high temperature superconductors," *Superconductor Science and Technology,* vol. 28, no. 5, 2015.

[9] R. P. a. D. X. F. a. H. W. W. a. M. Eisterer, "Suitability of coated conductors for fusion magnets in view of their radiation response," *Superconductor Science and Technology,* vol. 28, no. 1, 2014.

[10] D. X. Fischer, "The effect of fast neutron irradiation on the superconducting properties of REBCO coated conductors with and without artificial pinning centers," *Superconductor Science and Technology,* vol. 31, 2018.

[11] Y. Z. A. R. K. D. A. A Sundaram, "2G HTS wires made on 30μm thick Hastelloy substrate," *Superconductor Science and Technology,* vol. 29, 2016.

[12] D. R. Ladner, "Performance and Mass vs. Operating Temperature for Pulse Tube and Stirling Cryocoolers," in *International Cryocoooler Conference (16th),* Atlanta, GA, 2008.

[13] G. W. H.J.M. ter Brake, "Low-power cryocooler survey," *Cryogenics,* vol. 42, no. 11, pp. 705-718, 2002.

[14] P. Kittel, "Cryocooler Performance Estimator," in *International Cryocooler Conference,* 2007.

[15] J. R. a. E. Tward, "Small Space Cryocoolers," in *49th AIAA Aerospace Sciences Meeting,* Orlando, FL, 2011.

[16] M. C.-C. R. F. K. G. M. K. J. K. E. M. S. N. M. P. T. R. S. T. a. M. W. S.A. Cohen, "Reducing Neutron Emission from Small Fusion Engines," *66th International*

Astronautical Congress, pp. IAC-15,C4,7-C3.5,9,x28852, October 2015.

[17] S. Tamor, "Synchrotron Radiation Loss from Hot Plasma," *Nuclear Instruments and Methods in Physics Research Section A: Accelerators, Spectrometers, Detectors and Associated Equipment,* vol. 271, no. 1, p. 37–40, 1988.

[18] E. A. P. V. V. ,. a. B. G. M. Serov, "Reflectivity of Metals in the Millimeter Wavelength Range at Cryogenic Temperatures," *IEEE Transactions on Microwave Theory and Techniques,* vol. 64, no. 11, p. 3828–3838, November 2016.

[19] K. K. Sessou, "Design of a class-F power amplifier with reconfigurable output harmonic termination in 0.13 Âμm CMOS," Iowa State University, 2014.

[20] Y. Kim, "High Efficiency Frequency Tunable Inverse Class-E Amplifier in VHF Band," *International Journal of Engineering and Industries (IJEI),* vol. 2, no. 3, Sept 2011.

[21] B. A. M. R. Brench, "The Finite-Difference Time-Domain Method," in *EMI/EMC Computational Modeling Handbook,* Boston, MA, Springer Science, 1998, pp. 35-67.

[22] A. I. N. M. E. a. S. A. A. Livshits, "Physico-chemical origin of superpermeability Large-scale effects of surface chemistry on hot hydrogen permeation and absorption in metals," *Journal of Nuclear Materials,* vol. 170, p. 79–94, 1990.

[23] A. I. N. M. E. S. A. A. B. A. O. D. A. Y. a. P. V. I. Livshits, "Su- perpermeability to fast and thermal hydrogen particles: applications to the pumping and recycling of hydrogen isotopes," *Journal of Nuclear Materials,* p. 159–163, 1992.

[24] Y. O. N. S. H. N. Y. L. A. N. M. A. V. a. B. A. Nakamura, "Development of divertor pumping system with superpermeable membrane," *Fusion Engineering and Design,* Vols. 49-50, p. 899–904, Nov. 2000.

[25] B. J. H. S. a. D. C. Peters, "Metal Foil Pump performance aspects in view of the implementation of Direct Internal Recycling for future fusion fuel cycles," *Fusion Engineering and Design,* vol. 136, p. 1467–1471, Nov. 2018.

[26] R. T. T. I. N. M. K. K. T. a. T. H. Ito, "Data on the backscattering coefficients of light ions from solids, A Revision," Nagoya University's Institute of Plasma Physics, 1985.

[27] S. I. A. S. K. a. A. A. P. Krasheninnikov, "Physics of Plasmas," *Divertor Plasma Detachment,* vol. 23, no. 5, May 2016.

[28] P. C. Stangeby, "Can Detached Divertor Plasmas Be Explained as Self-Sustained Gas Targets?," *Nuclear Fusion,* vol. 33, no. 11, p. 1695–1705, November 1993.

[29] P. C. Stangeby, The Plasma Boundary of Magnetic Fusion Devices, Taylor & Francis, 2000.

[30] M. A. D. J. C. H. C. L. O. N. S. R. D. a. W. J. C. Mahdavi, "Particle Exhaust from Plasma Discharges with an Expanded-Boundary Divertor," *Physical Review Letters,* vol. 47, no. 22, p. 1602–1605, Nov. 1981.

[31] K. C. R. K. M. N. J. R. K. G. a. S. W. Lackner, "Control of particle and energy transport across the boundary of a Tokamak plasma," *Plasma Physics and Controlled Fusion,* vol. 26, no. 1A, p. 105–115, Jan. 1984.

[32] S. I. K. A. S. a. P. A. A. Krasheninnikov, "Divertor plasma detachment," *Physics of Plasmas,* vol. 23, no. 5, May 2016.

[33] S. W. M. B. M. D. R. M. H. W. a. S. A. Potzel, "Characterization of the fluctuating detachment state in ASDEX Upgrade," *Journal of Nuclear Materials,* vol. 438, p. S285– S290, July 2013.

[34] J. N. Brooks, "Modeling and Analysis of Erosion and Redeposition For Limiter and Divertor Impurity Control Systems," *Nuclear Technology - Fusion,* vol. 4, no. 1, p. 33–45, July 1983.

[35] J. N. Brooks, "Modeling of sputtering erosion/redeposition status and implications for fusion design," *Fusion Engineering and Design,* vol. 60, no. 4, p. 515–526, July 2002.

[36] E. Hotston, "Threshold energies for sputtering," *Nuclear Fusion,* vol. 15, no. 3, p. 544, 1975.

[37] N. Y. Y. I. Y. I. N. K. Y. M. S. M. K. S. R. a. T. H. Matsunami, "Energy Dependence of the Yields of Ion-Induced Sputtering of Monatomic Solids," Nagoya University Institute of Plasma Physics, Nagoya, Japan, 1983.

[38] G. S. C. H. B. J. N. C. J. P. G. C. H. A. A. H. A. P. V. P. C. S. R. J. W. W. R. a. W. D. G. Federici, "Plasma-material interactions in current tokamaks and their implications for next step fusion reactors," vol. 41, no. 12, p. 1967–2137, Dec. 2001.

[39] I. H. Hutchinson, Principles of Plasma Diagnostics, Cambridge,MA: Cambridge University Press, 2002.

[40] K. F. K. B. L. J. M. N. R. S. J. F. D. R. E. W. F. J. C. a. T. A. U. Asmussen, "Spectroscopic investigations of tungsten in the EUV region and the determination of its concentration in tokamaks," *Nuclear Fusion,* vol. 38, no. 7, p. 967–986, July 1998.

[41] M. A. H. G. S. J. F. a. J. L. Zenker, "Efficiency and Power Density Potential of Combustion-Driven Thermophotovoltaic Systems Using GaSb Photovoltaic Cells," *IEEE Transactions on Electron Devices,* vol. 48, no. 2, February 2001.

[42] D. J. Anderson, "NASA Radioisotope Power Conversion Technology NRA Overview," *AIP Conference Proceedings,* vol. 746, no. 1, 2005.

[43] D. D. C. D. W. P. M. a. C. C. Wilt, "Thermophotovoltaics for Space Power Applications," *AIP Conference Proceedings,* p. 335–345, February 2007.

[44] D. L. Chubb, "Reappraisal of Solid Selective Emitters," *IEEE Conference on Photovoltaic Specialists,* vol. 2, p. 1326–1333, 1990.

[45] S. Y. J. M. a. J. G. F. Lin, "Three-Dimensional Photonic-Crystal Emitter for Thermal Photovoltaic Power Generation," *Applied Physics Letters,* vol. 83, no. 2, p. 380–382, 8 July 2003.

[46] L. S. C. P. R. A. G. S. T. M. D. P. E. J.-M. F. A. P. e. a. Rothman, "The HITRAN Molecular Spectroscopic Database and HAWKS (HITRAN Atmospheric Workstation): 1996 Edition," *Journal of Quantitative Spectroscopy and Radiative Transfer,* vol. 60, no. 5, p. 665–710, November 1998.

[47] L. S. D. J. A. B. D. C. B. M. B. L. R. B. M. R. C. e. a. Rothman, "The HITRAN 2004 Molecular Spectroscopic Database," *Journal of Quantitative Spectroscopy and Radiative Transfer,* vol. 96, no. 2, p. 139–204, 1 December 2005.

[48] S. Rühle, "Tabulated Values of the Shockley–Queisser Limit for Single Junction Solar Cells," *Solar Energy*, p. 139–147, 1 June 2016.

[49] W. a. H. J. Q. Shockley, "Detailed Balance Limit of Efficiency of P-n Junction Solar Cells," *Journal of Applied Physics*, vol. 32, no. 2, p. 510–519, 1 March 1961.

[50] R. M. M. J. L. M. E. T. a. F. F. M. Sova, "High-Temperature Infrared Properties of Sapphire, AlON, Fused Silica, Yttria, and Spinel," *Infrared Physics & Technology*, vol. 39, no. 4, p. 251–261, 1 June 1998.

[51] K. Y. O. a. O. M. Hisano, "Spectral Emissivity of Calcium Fluoride," *Journal of the Physical Society of Japan*, vol. 23, no. 3, p. 651–651, 15 September 1967.

[52] Naval Research Laboratory, "NRL Plasma Formulary," 2011.

[53] R. F. Post, "Mirror Systems: Fuel Cycles, Loss Reduction and Energy Recovery," in *British Nuclear Energy Society, Nuclear Fusion Reactor Conference at Culham Laboratory*, 1969.

[54] S. Cohen, "Direct Fusion Drive for Interstellar Exploration," *JBIS*, vol. 72, pp. 37-50, 2019.

[55] A. H. M. a. L. C. S. Ishida, "Variational Formulation for a Multifluid Flowing Plasma with Application to the Internal Tilt Mode of a Field-reversed Configuration," *The Physics of Fluids*, vol. 31, no. 10, p. 3024–34, October 1988.

[56] A. W. Carlson, "A Search for Lower-hybrid-drift Fluctuations in a Field-reversed Configuration Using CO2 Heterodyne Scattering," *Physics of Fluids*, vol. 30, no. 5, p. 1497–1509, May 1987.

[57] H. Y. A. L. H. R. D. M. L. C. S. R. D. B. C. L. D. J. A. G. P. M. K. E. M. a. G. C. V. Guo, "Improved Confinement and Current Drive of High Temperature Field Reversed Configurations in the New Translation, Confinement, and Sustainment Upgrade Device," *Physics of Plasmas*, vol. 15, no. 5, February 2008.

[58] R. M. A. N. R. C. S. K. S. N. T. R. M. C. T. M. W. B. a. T. T. Magee, "Direct Observation of Ion Acceleration from a Beam-Driven Wave in a Magnetic Fusion Experiment," *Nature Physics*, vol. 15, no. 3, MArch 2019.

[59] M. R. a. G. R. S. T.D. Rognlien, "Users' Manual for the UEDGE Edge-Plasma Transport code," LLNL, N/A, 2000.

[60] S. Bingren, "Core Plasma Characteristics of a Spherical Torus Fusion Reactor," *Plasma Science & Technology*, vol. 7, p. 00, April 2005.

[61] B. T. P. C. a. J. R. R.W. Hyers, "Lightweight, High-Temperature Radiator for Space Propulsion," U. Mass Amherst, Amherst, 2012.

[62] M. C.-C. R. F. K. G. M. K. J. K. E. M. S. N. M. P. T. R. S. T. a. M. W. S. A. Cohen, "Reducing Neutron Emission from Small Fusion Rocket Engines," in *66th International Astronautical Congress*, Jerusalem, 2015.

[63] R. Lewis, "Space shielding materials for Prometheus application," Knolls Atomic Power Laboratory, 2006.

[64] D. M. C. T. S. E. e. a. A. Bushman, "The martian surface reactor: An advanced nuclear power station for manned extraterrestrial exploration.," Nuclear Space Application Program , 2004.

[65] L. Hively, "A Simple Computational Form for Maxwellian Reactivities," Plasma Engineering, 1982.

[66] M. C. H. W. W. M. Eisterer, "Neutron irradiation of coated conductors," *Superconductor Science and Technology,* August 2009.

[67] A. H. G. a. S. A. Cohen, "Ion and electron acceleration in the field-reversed configuration with an odd-parity rotating magnetic field," *Physics of Plasmas,* vol. 9, no. 5, pp. 2093-2102, May 2002.

[68] L. Mason, "A comparison of brayton and stirling space nuclear power systems for power levels from 1 kilowatt to 10 megawatts," NASA Glenn Research Center , 2002.

[69] M. Tuszewski, "Observations of Tilt Instabilities in Field-Reversed Configurations of a Confined Plasma," *Physical Review Letters,* vol. 66, no. 6, p. 711–14, 1991.

5 Acronyms

APU – Auxiliary Power Unit
CAD – Computer-Aided Design
CC – Center Cell, of the PFRC-2
DFD – Direct Fusion Drive
DOE - Department of Energy
EM - Electromagnetic
FB - Fast Baratron
FEC - Far End Cell, of the PFRC-2
FRC – Field-Reversed Configuration
HTS – High-Temperature Superconductors
ITER - International Thermonuclear Experimental Reactor
LSP – Large Scale Plasma
LTS – Low-Temperature Superconductor
MNX – Magnetic Nozzle Experiment
NRL – Naval Research Lab
PFRC - Princeton Field-Reversed Configuration
PPPL – Princeton Plasma Physics Lab
PSS – Princeton Satellite Systems
RMF – Rotating Magnetic Field
RF – Radio frequency
SEC – Source End Cell, of the PFRC-2
SOL – Scrape-off-layer
TPV - Thermophotovoltaic

Appendix A. PFRC Technical Description

This section provides a description of the PFRC that is intended for a general technical audience, without requiring plasma physics expertise. The interested reader is referred to our many physics publications for further details.

A.1 PFRC Overview

The Princeton Field Reversed Configuration (PFRC) nuclear fusion reactor is a revolutionary approach to fusion power generation. The reactor would be small and clean, producing very few damaging neutrons and enabling rapid development at relatively low cost. The 1-10 MW reactors are suitable for diverse applications, from submarines to urban environments to space propulsion.

There are two plasmas in the PFRC: a hot, fusing core plasma, and a cool, energy-extracting Scrape-Off Layer (SOL) plasma. The core plasma is shaped into a closed magnetic field region by a rotating magnetic field (RMF), driven by antennae outside the plasma. This closed magnetic field region is confined by a linear electromagnetic coil. The RMF also heats the plasma to a temperature of 100 keV (1.2 billion Kelvin, 80 times hotter than the center of the Sun), at which nuclei within the plasma fuse.

The SOL plasma is much cooler, with a temperature of 20 eV (230,000 Kelvin). No fusion occurs in the SOL, but the fast particles produced from fusion in the core deposit their energy in this plasma. The SOL is not confined; rather it flows from an upstream gas box, around the core, and into a collection chamber. If the PFRC is in the Direct Fusion Drive (DFD) configuration, the SOL flows out into space and generates thrust.

Only some of the energy leaves the core as fast particles. Sizable portions also leave as microwaves, X-rays, and neutrons. This energy is absorbed in the walls of the fusion reactor and converted into electrical power.

Figure 60. PFRC Schematic showing the magnetic field topology and locations of the coils

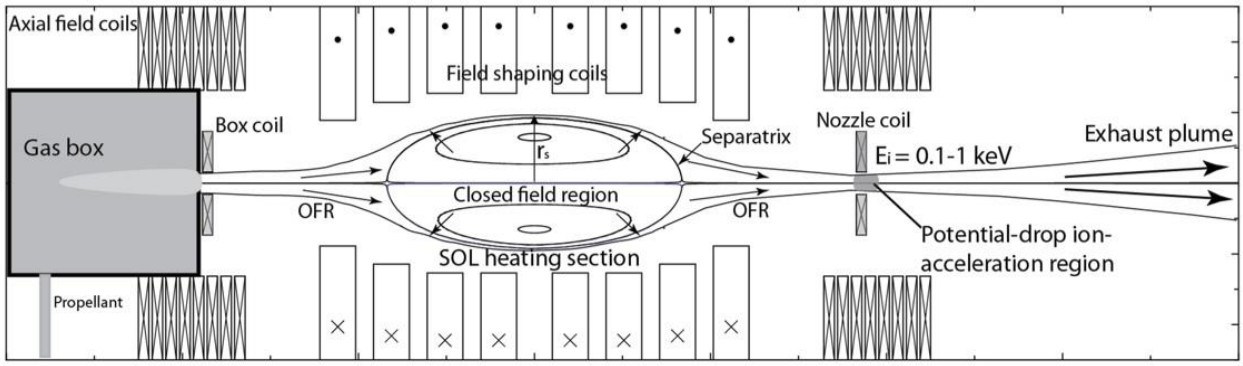

The rotating magnetic field strength is about 1% of the strength of the axial magnetic field. The antennae are figure-8 shaped, with the direction of the induced magnetic field having opposite

directions on either side of the machine midplane. This leads to the name, “odd-parity” heating, which contrasts with the traditional “even-parity” heating configuration. The odd configuration uniquely produces closed magnetic field lines of the internal torus, which would otherwise allow plasma to leak out. This method of heating was invented by PPPL scientist Dr. Sam Cohen.

Figure 61. External antennae produce rotating magnetic fields. The azimuthally rotating electric field results in a plasma current.

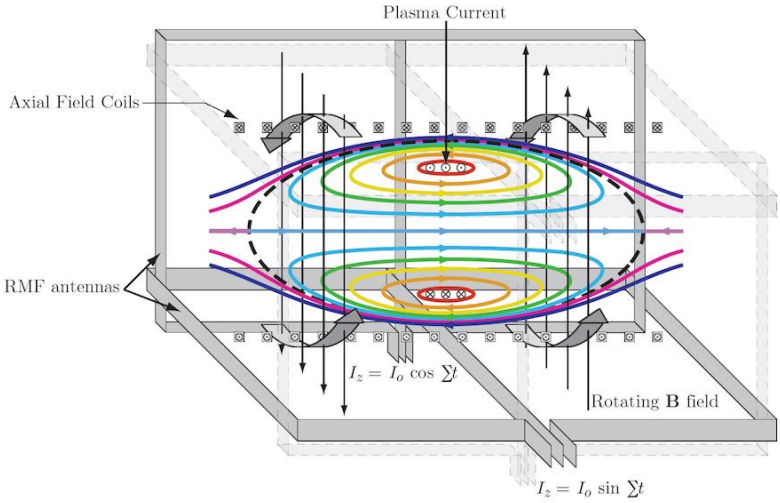

The PFRC is designed to produce exceptionally few neutrons. The primary fuels are the deuterium and helium-3, which produce only charged particles and no neutrons when they fuse. Deuterium-deuterium side reactions will produce small numbers of moderate energy neutrons and some tritium. If the tritium fuses with deuterium, high energy neutrons are produced which are very damaging. The small size of the machine allows tritium particles produced to be exhausted in the SOL before fusing, thus mitigating these harmful deuterium-tritium side reactions. The production of neutrons is reduced further by altering the fuel ratio to have three times the helium-3 as deuterium, i.e. a ratio of 3:1, favoring the helium-3 reactions.

Competing fusion concepts such as tokamaks that burn deuterium-tritium fuel suffer from high production of very damaging neutrons. These machines require complex, expensive, and thick shielding systems. In these gigawatt scale reactors, power must be extracted using 1 m-thick possibly liquid lithium layers. The lithium itself is hazardous. Even with the lithium shielding, the irradiated reactor walls will need to be frequently replaced. The PFRC can be shielded simply with boron carbide, a chemically stable solid.

The core plasma’s closed field region is in the form of a field-reversed configuration (FRC). The field-reversed configuration results in a high beta, which is the ratio of the plasma pressure to the applied magnetic field. This allows for a high pressure to be achieved with a lower magnetic field. A standard tokamak has a maximum beta below 8% while the PFRC will have a beta approaching 1.

The simple geometry of the machine, low radiation, and moderate magnetic field strength all contribute to lowering development and maintenance costs. There are no hazardous fuels or materials required. The PFRC has been designed to be safe and affordable.

A.2 The Field-Reversed Configuration

The FRC is a closed magnetic field topology that is achieved without any central penetrations or magnets. This results in a compact toroid inside a cylindrical plasma. Plasma current flows in the toroid perpendicularly to the applied external field. The field in the center of the toroid is reversed with respect to the external field. This configuration may be achieved in a variety of ways; when formed using an inductive electric field (theta-pinch), the axial field is literally reversed around a pre-ionized gas. FRCs can also be formed, sustained, and heated by application of neutral beams. In the PFRC, the FRC is formed using rotating magnetic fields (RMF).

Figure 62. Field-Reversed Configuration.

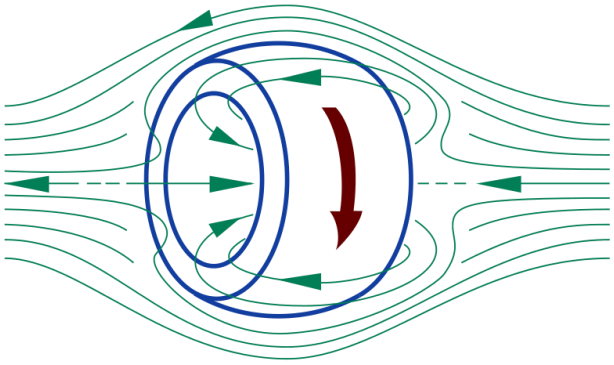

Image Source: Wikimedia Commons

Rotating magnetic field methods using external antennae are classified as even-parity or odd-parity. The rotating field is generated by external coils or antenna and the direction of this field is rotated about the machine axis. The field rotation causes the electrons in the plasma to rotate at the same average angular frequency, producing current and reversing the magnetic field.

In a plasma confinement device, a global mode or macro instability is a mode in which the entire plasma becomes unstable and falls apart. The worst global mode in an FRC is the tilt mode, in which the plasma magnetic field rotates to align itself with the external magnetic field, destroying the FRC. Experiments on the LSX experiment and analytic studies using two-fluid or finite-orbit-size MHD agree: The stability boundary for tilt mode is such that an elongated FRC at the magnetic field, size, and temperature of the PFRC is stable. [55] Experiments on the current PFRC-2 experiment have held an FRC stable for 100,000 times longer than the tilt mode would allow.

In a plasma confinement device, in the absence of macro instabilities, the transport (leakage of particles and energy) is set by micro instabilities. These are small-scale fluctuations which

transpose the locations of cold and hot packages of plasma or allow momentary pathways for hot plasma to escape. In an FRC, the dominant micro instability is the Lower Hybrid Drift Instability (LHD). LHD has been observed to saturate at very low levels, sufficient for the PFRC to achieve fusion with significant margin. [56] [57] Recent FRC experiments at Tri Alpha Energy have even measured confinement close to what would be expected from no micro instabilities whatsoever. [58]

A.3 PFRC Fusion Reactions

There are four fusion reactions of interest for a deuterium/helium-3 reactor. The first is the deuterium/helium-3 reaction itself, which produces no neutrons. There are two deuterium-deuterium side reactions, which will occur in nearly equal proportions. One of these produces a moderate energy neutron and additional helium-3 while the other produces tritium and a proton. The final reaction, deuterium-tritium, produces a dangerous high-energy neutron.

D + ^{3}He >	He (3.6 MeV)	+ p (14.7 MeV)
D + D >	T (1.01 MeV)	+ p (3.02 MeV)
D + D >	^{3}He (0.82 MeV)	+ n (2.45 MeV)
D + T >	He (3.45 MeV)	+ n (14.1 MeV)

Figure 63 shows the cross-sections of the relevant fusion reactions. The D-He3 reaction rate is considerably higher that the D-D reaction rate at the target temperature of 100 keV. Note that the D-T cross section is even higher than D-He3 at this temperature, which makes removing the tritium critical.

Figure 63 Fusion Reaction Cross Sections.

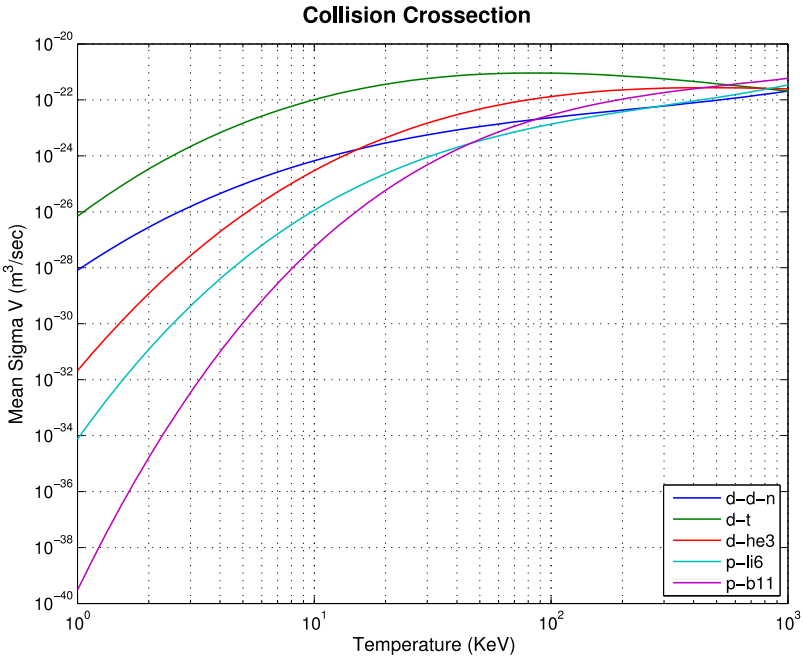

In the PFRC, about 99% of the power is projected to be in the D-^{3}He reactions, and about 0.5% in each of the deuterium-deuterium reactions. The tritium is exhausted before it can fuse, so that the power in that reaction should approach zero.

A.4 RMF Heating Method

For an FRC reactor to burn a D – ^{3}He fuel mixture, the plasma ions must be heated to over 50 keV. If energetic neutral-beam injection were used for achieving these temperatures, the plasma would have to be over 4 m in diameter in order to "stop" the injected neutral beam. Such a large reactor would produce proportionally large amounts of power, near 1 GW. In RF heating methods, on the other hand, power can be absorbed over shorter distances. Using odd-parity RMF allows the diameter of the plasma to be reduced to 0.5 m and produce a few MWs.

In odd-parity RMF heating, the maximum ion energy is proportional to the RMF frequency ω_{RMF}. Due to a constraint set by the RMF-generated current and the FRC's magnetic field strength, the RMF frequency decreases as the product of plasma density times the square of the plasma radius. Thus, too large or dense an FRC is not well heated. An optimum FRC for RMF heating of ions to 100 keV and above has a radius in the range from 20 to 30 cm.

RMF creates a time-varying azimuthal electric field near the O-point null line [Glasser, 2002]. This periodically accelerates ions into betatron orbits and then decelerates them back into cyclotron orbits. Choosing the frequency and amplitude properly allows ions to be pumped up, repeatedly, to energies near the peak of the D–^{3}He fusion cross-section and then returned to the bulk temperature.

Figure 64 Ion Trajectories showing energy pumping (RMF Software)

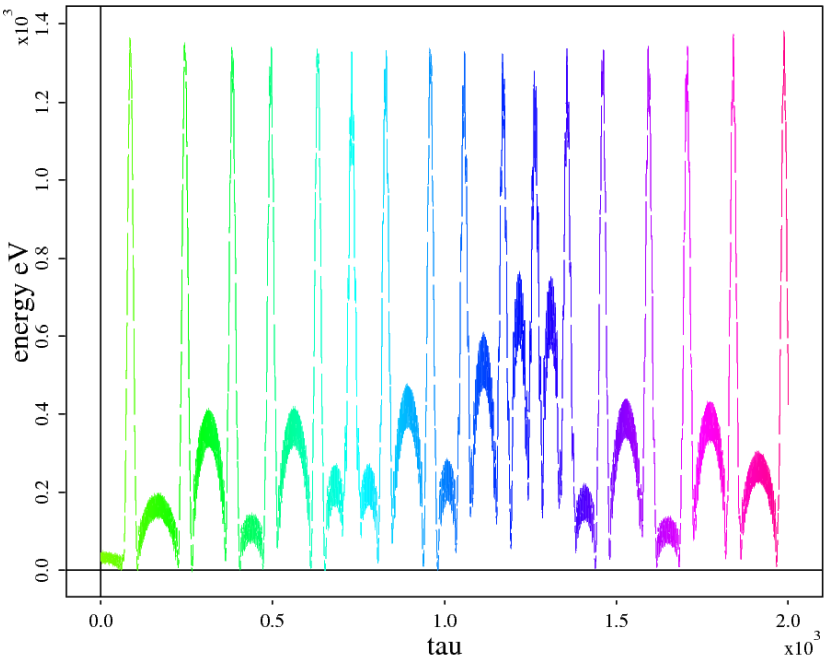

In a D–^{3}He plasma, the trajectories of the accelerated ions are predicted to form two betatron-orbit streams close to the FRC's O-point null line, a D stream and a ^{3}He stream. The deuterium stream ions have half the peak energy of the ^{3}He ions, causing non-zero relative velocity between them. The energy dependent fusion rates can be used to show the basic effect of the higher energy of the ^{3}He stream. If the bulk plasma has an average energy of 70 keV and the RMF pumps the ^{3}He up by 100 keV it will pump the deuterium up by only 50 keV. This favors the desirable D-^{3}He reactions and reduces the percentage of fusion power in deuterium-deuterium reactions, to less than 1%.

A.5 Reduction of Neutrons

Overall, the shielding requirements for this type of small, clean reactor are far less than for a larger deuterium-tritium fusion engine. The neutrons from the D-D side reactions are only 2.45 MeV, which is 1/6 of the energy of those produced by D–T. The larger surface-to-volume ratio for a small FRC, about 25 cm radius, compared to a large tokamak, about 10 m, results in a 200-fold reduction in neutron power load on the wall.

With a low *s* value of around 3, the energetic tritium products will pass across the separatrix and traverse the cold scrape-off-layer. The tritium products slow down in about 0.01 s while the characteristic burn-up time is 20 s. Their trajectories end up fully in the SOL, from where they are promptly expelled with the propellant.

A.6 Radiation Losses

There are two key mechanisms for radiation loss from the plasma: synchrotron radiation and bremsstrahlung. Synchrotron is produced due to the acceleration of relativistic charged particles through magnetic fields. Since we are confining the plasma with magnetic fields, we will always get synchrotron radiation. Bremsstrahlung or "braking radiation" is due to the deceleration of a charged particle when deflected by another charged particle, typically an electron by an atomic nucleus. Since our plasma is a mix of electrons and nuclei this will happen frequently. Both types of radiation are electromagnetic. Heat from the radiation losses is converted to electrical power using a thermal conversion system.

A.7 Thrust Augmentation

Thrust augmentation is the process by which additional ionized gas flows through the PFRC and produces thrust. The fusion products alone, if ejected directly from the engine, would have a velocity of 25,000 km/s and produce negligible thrust. In the PFRC, these products interact with cool ionized gas in a region called the scrape-off-layer (SOL). Energy is transferred from the hot products to the SOL electrons, and this energy is in turn transferred to the ions as they traverse and exit the magnetic nozzle. The result is an exhaust with a bulk exist velocity of about 100 km/s and a thrust of about 2.5 to 5 N per MW of fusion power.

The magnetic nozzle has been studied under separate DOE grants for the Magnetic Nozzle Experiment (MNX) program. The LSP particle-in-cell code has been used to study plasma detachment. Figure 65 shows an example result for ion kinetic energy at 3110 nanoseconds. Figure 66 shows the ratio of the axial velocity fraction to the axial magnetic field fraction, indicating values higher than one. These studies verify that electron energy is transferred to the ions and that detachment from the magnetic field lines occurs.

Figure 65. Ion Kinetic Energy from LSP PIC Simulation

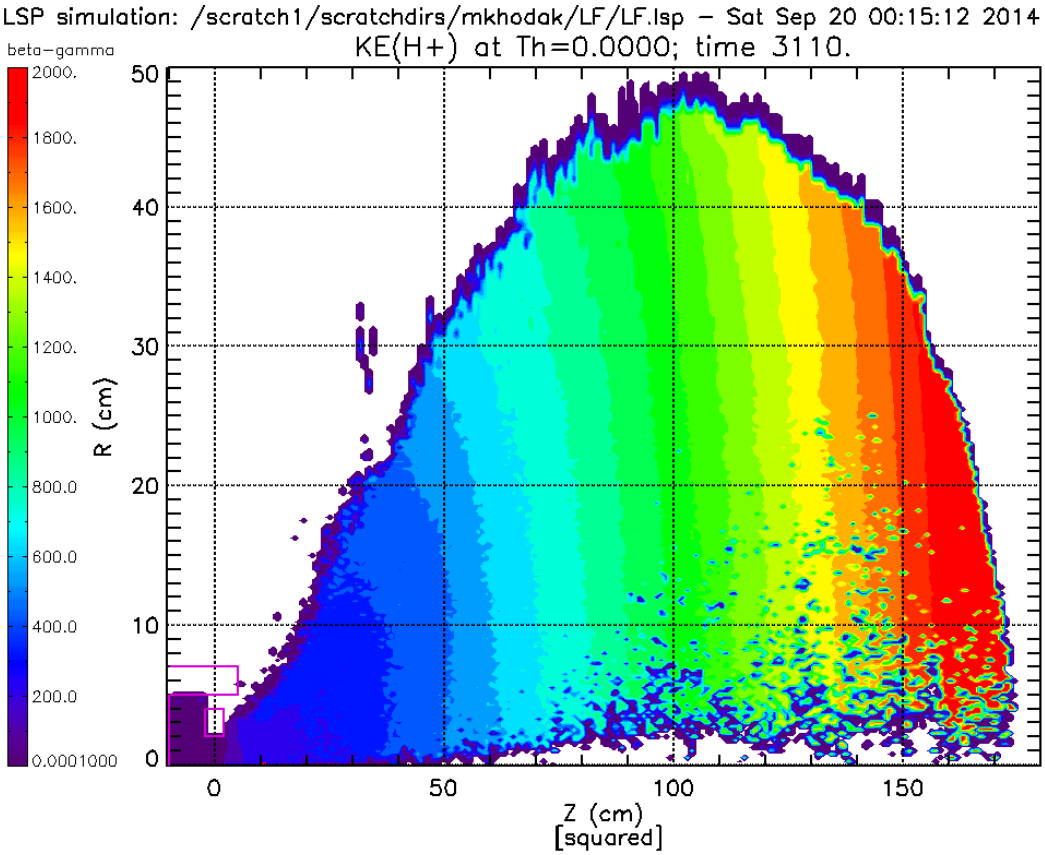

Figure 66. Ratio of Axial Velocity to Axial Field Components from LSP PIC Simulation

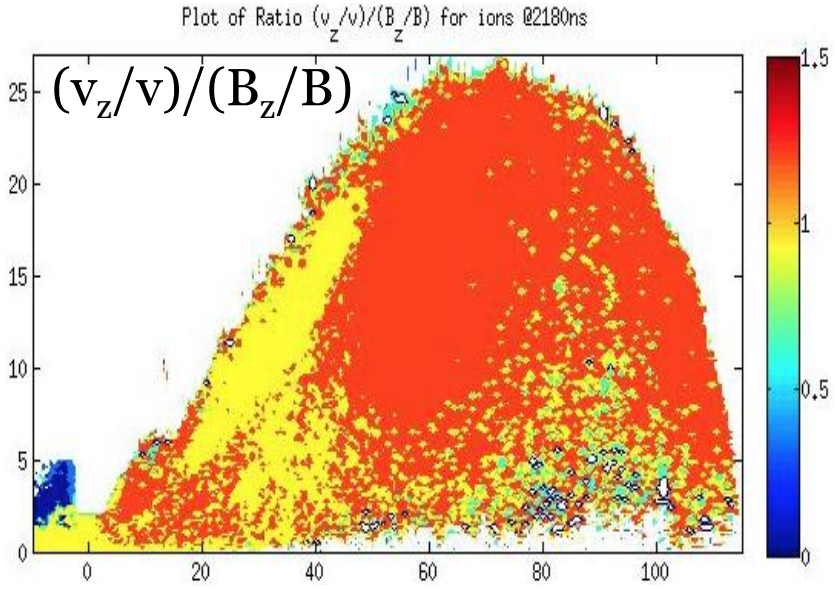

A.8 Development Plan

PPPL has been performing PFRC-2 research under a DOE grant. PFRC-2 was designed to characterize ion heating to kilovolt energies. PFRC-3 would be designed to achieve fusion-relevant temperatures of about 5 keV. The first fusion demonstration could potentially be achieved in a second phase of PFRC-3, PFRC-3b, or in a larger and stronger PFRC-4. Each stage of this phased development plan, Figure 67, is designed to reach significant scientific and technological milestones. Unanticipated physical processes may result in poorer plasma performance than predicted.

Figure 67. PFRC Development plan

Machine	PFRC-1	PFRC-2	PFRC-3A	PFRC-3B
Objectives	Electron Heating	Ion Heating	Heating above 5 keV	D-He3 Fusion
Fuel	H	H	H	D-3He
Goals/ Achievements*	3 ms pulse* 0.15 kG field* e-temp = 0.3 keV*	0.1 s pulse* 1.2 kG field i-temp = 1 keV	10 s pulse 10 kG field i-temp = 5 keV	10 s pulse 80 kG field i-temp = 50 keV
Plasma Radius	4 cm	8 cm	16 cm	16 cm
Time Frame	2008-2011	2011-2017	2018-2022	2022-2026
Cost	$2M	$4M	$25M	$25M

The next sections further describe the experimental stages. Following PFRC-3B, the next step would be a full-scale PFRC-4 reactor with a plasma radius of 25 cm.

PFRC-2: Prove ion heating method

The goal of PFRC-2 is to achieve 0.1-second-duration hydrogen plasmas with 1-keV ion and electron temperatures at a magnetic field strength of 1.2 kG. Plasmas of this temperature have never before been made in FRCs. When such temperatures were achieved in tokamak research nearly 50 years ago, international fusion research rapidly grew. The main technical achievements for the PFRC-2 have been the implementation of an array of passive high-temperature superconducting (HTS) magnets and construction of a higher power RF plasma heating system, with antennae external to the vacuum vessel. This plasma heating system would be useful for other applications, e.g., semiconductor/materials processing and spacecraft propulsion.

PFRC-3A: Achieve thermonuclear parameters

The goal is to increase the pulse length to 10 seconds, the temperature to 5 keV, and the magnetic field to 10-kG magnetic field. The plasma parameters achieved would be adequate for D-T fusion though not for *really clean* (D-^{3}He) fusion. This high power, near steady-state plasma source could be useful for many applications, including toxic waste destruction and heat flux generation for materials fabrication and testing.

- A full array of active HTS magnets would be designed, prototyped, built, and tested. These will allow sufficiently long pulses that most steady-state heat-load questions can be answered.
- Additional diagnostics and a higher power RF system would be built and installed.
- First tests of the thrust augmentation and efficient ^{3}He fueling methods would be made.
- Scenarios for stage 3B would be developed. These include studies of energy confinement and current-drive efficiency.

PFRC-3B: Demonstrate low-neutron-production fusion and ash- and energy-removal methods

The goal is to achieve 100-minute total operation of 100-second-duration D-^{3}He plasmas with fusion demonstrated at $0.1 < Q < 2$. The ion temperature would need to reach 50 keV and the magnetic field 60 kG.

- Neutron shielding would be added.
- Neutron and Q diagnostics would be added.
- This stage would use the same full HTS magnet array as 3A, except the field would be raised a factor of 6, still well below the current limit for HTS.
- Operational scenarios for efficient ^{3}He fueling, novel energy extraction methods, and fusion power control would be developed.
- Modeling of He-catalyzed D-D fusion for terrestrial power generation will be made, guided by the experimental results.

A.9 PFRC Summary

A PFRC reactor would be about 2 m in diameter, 10 m in length, and produce between 1 and 10 MW of steady-state fusion power. The novel radio-frequency plasma heating system enables the achievement of sufficiently high plasma temperatures for D-^{3}He fusion. The size of the machine and the operational fuel ratio combine to reduce the neutron wall load 1000-fold compared to traditional D-T machines, dramatically reducing safety and siting concerns, materials requirements, and maintenance issues. The machine requires no radioactive or dangerous materials and requires only modest amounts of shielding for safe operation. The low radioactivity and simple geometry reduce the development costs dramatically as compared to other fusion concepts. We estimate that PFRC-3A and PFRC-3B can be completed for about $50MM and five to ten years, depending on the funding profile.